IMPLANTATION AND ELECTRON EMISSION IN CLUSTER-SURFACE COLLISIONS

THÈSE N^{O} 2931 (2004)

PRÉSENTÉE À LA FACULTÉ SCIENCES DE BASE

Institut de physique des nanostructures

SECTION DE PHYSIQUE

ÉCOLE POLYTECHNIQUE FÉDÉRALE DE LAUSANNE

POUR L'OBTENTION DU GRADE DE DOCTEUR ÈS SCIENCES

PAR

Lucia SEMINARA

laurea in fisica, Università degli Studi di Genova, Italie
et de nationalité italienne

acceptée sur proposition du jury:

Dr W. Harbich, directeur de thèse
Prof. C. Brechignac, rapporteur
Dr P. Hoffmann, rapporteur
Prof. R. Monot, rapporteur
Prof. R. Palmer, rapporteur

Lausanne, EPFL
2004

Version abrégée

Ce travail de thèse est consacré aux processus microscopiques relatifs à la déposition contrôlée d'agrégats d'argent sélectionnés en masse, sur du graphite fortement orienté (HOPG) et du Pt (111).
L'implantation d'agrégats d'argent dans la surface du HOPG est étudiée en effectuant une étude systématique de la profondeur d'implantation d'Ag_N^+ (N = 1,3,7,9,13) en fonction de la taille des agrégats et de leur énergie d'impact. Ceci est obtenu par contrôle de l'oxydation thermique de la surface de graphite bombardée. Ce processus donne lieu à une attaque des défauts crées par les agrégats, pour former des cavités qui croissent latéralement tout en maintenant leur profondeur initiale. La morphologie de la surface est caractérisée par microscopie à effet tunnel (STM). Une relation directe est observée entre profondeur d'implantation et quantité de mouvement des agrégats, confirmant des résultats récents de la littérature. On a en particulier identifié un comportement universel lorsque la quantité de mouvement des agrégats est normalisée par leur surface projetée. Dans le cadre de ce modèle, il a ainsi été déterminé que la géométrie réelle des agrégats joue un rôle dominant. Il est également examiné si les agrégats individuels se comportent comme une somme d'atomes indépendants ou si des effets moléculaires sont présents. On montre en particulier que ces derniers existent au niveau de la "puissance de freinage" subits par les agrégats lorsqu'ils pénètrent dans le substrat.

L'émission électronique provoquée par les collisions agrégats-surface est présentée en fonction du substrat (HOPG et Pt(111)), de la taille, et de l'énergie incidente des agrégats d'Ag_N^+ (N = 1,2,3,4,5,7,8,9). Pour étudier l'origine des électrons émis, les différents processus d'émission et de transfert de charge durant les collisions sont analysés. L'émission est observée à des valeurs inférieures au seuil classique et les résultats sont interprétés à la lumière d'un modèle récent basé sur la semi-localisation des électrons de valence. Le substrat a également une importance dans les processus d'émission électronique : des taux d'émissions plus élevés sont mesurés pour les impacts d'agrégats sur Pt(111). On a également vérifié l'influence d'effets moléculaires. Pour les deux substrats, on trouve un effet sous-linéaire à faibles vitesses, et un effet sur-linéaire à hautes vitesses, un comportement similaire au cas de projectiles d'hydrogène reporté dans la littérature. On a également cherché à détecter des oscillations au niveau du taux d'émission électronique, qui permettraient de fournir des informations concernant les processus de transfert de charge durant la collision, ainsi que sur la structure électronique des agrégats et des substrats. De telles oscillations, récemment suggérées dans les travaux de Meiwes-Broer, ne sont pas clairement identifiées dans nos mesures.

Abstract

Microscopic processes induced by the controlled deposition of mass selected silver clusters on graphite (HOPG) and Pt(111) are investigated.

The *implantation* of silver clusters into the HOPG surface is analyzed. The first step consists in a systematic study of the implantation depths of Ag_N^+ (N=1,3,7,9,13) clusters into HOPG, as a function of the cluster size and of the incoming energy. This is achieved by controlling the thermal oxidation of the bombarded graphite surface. This process results in etching of the cluster-induced defects to form pits which grow laterally while maintaining the depth of the implanted cluster. The morphology of the surface is characterized by the STM method, which provides information on the microscopic structure of the examined sample.
We observe a scaling of the implantation depth with the momentum of the cluster, in agreement with recent results reported in the literature. In particular, a *universal behavior* is recognized when scaling the momentum with the cluster projected surface. Within this model, we find that the *real* geometry of the cluster plays a dominant role. It is also explored whether the single cluster behaves as a *sum* of independent atoms, or if molecular phenomena are present. In particular, we find *molecular effects* in the stopping power that the cluster experiences in penetrating the substrate.

The electron emission induced by cluster-surface collisions is presented as a function of the two different employed substrates (HOPG and Pt(111)), and of size and energy of the incoming Ag_N^+ (N=1,2,3,4,5,7,8,9) clusters.
In order to understand the origin of emitted electrons, we investigate the different electron emission and charge transfer processes during the collision. Emission is observed below the classical threshold and results are interpreted within a recent model based on the *semi-localization* of valence electrons. The substrate itself plays a role in the electron emission processes, and higher emission yields are measured for clusters impact on the Pt(111) target. *Molecular effects* are also investigated. For both substrates we find a size-dependent *sublinear* effect at low velocities and a *superlinear* effect at higher velocities, similar to the case of hydrogen projectiles reported in the literature.
We try to find oscillations in the electron emission yield, which would bear information on the charge-exchange processes during the collision as well as on the electronic structure of the cluster and the substrate. Such oscillations - recently suggested in Meiwes-Broer's work - are not clearly identified in our data.

Contents

Chapter 1

Introduction

Small groups of atoms, known as *clusters*, form the link between molecular and solid state behavior. Their physical and chemical properties depend on their size and shape, and can be very different from those of bulk matter. Increasing interest has emerged both from fundamental research and applications in understanding the properties of these small *nanostructures*. In any application which will use these *particular* properties, supported clusters will be employed. As a consequence, an interesting question is how these properties change in the transition from *isolated clusters* in the gas phase to clusters *supported* on a substrate. In order to characterize the particular cluster-surface system, precise conditions concerning the size of the clusters as well as the morphology of the substrate have to be defined. The ultimate goal is to prepare the *size-selected* clusters in ordered structures on surfaces to tailor new materials with novel properties. The controlled fabrication of ordered metal nanostructures remains a difficult challenge.

A first approach where a large number of structures can be created in parallel is *self-organized growth*. To cite one very elegant example one can obtain an highly-ordered array of adsorbed nanostructures through *nucleation* of deposited metal atoms on substrates which are patterned due to a periodic strain-relief [1].
Another approach for the synthesis of nanostructures with controlled size on surfaces is the *deposition* of *size-selected* clusters from the gas phase [2].
In these experiments clusters are formed in the gas phase, mass selected and soft-landed on the substrate. Schaub *et al.* [3] have demonstrated the feasibility of this method by depositing Ag_{19}^{+} clusters on rare gas layers, preadsorbed on a Pt(111) surface. This kind of analysis showed that rare gas atoms are not only efficient shock absorbing to allow soft-landing but also a sensitive tool for an investigation of the deposited particles structure. In these experiments a one to one correspondence between the cluster size before and after deposition could be shown.

Finally, a very precise method is *atomic manipulation* with scanning-probe methods [4], where the desired structures are assembled atom by atom with the tip of a Scanning Tunneling Microscope. However this technique produces one structure in the timescale of hours while the other methods described above produce 10^{15} structures per cm^2 in the same timescale.

In order to highlight the importance of the precise definition of the cluster size we cite as an example the *catalytic activity* of small metal clusters deposited on metal-oxide substrates.
Heiz *et al.* investigated and reported the size-dependent chemical reactivity of nickel clusters with up to 30 atoms [5]. To discover such size-dependent behavior, the preparation of monodispersed clusters supported on well characterized surfaces is required. Heiz and coworkers found that the reactivity for CO dissociation changes by varying the cluster size in an atom by atom manner. Moreover the authors discovered that the substrate plays an important role in changing the bonding properties of such small supported metal clusters. While inert as bulk material, nanoscale gold particles supported on various oxide supports exhibit a remarkable catalytic activity [6]. Partial electron transfer from the surface to the gold cluster as well as the presence of oxygen-vacancy (F-center) defects in the substrates, seem to be responsible of the activation of nanosized gold model catalysts for the combustion of CO [7]. The reactivity of small platinum clusters is also investigated, and they seem to maintain the same characteristics of the bulk, being catalytically active. The size dependent reactivity of platinum clusters is associated to a morphological transition from 2- to 3- dimensional structures and to the different electronic structure of the platinum clusters [8]. A more detailed study of the size-dependent catalytic properties of ultra-small supported particles can be found in [9]. Nanoassembled model catalysts fabricated by soft-landing Pd_n $(1 \leq n \leq 30)$ clusters on magnesium oxide thin films also show a striking size-dependent selectivity for the reaction paths toward the formation of butadiene, butene, and benzene [10]. Distinct size effects for the same system are also acknowledged in the efficiency of the CO + NO reaction [11].
The morphology and structure of metal deposits are very important, because they determine the activity and selectivity in the chemical process. Another physical factor that underlies the chemical activity of supported nanoclusters is the propensity of small clusters to transform between various structural isomers (structural *fluxionality*), thus promoting binding and activation of the reactants [12]. The size-dependent reactant activation is also found to correlate with the electronic structure of the catalyst [12].
The interaction between the metal and the oxide substrates is strongly influenced by

the presence of defects or point defects on the substrate [13].

From what is outlined above it becomes clear that the physics of mass-selected cluster deposition on surfaces is becoming increasingly important.
Let us now focus on the *size selected* deposition of clusters. A key parameter which controls the morphology and the *stability* of the cluster-surface system is the impact energy. Exploitation of the controllable kinetic energy of the ionized cluster beam permits to create well-defined vertical nanostructures via *implantation* of clusters into a substrate [14].
The graphite surface is a model in the field of cluster physics [14–31]. Due to its unique layered structure it could be easily cleaned by cleavage and it is chemically inert. In the last few years, the metal clusters-on-HOPG system has been modelled and experimentally analyzed. In particular we are interested in the Ag_N/graphite system, for which significant progress has recently been reported [14–16, 18–20, 26, 27, 32].
For *low deposition* energies (i.e. $< 1\,\mathrm{eV/atom}$), size-selected clusters can diffuse and aggregate. As a first example, we report on the study conducted by Bréchignac *et al.* [33] on neutral Sb_N clusters deposited at low kinetic energies on cleavage surfaces of graphite (HOPG). Defects created on graphite by ion irradiation act as nucleation sites for island growth by cluster aggregation. Several processes are identified, which are responsible for the non-equilibrium island shapes that are recognized on the surface. Restricting the surface of cluster diffusion reveals the transition between *compact* and *ramified* shapes.
A similar study conducted in the same group concerns neutral silver clusters *low-energy* deposition on graphite [30]. The fragmentation dynamics and the following relaxation to equilibrium shapes has been investigated and controlled by the deposition conditions. The authors found that the fragmentation instability of fractal islands is governed by the ratio of the length to the width of the fractal arms. Finally, recent results related to the deposition of $Ag_N O_x H_y$ clusters on the same substrate [31], show that cluster diffusion and agglomeration resulting in different island morphologies strongly depend on the cluster chemical composition.
Goldby *et al.* [21] studied the nucleation and growth of silver islands on graphite, as a function of incident cluster size. They stated that island formation on terraces cannot be governed by defects which act as nucleation sites, but possibly by the strain between the silver lattice and the substrate. In another paper [16], the same group showed that cluster aggregation is more limited at the steps than on the terraces. The mobility of the trapped clusters is limited to some motion along the steps, suggesting the possibility of the fabrication of structured arrays of size-selected particles.
At *intermediate deposition* energies (i.e. $\approx 1\,eV/atom - 100\,eV/atom$), above a thresh-

old which scales with cluster size, deposited Ag_N clusters (N=50-200) are pinned to their point of impact on the graphite surface [20]. Pinned clusters, bound to the surface by the displacement of one or more carbon atoms from the outermost surface layer, are stable against diffusion even at room temperatures.
Finally, for *high deposition* energies the Ag clusters implant into the graphite and rest at the bottom of a short tunnel [18].
The clusters implant via a mechanism of penetrating successive graphite planes immediately beneath the impact zone. Recently, scanning tunneling microscopy (STM) and molecular dynamics simulations have been used to investigate the implantation depths of Ag_7^- clusters in graphite for deposition energies of 2 keV and 5 keV [14]. By etching the cluster-induced defects to form etch-pits (which have the same depth as the implanted cluster), and by imaging these pits with the STM, they found the distribution of implantation depths for deposition energies of 2 keV and 5 keV. Differently to what was previously identified in the case of Ag_3^- impact on graphite [15], simulations suggests that for the case of Ag_7^- the different impact sites and orientation of the clusters have little effect on the implantation depth.
The controlled creation of these well-defined nanostructured systems requires a precise understanding of the scaling relations which define implantation. In particular, by molecular dynamics simulations the implantation of large Ag_N clusters (N=20-200) is found [18] to scale linearly as $E/N^{\frac{2}{3}}$. On the other hand, recent results on the impact of smaller Ag_7 clusters on graphite indicate an implantation depth which scales with the *momentum* of the clusters. This scaling relation applies also to Au_7 and Si_7, suggesting an universal scaling behavior of the implantation depth for small clusters.

To gain further insights on clusters-on-surface systems, together with a morphological study a series of different spectroscopic techniques has been developed.
Among the different techniques we cite the analysis by STM operating in the spectroscopic mode. This method allows to investigate the size-dependent electronic structure of individual clusters and the way it changes by the interaction with a surface. *Scanning Tunneling Spectroscopy* (STS) is a spectroscopic technique which gives direct access to unoccupied as well as occupied energy levels on a local level. Vinod *et al.* [34] carried out by STS a systematic study of the electronic structure of Pd, Ag, Cd and Au clusters deposited on HOPG and as a function of the cluster size. For the four metals they investigate the size-dependent conductance and energy gap, and found a tunneling conductance decrease and a widening gap with decreasing size. In particular, there is no gap in clusters larger than 1 nm, but, as the cluster size decreases below 1 nm, an energy gap emerges (which grows up to 70 meV for very small clusters). This result seems to

prove the existence of a metal-nonmetal transition for metal cluster decreasing size.
Bettac *et al.* [35] investigated the electronic structure of Pt clusters (containing from about 5 up to 400 atoms) deposited on crystalline graphite surfaces. Their STS study showed distinct peaks in the conductivity of the cluster-surface system at 6 K. As the peak separations are proportional to the inverse particle height, it seems to be evident that the discrete levels in the spectra are caused by quantum size effects. Other hints to the quantized electronic structure of clusters-on-surface system, come from STS data on silver [36] and gold [37] clusters on a graphite surface, at 5 K. The clusters are grown in nanopits on the surface, and a pronounced peak structure in the spectroscopic data is observed. However, the extraction of the electronic structure of the cluster-surface system is still an open question in current research.

Another method to investigate the clusters electronic structure which is important in the context of this thesis work is the study of the *electron emission* yield generated by the impact of clusters on a specified surface.
Electron emission has been extensively studied for collisions between ions and surfaces. Experiments with light energetic ions on surfaces showed an emission yield related to the kinetic energy of the incoming ions. This kinetic emission (KE) is caused by transfer of kinetic projectile energy onto the electrons of the solid, which may result in a variety of physical processes eventually leading to the ejection of electrons from the solid surface [38]. On the other hand, experiments with slow rare gas ions showed an electron emission which is almost independent of the velocity of the impinging ions but strongly related to their electronic structure and to the density of states of the surface [39].
Experiments have been performed to study the collision dynamics between two particles and between particle and surface [40]. The charge-exchange between the two "objects" depends on the electronic structures of both the projectile and the substrate. Studies conducted in the group of K.H. Meiwes-Broer on low energy collisions between different metallic clusters and an HOPG surface revealed the existence of an interplay between the emission of electrons and the neutralization dynamics during the cluster-surface collision [41, 42]. In particular, they assume a relation between the electron emission and the charge state of the cluster when it reaches the surface. This main assumption has to be verified. For high velocities of the incoming clusters, we can assume that the state of charge is constant during the cluster-surface collision. On the other hand, for low impact speeds, depending on the cluster type, the cluster size and the substrate, charged clusters can become neutralized or their charge can fluctuate during the collision (Stückelberg oscillations). Then, if their hypotheses are correct, Stückelberg

oscillations would yield oscillations in electron emission as a function of the cluster velocity.

The manuscript is organized as follows:

Chapter 2 is devoted to a description of the relevant physical processes at the basis of clusters-surface collisions. The geometrical and electronic structures of silver clusters and of the HOPG and Pt(111) targets are shown and discussed.

Chapter 3 describes the STM technique, as it is the main experimental method employed during this thesis.

The experimental setup is presented in chapter 4. A general overview on the apparatus common to both *implantation* and *electron emission* experiments is introduced. The additional tools specific of the two different arrangements are also described in details.

A systematic study of the implantation of silver clusters into graphite is presented in chapter 5, for different cluster sizes and over an extended energy range. Scaling relations of the implantation depth *vs* different impact parameters and the role of the cluster geometry in defining this depth are investigated. Molecular effects in the stopping power of the cluster projectile are also examined.

Chapter 6 is devoted to the study of the electron emission induced by silver clusters impact on surfaces. Potential and Kinetic emission processes as well as molecular effects in the emission yield are studied. The possibility of oscillations in the emission data as a function of the cluster velocity is analyzed, which would establish a link between electron emission and charge transfer processes during the collision.

Finally, chapter 7 contains the concluding remarks.

Chapter 2

Fundamental physical processes

2.1 Cluster Deposition Processes

The deposition event is composed by the *collision* itself and the subsequent *evolution* of the cluster-surface system. The time-scale of the first process is several picoseconds and gives rise to specific collision processes. The second extends from picoseconds to hours or even days and is related to the relaxation, through thermally activated processes, of the cluster and surface atoms that have been involved in the collision. We will not enter into the details of the evolution of the system after the collision, as the subject is not related to this thesis work. For a comprehensive review of cluster deposition processes, the reader is referred to Ref. [43].

The most relevant parameters that influence the outcome of a cluster-surface collision are listed below [43]:

- the cluster size N
- the cohesive energies per atom of the cluster $E_{\mathrm{coh}}^{\mathrm{cl}}$ and the surface $E_{\mathrm{coh}}^{\mathrm{s}}$. A useful ratio can be defined as:

$$R = \frac{E_{\mathrm{coh}}^{\mathrm{cl}}}{E_{\mathrm{coh}}^{\mathrm{s}}} \tag{2.1}$$

  This ratio ranges between 10^{-2} and 10^{2} and permits to describe a particular collision either as a hard cluster landing on a soft substrate or a soft cluster landing on a hard substrate.

- the impact energy E_0 per atom of the cluster (expressed as the ratio E_{kin}^{cl}/n_{cl} in Fig. 2.2)

- the impact angle ϕ_{in}
- the ratio between the masses of the cluster- and substrate-atoms
- the adsorption energy of the cluster atoms on the substrate

2.1.1 Impact processes

The tuning of all the parameters cited above defines the collision outcome, which is associated to a particular collision process. Figure 2.1 is an attempt to classify the different impact processes. The mechanism diagram (Fig. 2.2) proposed by Flynn and coworkers [44] organizes these processes as a function of the ratio between the energy per atom and the cohesive energy of the substrate (*reduced* energy), and of the parameter R defined above. It should be kept in mind that the diagram should only serve as a qualitative guideline, because important parameters such as the cluster size are not even taken into account.
In the following the main collision processes will be briefly illustrated and commented.

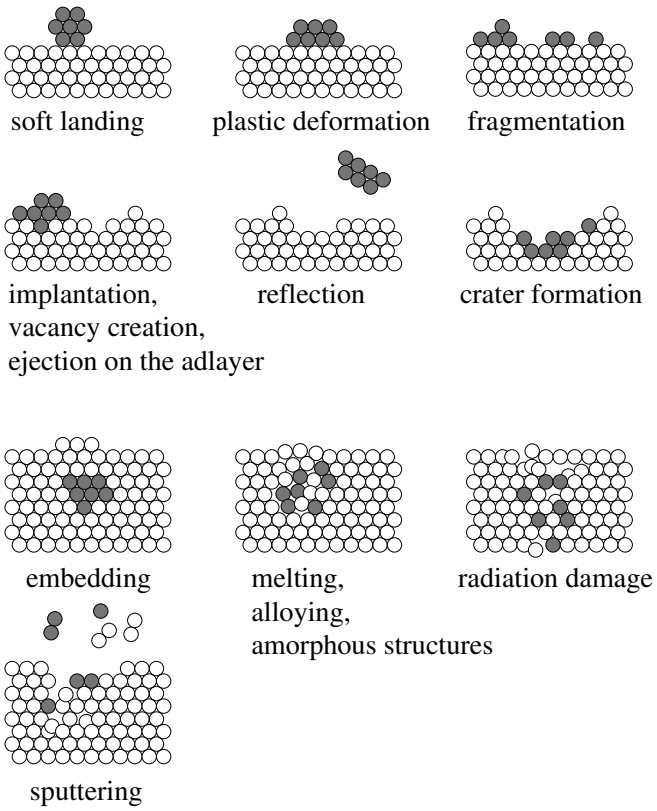

Figure 2.1: Fundamental processes in cluster-surface collisions.

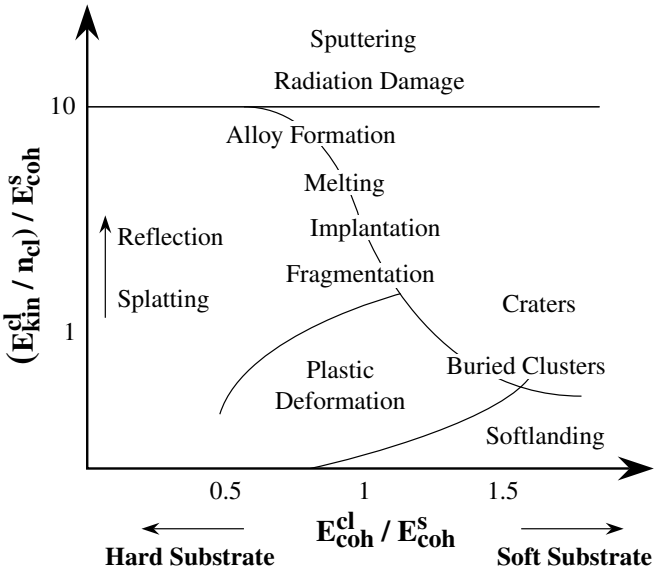

Figure 2.2: Mechanism diagram in cluster-surface collisions. The x-coordinate represents the relative binding energies of the surface and the cluster (R); the y-coordinate is the reduced energy. After [44].

Softlanding and Plastic Deformation

The ideal case of *softlanding* is depicted in the first scheme of Fig. 2.1. The cluster sits on the surface maintaining its 3-D structure, without experiencing any collision-induced deformation. In practice, even if the cluster impact energy approaches zero, the cluster-substrate interaction energy $E^{\mathrm{cl-s}}_{\mathrm{ads}}$ leads to a rearrangement of the cluster atoms. Enlarging the definition of softlanding to account for plastic deformation, an upper energy limit for these phenomena ranges about 1 eV / atom [43].
An alternative way to control softlanding conditions on hard surfaces, even at energies larger than 1 eV / atom, is to deposit clusters into a rare gas buffer layer which has been condensed on the substrate before deposition [2, 3, 45].

Fragmentation and Implantation

If the cluster kinetic energy increases, *fragmentation* and/or *implantation* of the cluster occurs.
Fragmentation is the decomposition of the cluster into two or more constituents. To fragment, a cluster has to overcome the cohesive energy of its constituents. *Implantation* occurs when the cluster penetrates partially or totally into the surface. In both cases, the ratio between the cohesive energies of the cluster and the substrate has an important role in defining the collision outcome.

A *hard substrate* shows a strong resistance to deformation and the cluster fragments upon impact [46]. At low energies small fragments can evaporate due to the rapid heating of the clusters, a few atoms might get implanted in or reflected from the surface. At higher energies shattering of the cluster takes place and backscattered fragments can be composed by small clusters.
On the contrary, a hard cluster colliding on a *soft substrate* can penetrate partially or totally into the substrate without breaking itself [14, 18, 22, 26]. It can create a crater with a rim of ejected substrate atoms. It should be mentioned here that the stability of clusters on surfaces can be strongly enhanced by *pinning* some of its atoms into the surface [20,47]. The threshold for this process depends on the cluster-target combination.

Amorphous Structures, Radiation Damage, and Sputtering

By increasing the cluster kinetic energy, local *melting* of the cluster and the substrate is observed [48,49]. This phenomenon gives rise to the formation of alloys and amorphous structures. Radiation damage is also observed, i.e. crater formation around the impact point [50], when the threshold for atomic displacement is exceeded. Atomic displacement cascades induced by the clusters lead to a high degree of disorder and to creation of vacancies down to many layers inside the bulk. The substrate atoms can even be pushed out and leave the surface (*sputtering*). Several studies show that nonlinear effects in sputtering are to be expected when clusters are used as projectiles [128].

2.1.2 Electronic processes

Electronic processes during cluster-surface collisions can provide valuable information about the dynamics of the collision [41, 42]. The impact energy and the charge state of the clusters are the fundamental parameters which characterize the electronic process. For *low impact energies* ($E < keV/atom$) the energy loss of the projectile penetrating into the target proceeds via *nuclear stopping*, while in the *high energy* regime ($E < MeV/atom$) *electronic stopping* becomes dominant.
The electronic processes induced by cluster-surface collisions can yield *photon emission*, *secondary ion emission*, and *electron emission*. Most of the literature concentrates on electron emission, which will be also the subject of Chapter 6 of this thesis work. We will not enter here into the details of the different electron emission mechanisms, which will be extensively described in Chapter 6.

2.2 Characterization of the investigated systems

In this section we describe the systems employed in the experiments performed during this thesis, namely Ag_N^+ clusters and HOPG and Pt(111) substrates. The geometric as well as the electronic structure will be characterized.

2.2.1 The Silver Clusters

Among the extensive theoretical literature on the geometrical structures of Ag_N clusters, we have chosen to refer to the work of Bonačić-Koutecký and coworkers, who in particular calculate the geometry of *positive* silver clusters up to the cluster size N=9 [51]. The geometrical structure of silver clusters will only be shown for the sizes N=3,7,9,13 (involved in implantation experiments), because it is essential for an understanding of geometrical effects in the implantation of these clusters into the HOPG substrate.
The electronic structure of small metal clusters has long been a subject of intensive theoretical and experimental studies. However, these studies concentrated on silver *neutrals* more than on positively or negatively charged clusters. The neutrals ionization potential, however, is an interesting quantity for this thesis work. It corresponds to the *neutralization* energy of the silver cluster cations, which plays an important role in electron emission processes during cluster-surface collisions (see Chapter 6).

The Ag_N^+ geometrical structures

The ground state geometries of small cationic Ag_N^+ (n=2-9) clusters have been determined in the framework of the *Hartree-Fock* procedure employing a relativistic effective core potential accounting for core-valence correlation effects [51]. Ag_2 and Ag_2^+ are the simplest and most studied silver clusters. The calculated interatomic distance of Ag_2^+ measures 2.85 Å, a larger value than that calculated for the *neutral* dimer, equal to 2.612 Å.
For the equilibrium geometry of the silver *trimer* cation, Bonačić-Koutecký *et al.* found an equilateral triangle with C_{2v} symmetry. The bond length is only slightly shorter than the nearest neighbor distance in bulk silver, i.e. 2.8 Å (first scheme in Fig. 2.3(a)).
In the case of Ag_4^+, the planar rhombus is lower in energy than the highly symmetrical tetrahedral structure. Its bond lengths are only negligibly larger than the corresponding lengths in the neutral cluster, which almost corresponds to the bulk value. This means that the removal of one electron does not increase considerably the repulsion energy, since the valence electron cloud (mainly composed of *5s* electrons) is rather diffuse.
The competition between two- and three- dimensional structures is already present for

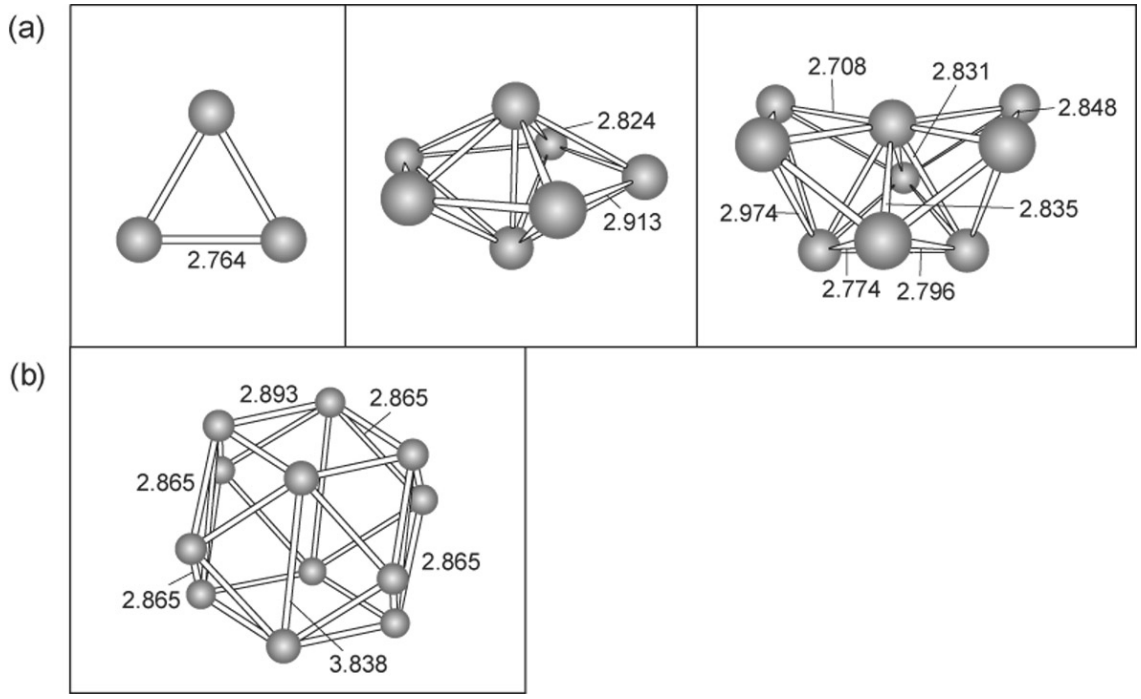

Figure 2.3: (a) The geometrical structure of Ag_3^+, Ag_7^+ and Ag_9^+. The binding lengths are also shown. After [51]. (b) The geometrical structure of the Ag_{13}^+ cluster [52].

silver pentamers. However, the cationic *pentamer* prefers a trigonal bipyramidal D_{3h} geometry. Again, the average value of the bond distances does not differ substantially from the bulk interatomic distance.

The most stable structure for the neutral and the positively charged silver *heptamer* has been calculated to be the pentagonal bipyramid. The second scheme in Figure 2.3(a) represents this configuration and indicates the bond lengths for the cluster ion. All distances are comparable to the lattice constant of the silver crystal. Due to their reduced coordination the atoms are less strongly bounded than the atoms in the bulk.

The capped pentagonal bipyramid is the best geometry for the silver *octamer* cation.

An extensive search for energetically low-lying classes of geometries was carried out for Ag_9^+ clusters. The structure with the lowest energy turned out to be the pentagonal bipyramid with two atoms capping two neighboring of the one pyramid. This geometry is sketched in the last scheme of Fig. 2.3(a).

In its ground state structure, the geometry of Ag_{13}^+ corresponds to a distorted "Jahn-Teller" cuboctahedron (Fig. 2.3(b)). This geometrical structure has been calculated with a DFT scheme by Dr. Fortunelli, CNR of Pisa, Italy [52]. The bond lengths approach even more the nearest neighbor distance in the bulk, as the cluster size N=13 starts to show "bulk-like" compact structure features.

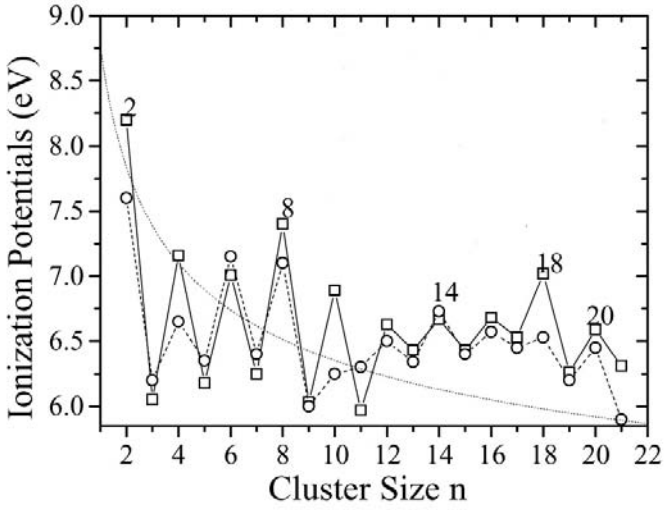

Figure 2.4: Vertical Ionization Potentials *vs* cluster size N. Circular open marks connected with dashed lines represent the measured IP values reported in [53]. These points are compared with the theoretical values from TB calculation performed by the authors of [54] (open squares connected by solid lines). Adapted from Ref. [54].

The Ag_N^+ electronic structures

As regards the electronic structure, *transition* metal clusters are more complicated than alkali metal clusters because of the presence of *d* electrons. However, a silver atom has a completely filled *4d*-shell and one 5*s* valence electron, and silver clusters are often thought to be analogous to alkali metal clusters in terms of electronic configuration. Maxima in the mass spectra of Ag (as well as of the other *coinage metals*, i.e. Cu and Au) have been repeatedly found, independently of the state of charge[1] of the cluster [55–57]. Also, as shown in Fig. 2.4, *odd-even* oscillations for (neutral) silver clusters up to the size n=20 have been found in the *Ionization Potentials* [53]. The observed anomalies in the abundance spectra as well as in the ionization potentials have been explained in terms of electronic shell-closing. Thus, silver clusters seem to behave essentially like s^1-metal clusters. However, a quantitative description of the silver cluster behavior is impossible without adequate consideration of the *d*-electrons.

We investigate the (neutral) clusters electronic properties by looking up at some examples of their electronic density of states (DOS) [54]. Fig. 2.5 represents the total *spd* electronic DOS for Ag_2, Ag_8, Ag_{13} and the bulk DOS of fcc crystal silver, evaluated from Tight Binding calculations. The total DOS contains the "compact" *d* states and the broader *sp* bands. In smaller clusters (Ag_2 in the figure) the *d* and *sp* bands are

[1]The peak structure observed in the mass spectra of neutral clusters is right-shifted of one cluster size unity when considering positive clusters.

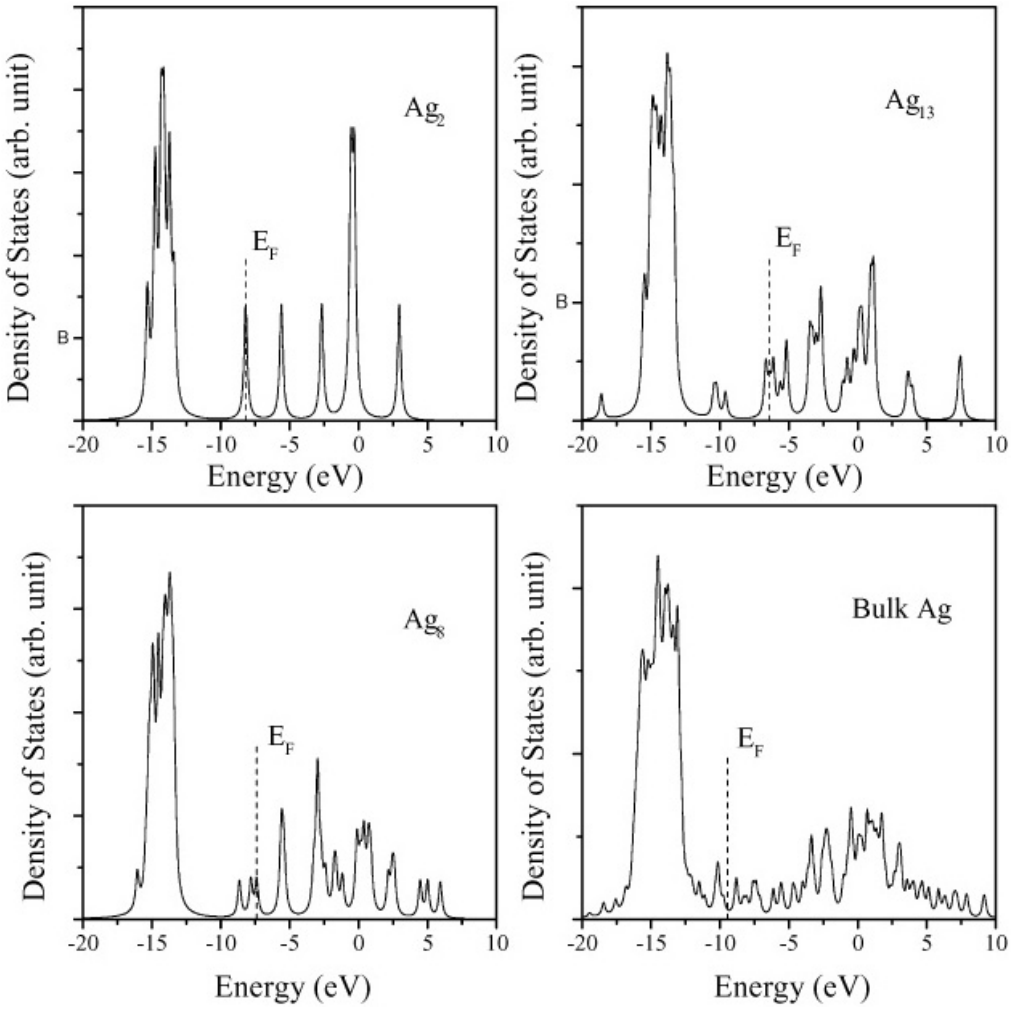

Figure 2.5: Density of states (DOS) of Ag_N (N=2,8,13) clusters *vs* energy. Bulk DOS in fcc crystalline silver is also shown for comparison. From Ref. [54].

clearly separated. The low-lying *d* band is narrow in the smallest clusters, and the broadening increases as the cluster size increases towards bulk solid. In contrast, the shell occupation of *s* electrons shows an odd-even behavior. All the peaks of the electronic structure gradually broaden, overlap, and shift with increasing cluster size, up to the reproduction of the continuous bulk electronic band. Although there are still some differences with the bulk behavior, the cluster size N=13 is considered to represent the transition between a molecular- and a bulk-like electronic structure.

2.2.2 The HOPG Structure

Graphite is a *layered semimetal* with very strong covalent carbon-carbon bonds within its *basal plane* and relatively weak *Van der Waals* interlayer forces. The planes constituted of sp^2 carbon atoms, each forming an hexagonal net, are stacked in a ABAB

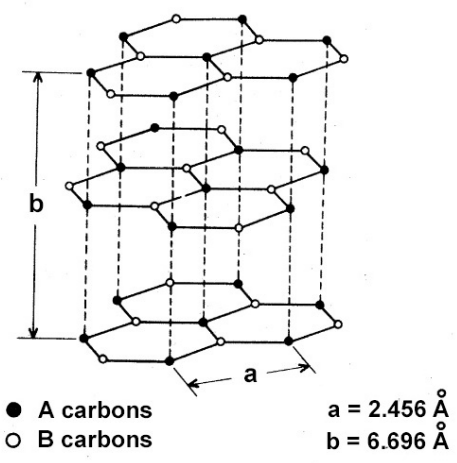

Figure 2.6: Layered structure of graphite. Adapted from Ref. [58].

sequence. It means that the A atoms are located directly above each other in adjacent planes, whereas the B atoms are located above the center (the *hollow site*) of the hexagon in the adjacent plane (Fig. 2.6). The unit cell contains 4 atoms (*three fold* symmetry), two carbons of "type A" and two of "type B" [58]. The lattice constant[2] a measures 2.456 Å and the interlayer distance corresponds to 3.348 Å.

The external surfaces of the graphite crystals are either *cleavage surfaces*, composed of atoms tightly bonded together, or *edge surfaces*, i.e. edges of layers which contain unsaturated valences. Edge surface atoms are chemically more active than cleavage surface atoms, due to their unoccupied sp^2 orbitals. These considerations will be useful to understand the process of oxidation of graphite treated in Sect. 5.2.

Besides naturally occurring single crystals, graphite is available as Highly Oriented Pyrolytic Graphite (HOPG), which is a mosaic of single crystallites, whose basal planes are oriented parallel to each other, while the in-plane lattice vectors are distributed randomly within the plane. The surface of a single crystallite is atomically flat with few defects or small steps over distances up to the micrometer.

The graphite electronic structure depicted in Fig. 2.7 has been determined within the density functional theory (DFT) [59]. The graphite electronic properties near the Fermi level are mostly determined by *delocalized* π states. The most important feature, for the aim of this work, is that HOPG is classified as a semimetal. It is characterized by a *vanishing DOS* at the Fermi level, and *non-zero* DOS values at a small distance from the Fermi Energy. Also, although it is not evident in Fig. 2.7, the $2p_z$ orbital of graphite contribute to the total DOS with a *narrow* peak located 2 eV *below* the Fermi

[2]It corresponds to the distance between two atoms of the same type or to the hexagon-center-to-center distance.

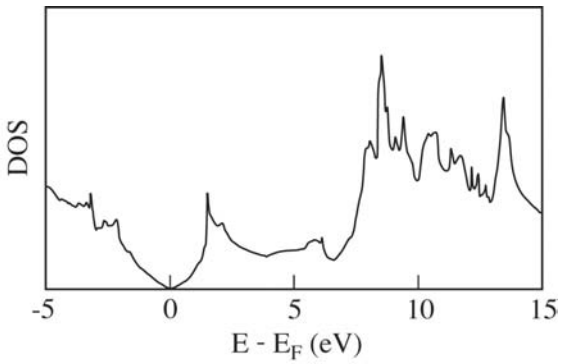

Figure 2.7: Electronic structure of graphite. Adapted from Ref. [59].

level. This information will be important for understanding *neutralization* processes in cluster-surface collisions (see Sect. 6.5.4).

2.2.3 The Pt(111) Structure

We will not enter into the details of the platinum structure, as this sample has been employed only a few times in the course of the *electron emission* measurements presented in this thesis. For better details about the (111) surface of the Pt crystal, the reader is referred to the work of the group of G. Comsa.
The equilibrium distance of the nearest neighbor atoms (denoted a in Fig. 2.8) is 2.775 Å [60]. A monoatomic step has a height of 2.26 Å [60].

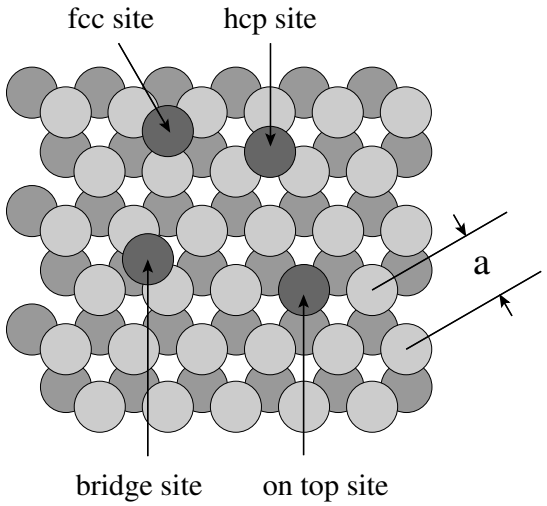

Figure 2.8: The Pt(111) surface structure. Light atoms correspond to the top layer and dark atoms to the second layer. The nearest neighbor distance is denoted as a.

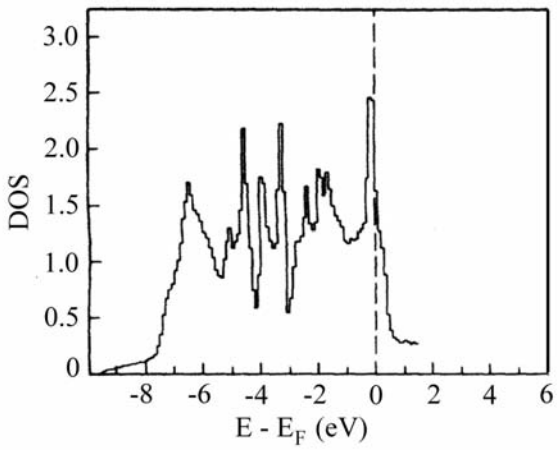

Figure 2.9: The Density of *occupied* states (electrons per atom per eV) of Pt. Adapted from Ref. [61]. The zero of energy corresponds to the Fermi level.

The Density of States (DOS) of Platinum sample is presented in Fig. 2.9. It has been calculated from *interpolated band structure* by Smith and coworkers [61]. We are not interested in understanding all the features of this *d shell* metal, but only to retain the qualitative behavior of the Pt DOS. Platinum is characterized by a *broad* density of states close to the Fermi level, and a high value of the DOS at the Fermi energy. The broad band originates from the metal *d*-electrons.

Chapter 3

Experimental Methods

3.1 Scanning Tunneling Microscopy

It has been 20 years since the Scanning Tunneling Microscope made its breakthrough by resolving the structure of Si(111)-7×7 in real space [62]. This new instrument has proved to be an extremely powerful tool. It can resolve local electronic structure at an atomic scale on almost every kind of conducting solid surface, thus also allowing the local atomic structure to be revealed. A basic reference book about the Scanning Tunneling Microscopy technique can be found in ref. [63].
In the following we will focus on the basic physical principles of the Scanning Tunneling Microscope.

3.1.1 Principles of the microscope

Fig. 3.1 illustrates the principle of operation of a Scanning Tunneling Microscope. In its basic configuration, a sharp metal tip (usually made of Tungsten or Platinum-Iridium) is attached to a piezodrive, consisting of three mutually perpendicular piezoelectric elements. Upon applying a voltage, the piezo elements expand or contract. Voltages applied on the x and y piezos allow the tip scanning on the x-y plane, voltages applied on the z piezo make the tip approaching the sample to within a few Angstroms. The electron wavefunctions of the tip overlap the electron wave functions of the surface, and a bias voltage between tip and sample causes a tunneling current to flow.
The sample energy levels will be shifted upward by $|eV|$ with respect to the tip Fermi level if a negative voltage is applied to the sample, while they will be shifted downward by the same quantity if a positive voltage is applied. Thus, the sign of V determines whether tunneling occurs from the tip occupied states to the sample empty states

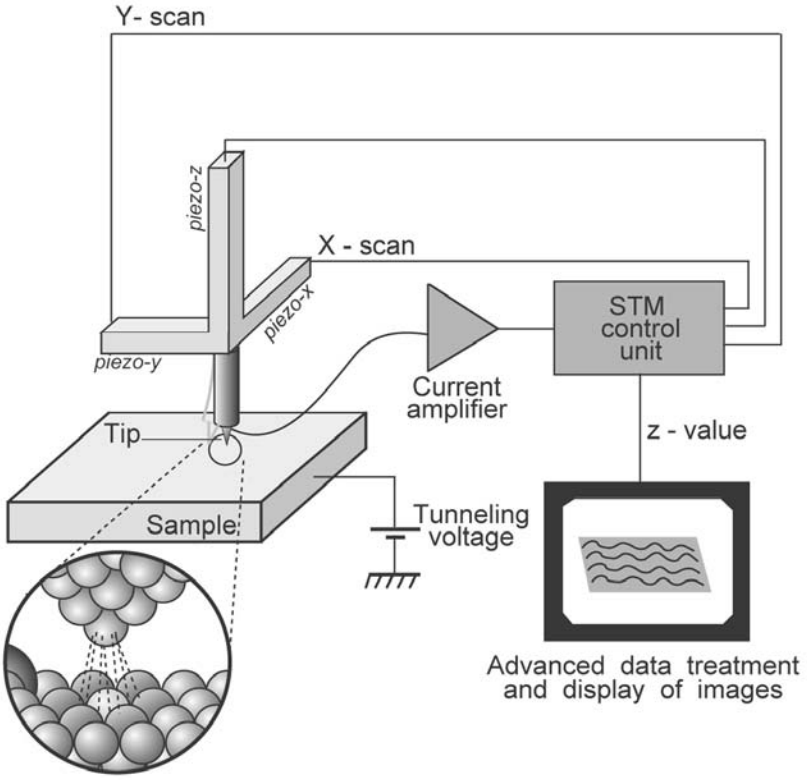

Figure 3.1: Basic principles of a Scanning Tunneling Microscope

(positive V) or viceversa (Fig. 3.2).

Starting from the basic concept of tunneling through a planar junction (consisting in planar electrodes separated by a rectangular barrier), we can explain some basic features of metal-vacuum-metal tunneling.
In the first approximation, sufficient for many applications, the tunneling probability for an electron incident on one side of the potential barrier is proportional to $e^{-2\kappa z}$, where $\kappa = \frac{\sqrt{2m\phi}}{\hbar}$ is the decay constant of the electron wave function in the barrier, and ϕ is the barrier height [63]. Strictly, this is only true for planar electrodes separated by a rectangular barrier. Neglecting effects such as the electron image potential (still a controversial issue) the height of a vacuum barrier should be approximately the work function of the electrode material. For a typical metallic work function of about 4 eV, the decay constant κ is roughly $1.0\,\text{Å}^{-1}$.
Referring to the tip-barrier-sample system (Fig. 3.2), at absolute zero the Pauli exclusion principle restricts tunneling to electrons in one side that are opposite empty states in the other, so that the tunneling current is given by [63]:

$$I_\text{t} \propto V \rho_\text{t} \rho_\text{s} e^{-2\kappa z} \tag{3.1}$$

where ρ_t and ρ_s are the local densities of electronic states in the tip and the sample. At large tip-sample distances ($\geq$20 Å) ϕ corresponds to the average work function, while at small distances it corresponds to the effective average tunnel barrier height.

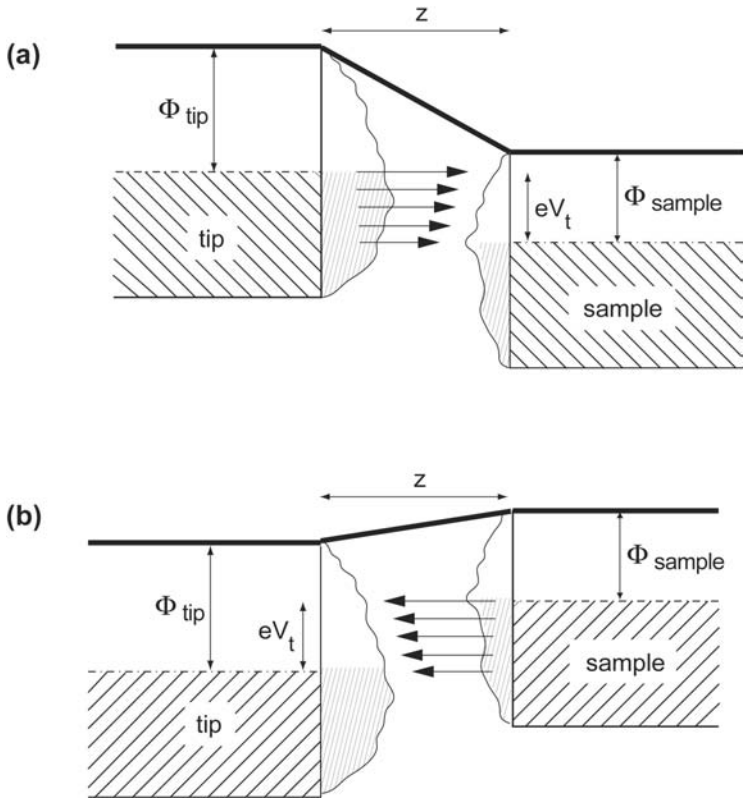

Figure 3.2: Energy level diagram of the sample and the tip. (a) A positive bias is applied to the sample; (b) A negative sample bias is applied.

Eq. 3.1 yields some important results:

- The tunneling current changes of approximately one order of magnitude per Angstrom of separation between the electrodes. Controlling the current value at a precision of one percent corresponds to a precision Δz of 0.01 Å in the tip position, a value which is well below atomic dimensions. To achieve this high resolution, the microscope must be protected and isolated from all mechanical vibrations.

- Only very few atoms at the tip apex contribute to the passage of the tunneling current through the barrier. The nearest neighbors of the apex atom(s) already give an exponentially smaller contribution, as the tunneling current diminishes of a factor of ten per Angström of tip-sample distance. This exponential behavior allows for the high spatial resolution of the microscope.

3.1.2 Modes of operation

The microscope can work in two different configurations, either the *constant-current mode* or the *constant-height mode*. Only the constant-current mode of operation has been employed during this thesis work.

In the *constant-current mode* of operation (fig. 3.3), the tunneling current is amplified by a *current to voltage converter* (IV) and compared to a reference value. The difference between the two is then amplified again to drive the z piezo, and an equibrium z position (corresponding to a voltage V_z) is established through the *feedback loop*. As the tip scans over the x-y plane, a two-dimensional array of equilibrium z positions is obtained, processed by a computer and displayed on the screen. The displayed array of equilibrium z-positions represents a contour plot of the constant tunneling-current surface. It should be kept in mind that the density of states of the Fermi-edge is probed rather than the geometrical structure of the surface (for more details see Sect. 3.1.3).
This microscope operation mode can be used to track **surfaces** which are **not atomically flat**. The corrugation of the surface can be derived from V_z and the sensitivity of the piezoelectric driver element. A disadvantage of this mode is that the finite response time of the feedback loop and of the piezoelectric driver set relatively low limits for the scan speed.

Alternatively, in the *constant-height mode* of operation a tip can be scanned rapidly across the surface at nearly constant height and constant voltage V_z while the tunneling current is monitored. In this case the scan speed is chosen to be much faster than the time constant of the feedback loop or the feedback is completely turned off, so that changes in the tip-sample distance are revealed as variations in the tunneling current. These rapid variations in the current due to the tip passing over surface features are recorded and plotted as a function of scan position.
This constant-height mode allows for much faster imaging of **atomically flat surfaces** since the feedback loop and piezos do not have to respond to the surface features passing under the tip. Fast imaging can prove to be important since it may enable researchers to study dynamical processes on surfaces as well as reducing data-collection time. Fast imaging also minimizes the image distortion due to piezoelectric creep[1], hysteresis and

[1]Creep is the expression of the slow realignment of the crystal domains in a constant electric field over time. If the operating voltage of a piezo is changed, after the voltage change is complete, the remanent polarization (piezo gain) continues to change, manifesting itself in a slow creep.

thermal drifts. In contrast to the constant-current mode, however, the topographical height information is not directly available from the recorded variations of tunneling current (see the relation between tunneling current and z-height presented in the next section) and large corrugations are not accessible.

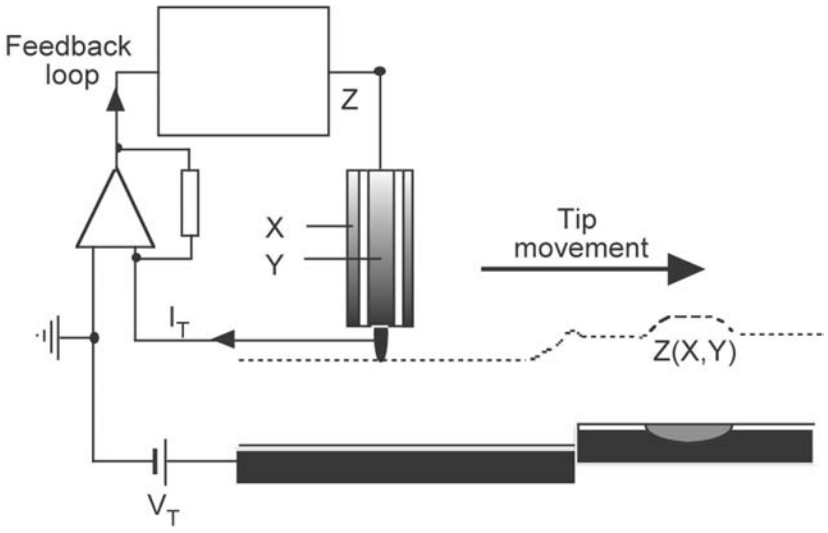

Figure 3.3: Schematic of the constant current mode of operation

3.1.3 Different approaches to tunneling phenomena

The simple, essentially one-dimensional, model we have discussed in sect. 3.1.1 is sufficient for a qualitative understanding of the behavior of an STM. However, treatment of problems such as the lateral resolution of the instrument requires a much more careful consideration of the effect of real surface structure, both of sample and tip, on the tunnel current. Precise simulation of real surfaces requires accurate numerical modelling, but more difficult is the definition of the tip structure, for which extremely idealized models are often used.

Given a particular model of sample and tip, complete calculation of the tunneling current requires two different steps to be achieved. First, the matching of conduction electronic wave functions of sample and tip with a suitable evanescent form in vacuum to find the tunneling probability between tip and sample states. The second step consists, as in the one-dimensional case, in summing over the initial and final states with due regard for the exclusion principle.

Several approximate schemes are available for calculating the tunneling probability.

Bardeen's perturbation theory (1960) has been introduced to achieve a step further in the understanding of the classical tunneling junction experiments. This approach can

provide analytic predictions for both tunneling current and attractive atomic forces. However, for atomic scale phenomena, because of the close proximity of the tip and the sample, modifications to the original Bardeen approach are necessary and the Tersoff-Hamann perturbation theory is introduced.

The Bardeen's approach

The "perturbative-transfer Hamiltonian" approach introduced by Bardeen in 1960 is based on the assumption that **the interaction between the two electrodes is sufficiently weak to be neglected**. In principle, the Hamiltonian of the system electrode-barrier-electrode is made up of three contributions:

$$H = H_L + H_R + H_T,$$

where H_L (H_R) is the Hamiltonian of the left (right) electrode and H_T is the coupling (*transfer*) Hamiltonian. The Bardeen's approach considers as negligible the interaction between the two electrodes, and only the H_T matrix elements appear in the expression of the tunneling current.

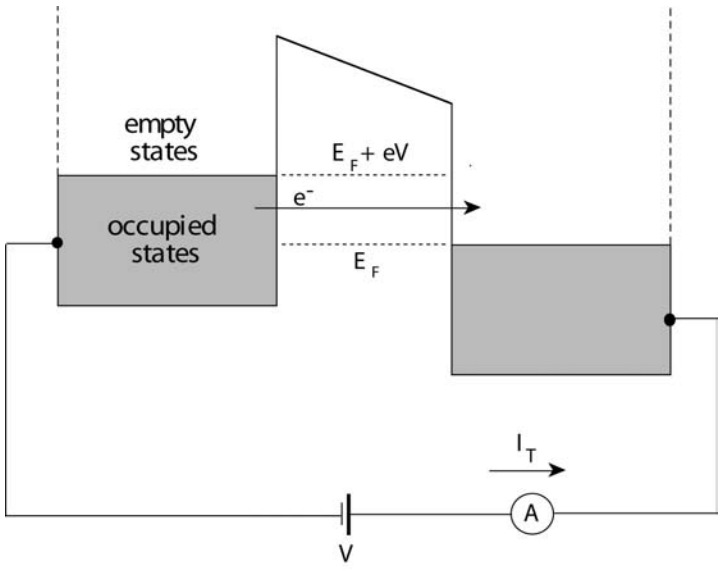

Figure 3.4: Tunneling junction.

Fig. 3.4 shows the tunneling junction, made up of two polarized electrodes separated by a potential barrier. The right electrode is positively biased with respect to the left one.

The expression of the tunneling current is obtained from the *Fermi golden rule*:

$$I = \frac{2\pi}{\hbar} \sum_{\mu\nu} \left[f(E_\mu) \left(1 - f(E_\nu)\right) - f(E_\nu) \left(1 - f(E_\mu)\right) \right] |M_{\mu\nu}|^2 \, \delta \left(E_\mu - E_\nu + eV\right) \quad (3.2)$$

where the eigenvalues E_μ and E_ν are associated to the unperturbed eigenfunctions ψ_μ and ψ_ν of the separate left and right Hamiltonian, H_L and H_R. E_μ and E_ν are given with respect to the left and right electrode Fermi levels.
In the "quasi-equilibrium" state, two different processes are possible: a *direct* current flows if a Fermi electron coming from the left electrode ($f(E_\mu)$ Fermi distribution function) tunnels to an empty state of the right electrode ($1-f(E_\nu)$ distribution), an *inverse* current flows if an excited electron on the right side (probability $f(E_\nu)$) tunnels to a left empty state ($1 - f(E_\mu)$). The conservation of energy impose that $E_\nu = E_\mu + eV$ (the delta-function implies that the electron tunneling is considered to be elastic).
$M_{\mu\nu}$ is the *tunneling matrix element* of the *transfer* Hamiltonian H_T coupling the unperturbed wave functions, ψ_μ and ψ_ν.
At zero temperature and for low voltages, the current is given by the following expression:

$$I = \frac{2\pi e^2}{\hbar} \sum_{\mu\nu} |M_{\mu\nu}|^2 \, \delta \left(E_\mu - E_F\right) \delta \left(E_\nu - E_F\right) \quad (3.3)$$

where E_F is the energy at the Fermi level.
To simplify eq. 3.3, an expression for the tunneling matrix element $M_{\mu\nu}$ is needed. The Bardeen's approach consists in expressing $M_{\mu\nu}$ by introducing a current operator which mixes the wave functions ψ_μ and ψ_ν:

$$M_{\mu\nu} = \frac{\hbar^2}{2m} \int_{S_0} \overrightarrow{dS} \left[\psi_\mu^* \overrightarrow{\nabla} \psi_\nu - \psi_\mu \overrightarrow{\nabla} \psi_\nu^* \right] \quad (3.4)$$

where the integral is evaluated over a surface S which lies completely within the barrier region.
The simplification consists in the fact that the calculation of $M_{\mu\nu}$ requires only the asymptotic forms of the electrodes wave functions, and not their exact value.

The Tersoff and Hamann approach

To model the STM tunneling junction, still in the approximation of weak coupling between electrodes, Tersoff and Hamann have derived a simplified expression for the *tunneling matrix element* by choosing the adequate wave functions [64]. In particular, the tip is considered as a hemispheric free-electron metal, and the electronic wave

function at point $\mathbf{r}$ in vacuum corresponds to the following evanescent form:

$$\psi_\mu = A_\mu \frac{e^{-\kappa|\mathbf{r}-\mathbf{r}_0|}}{|\mathbf{r}-\mathbf{r}_0|} \tag{3.5}$$

where $\kappa = \sqrt{2m_e(\phi - E)/\hbar^2}$ is the decay constant of the evanescent electron wave function, ϕ is the work function and A_μ a constant. $\mathbf{r}$ and $\mathbf{r}_0$ correspond to the position vectors of the considered point in vacuum and of the tip center, respectively.
We suppose that the tip is oriented along the z axis and the sample oriented parallel to the (x,y) plane. To describe the electrons in proximity of the surface, Tersoff and Hamann considered a periodic crystal which yielded a Bloch wave on the (x,y) plane, multiplied by an exponentially-decreasing component along z:

$$\psi_\nu = \psi_{\mathbf{k}_\parallel, E} = \sum_{\mathbf{G}} C_{\mathbf{k}_\parallel, \mathbf{G}} e^{i(\mathbf{k}_\parallel + \mathbf{G})\mathbf{x}} \exp(-\alpha_{\mathbf{k}_\parallel + \mathbf{G}} z) \tag{3.6}$$

with

$$\alpha_{\mathbf{k}_\parallel} = \sqrt{\left|\mathbf{k}_\parallel\right|^2 + \kappa^2} \tag{3.7}$$

where $k_\parallel$ is the wave vector component which is parallel to the sample surface. $\mathbf{G}$ is the general wave vector of the bidimensional reciprocal space and $C_{\mathbf{k}_\parallel, \mathbf{G}}$ are the coefficients of the Fourier development of ψ_ν. $\alpha_{\mathbf{k}_\parallel}$ now corresponds to the decay constant of the evanescent electron wave function, for fixed $(\mathbf{k}_\parallel, E)$.

Inserting 3.5 and 3.6 in 3.4, we obtain:

$$M_{\mu\nu} = -\frac{2\pi\hbar^2}{m} A_\mu \psi_\nu(\mathbf{r}_0) \tag{3.8}$$

with the following expression for the tunneling current, which is a measure of the overlap of the electronic wave functions of tip and sample in the gap between them:

$$I = \frac{e^2 V}{\hbar} \frac{(2\pi)^3 \hbar^4}{m^2} \left[\sum_\mu |A_\mu|^2 \, \delta(E_\mu - E_F)\right] \left[\sum_\nu |\psi_\nu(\mathbf{r}_0)|^2 \, \delta(E_\nu - E_F)\right] \tag{3.9}$$

The second factor in parenthesis corresponds to the local density of states ρ_s of the surface at the Fermi level, evaluated at the point $\mathbf{r}_0$ on the tip: $\rho_s(\mathbf{r}_0, E_F)$. The first factor in parenthesis, on the other hand, is proportional to the tip density of states at the Fermi level, $\rho_t(E_F)$.

We obtain the following fundamental result:

$$I = \frac{e^2 V}{\hbar} C \rho_s(\mathbf{r}_0, E_F) \rho_t(E_F) \tag{3.10}$$

where C is a constant.

The T&H model is based on the approximation of weak coupling between the electrodes and on the validity of Bardeen's conditions (perturbative approach). Moreover, the T&H calculations are only valid at zero temperature and for low voltages with respect to the work function. If these requirements are fulfilled, the current acquisition at different points on the surface allows to realize a *topography* of the local density of states (LDOS) at the Fermi level:

$$\rho_s(\mathbf{r}_0, E_F) = \sum_{\nu} |\psi_\nu(\mathbf{r}_0)|^2 \, \delta\left(E_\nu - E_F\right). \tag{3.11}$$

Chapter 4

Experimental Apparatus

4.1 Overview of the Whole Arrangement

The whole apparatus is an existing one, whose building blocks have been built by the workshop of the institute during the past few years. It consists of three main parts, the *cluster source*, the *deposition chamber* and the *scanning tunneling microscope (STM)*.

Fig.4.1 shows a schematic overview of the experimental arrangement. The Cluster Source and the Deposition Chamber are joined together in a single vacuum chamber. The *Deposition Chamber* houses the thermal atoms source and the equipment necessary for the TEAS (Thermal Energy Atom Scattering) measurements, which includes the helium source and the helium detector. All these tools will not be illustrated here, as they have not been used during this thesis work. For their detailed description the reader is referred to [65, 66].
Facilities, such as an *ion gun* (Sect. 4.2.4) for sample preparation and a *Faraday cup* (Sect. 4.3.2) for accurate cluster current measurements, are also located inside the Deposition Chamber. This chamber contains also the sample/substrate, which is held by its sampleholder.

Both studies performed during this thesis require good vacuum conditions (approximately 10^{-8} mbar) to avoid too much pollution of the sample and assure uncontaminated clusters during the deposition period. The whole system is equipped with a very efficient vacuum system which can achieve UHV conditions, though these high performances are not required in the experiments described in this work. A partial scheme of the existing fore- and turbo- pumping system is sketched in fig.4.1, it excludes the vacuum system related to the STM chamber. For a complete description

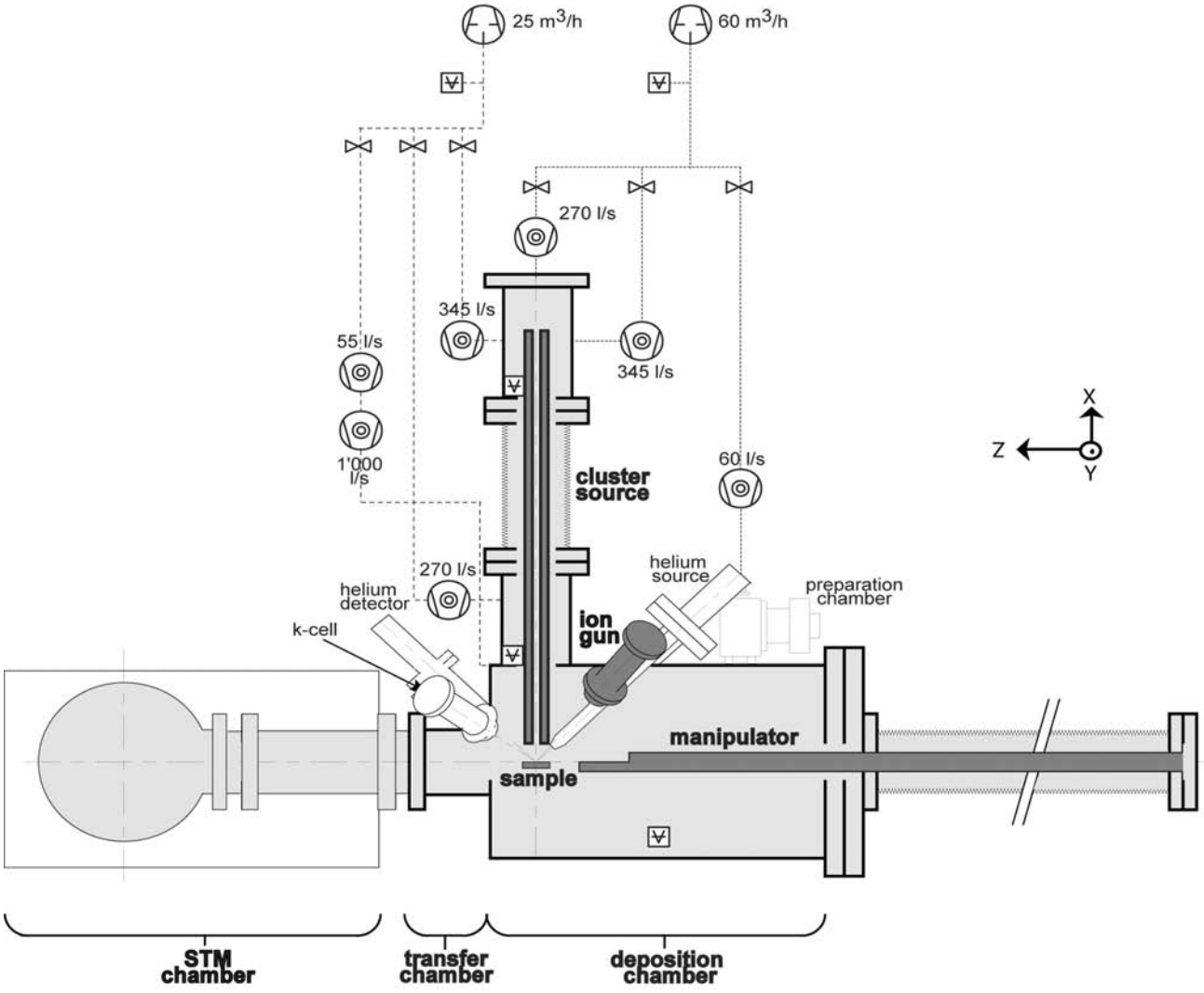

Figure 4.1: Schematic overview of the experimental arrangement. The scheme of the vacuum system of the Cluster Source and the Deposition Chamber is also sketched. The description of the vacuum system of the STM chamber is not shown here, as this chamber has only been used in preliminary implantation measurements performed at atmospheric pressure.

of the vacuum system of the whole apparatus see [65]. In particular, the cluster source is three times differentially pumped by two 345 l/s and one 270 l/s turbomolecular pumps. The pressure in the sputtering chamber, where the clusters are produced, is $3 \cdot 10^{-7}$ mbar during operation, mostly due to the rare gas used for the sputtering process, whereas it can reach $3 \cdot 10^{-10}$ mbar ($\sim 10^{-8}$ mbar in our experiments) when the primary sputtering beam is switched off. A fourth differential pumping stage (270 l/s turbomolecular pump) between the cluster source and the deposition chamber reduces the rare gas contamination towards the latter chamber.
The deposition chamber is pumped by a 1000 l/s turbomolecular pump (which can be backed by another 50 l/s turbomolecular pump for better helium compression during the TEAS measurements), and an additional huge 40000 l/s cryogenic pumping guarantees to reach very low base pressures. This pumping system ensures a base pressure in the low 10^{-12} mbar range, which is beyond the requirements of the experiments described here (typical operating pressures of the order of $10^{-7} - 10^{-8}$ mbar). The side and top views of the experimental arrangement employed during this thesis are shown in fig. 4.2. In the figure the *Transfer Chamber* is also sketched, it has been occasionally used in both experiments to store the samples. This chamber holds a simple system based on a linear manipulator which can stock up to 2 sample crystals together with their sampleholders.

Implantation experiments (IE) as well as *electron emission experiments* (EEE) are based on a controlled deposition of clusters on surfaces.
In the following we will describe the basic procedure of the two experiments, focusing on the tools which are involved in every operation. The reader is referred to the "Experimental procedure" section of Chapters 5 and 6, which summarizes the fundamental steps of IE and EEE, respectively. Future users of the *implantation apparatus* are also referred to Appendix A for all details about the experimental procedure.

- **Preparation of the sample**:
  in *implantation experiments* (IE) the HOPG sample is glued on its *sample holder* (Sect. 4.2.1) and simply cleaned by cleavage with Scotch tape. The sample holder is then screwed on a *support* (Sect. 4.2.1) and inserted into the *Deposition Chamber*.
  In *electron emission experiments* (EEE) the HOPG sample, glued on its holder (Sect. 4.2.2), is first cleaved in air and stored in the manipulator of the *Transfer Chamber*. The sample holder is then clamped by the *main manipulator* (Sect. 4.2.3), transferred into the *Deposition Chamber* and cleaned prior to de-

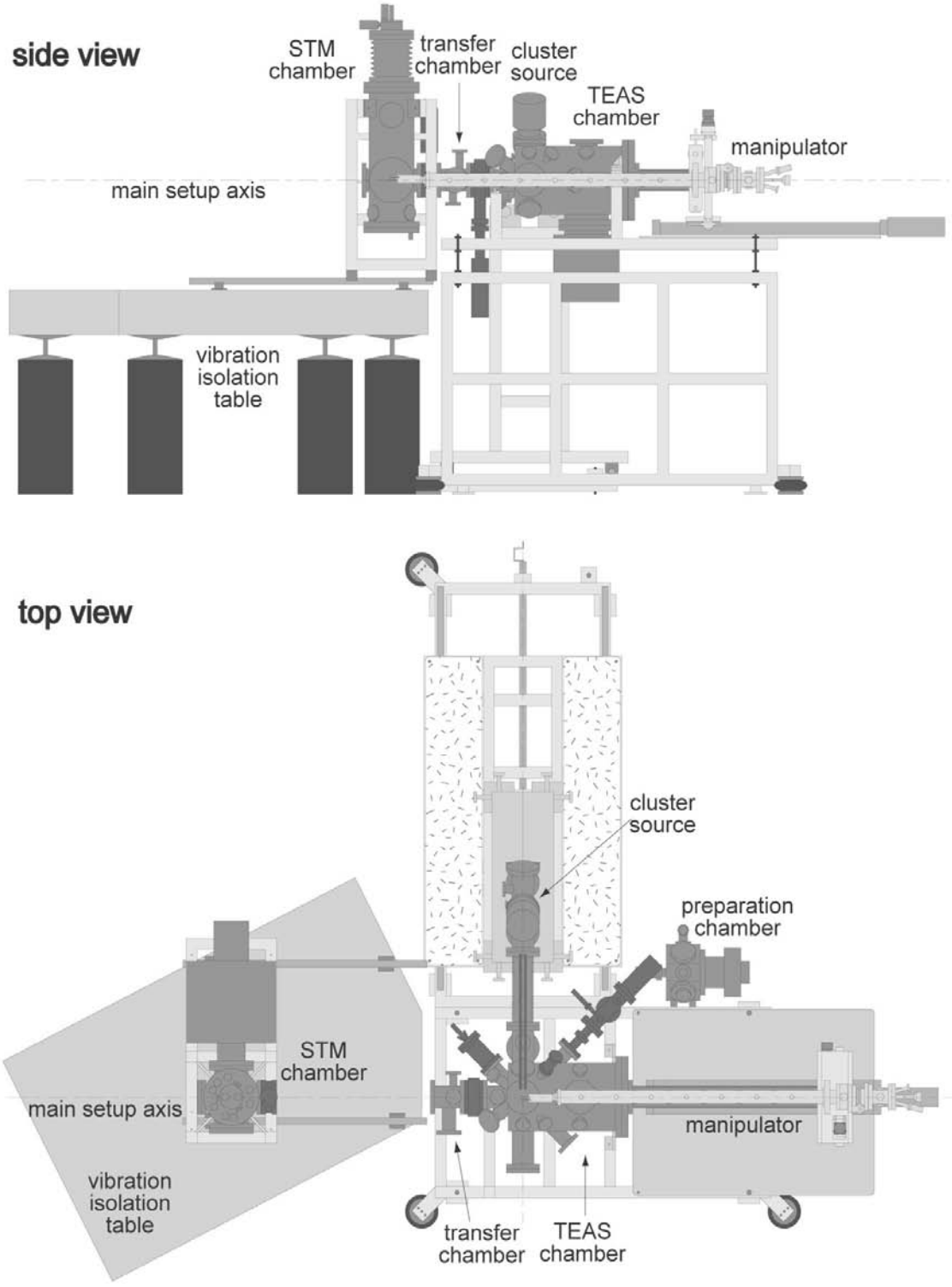

Figure 4.2: Side view and top view of the whole apparatus.

position by an heating filament located on the manipulator head. A high voltage is applied to the manipulator head, and sample cleaning is achieved by electronic bombardment.
When Pt(111) is employed as substrate, cleaning is obtained by sputtering the sample with Ar ions coming from an *ion gun* (Sect. 4.2.4) which is located in the deposition chamber.

- **Deposition of clusters on the surface**:
  In both experiments, the substrate is now irradiated by mass selected clusters. They are produced by sputtering from a *CORDIS ion source*, which will be described in Sect. 4.3.1. A *Faraday Cup* (Sect. 4.3.2) is employed to measure and control the incident cluster current.

- At this point, we can perform two different **analysis**:
  the first one consists in a systematic study of the implantation of clusters into the HOPG substrate. After implantation, the sample is oxidized in a *furnace* (Sect. 4.4.1) to obtain wide etch pits of the same depth as the implanted clusters. The topography of the sample is finally analyzed by a *Scanning Tunneling Microscope* (Sect. 4.4.2)
  The second experiment consists in studying the electron emission following the impact of clusters on the substrate. This experiment requires an *electron detection system* (Sect. 4.14), which includes the electron detection device and the system of control and data acquisition.

In the following the reader will find a detailed description of all the tools involved in the three experimental steps of preparation, deposition and analysis, cited above. If the described tool is specific to one of the two experiments, this will be specified in parentheses in the section title (IE stands for *Implantation Experiments*, and EEE for *Electron Emission Experiments*).

4.2 First step: Preparation of the sample

4.2.1 The Sample holder and its support (IE)

For sake of completeness, we should mention that this sample holder and its support have been designed for "high-energies" implantation measurements (impact energies higher than 2 keV). During "low-energy" measurements the sample was glued on the sample holder described in Sect. 4.2.2, which was clamped by a manipulator (Sect. 4.2.3). The

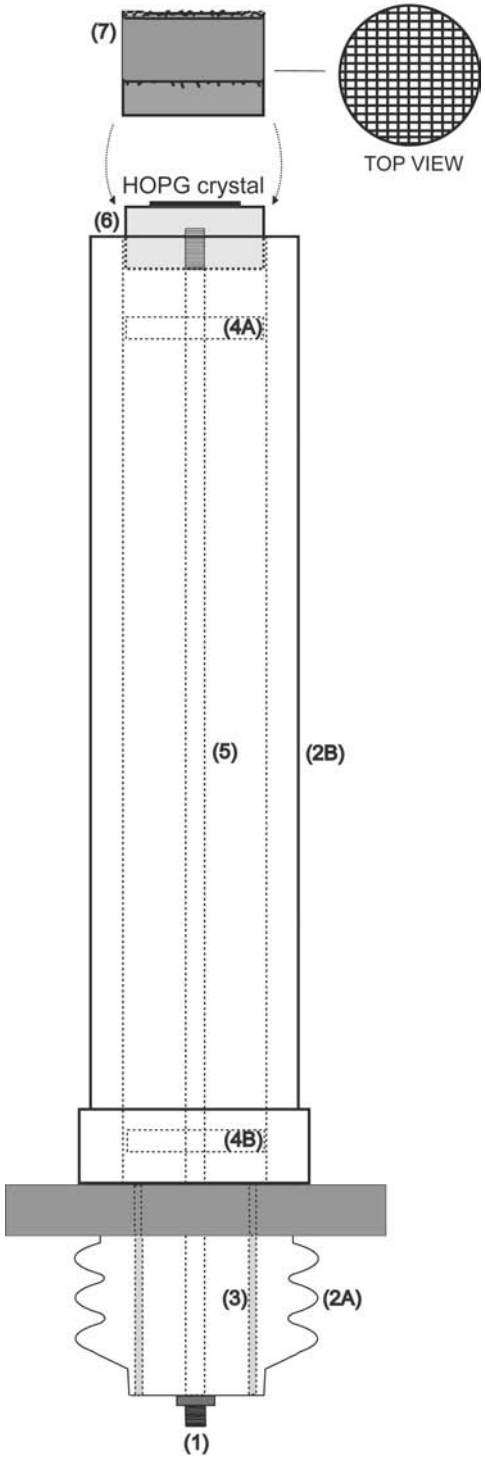

Figure 4.3: Detailed view of the sample holder, its support, and the protecting grid (IE).

voltage applied on the sample defines the impact energy of clusters on the surface. In this setting, the potential on the sample is established by biasing the manipulator head. As the manipulator head does not support high voltages, this setting is only suitable for low-energies measurements. For simplicity, in the course of measurements, the "high-voltages" setting has been used for both low- and high-energies implantation data.
Fig. 4.3 shows a schematic view of the sample on its sample holder (6), covered by the protecting grid (7) and screwed on a support which allows to establish an electrical contact between the sample and the exterior of the chamber. In particular, during the implantation of clusters into the surface the sample bias comes from a high voltage generator which provides negative voltages up to 30 kV.
The protecting grid is in electrical contact with the sample holder. This grid allows the incident cluster beam to reach the sample, but avoids the presence of a strong electric field on the sample surface.
The HOPG crystal is glued (with a vacuum-compatible electrically-conducting silver paste) on a very simple sample holder (4), consisting in an aluminum cylinder (diameter $\sim$1 cm) with a hole to be screwed on the long metallic rod (5) which electrically connects the sample to the exterior (1). The teflon (PTFE) disks (4A,4B) are used to center the rod and to isolate it from the internal metallic cylinder (3). The external part (2A) as well as the cylinder (2B) are made of electrically insulating materials (ceramic and teflon (PTFE), respectively).

4.2.2 The Sample holder (EEE)

The sample holder is made out of two molybdenum pieces which are spotwelded together, as shown in figure 4.4. The crystal is solidly attached to the lower ring with small tantalum sheets spotwelded to the ring. The sample holder is clamped by the manipulator on two small wings on the upper molybdenum piece. The space behind the sample inside the sample holder is empty, allowing the filament of the manipulator to be placed as close as possible behind the crystal to obtain a very efficient heating. Two thermocouple wires (type K) are spotwelded at the edges of the sample, as near as possible to the surface. They are then guided to the top of the sample holder via two small ceramics and slightly twisted on top of these in order to form two small point contacts insulated from the sample holder. When clamping the sample holder on the manipulator, one forces the two thermocouple spring contacts of the manipulator head to connect these point contacts.

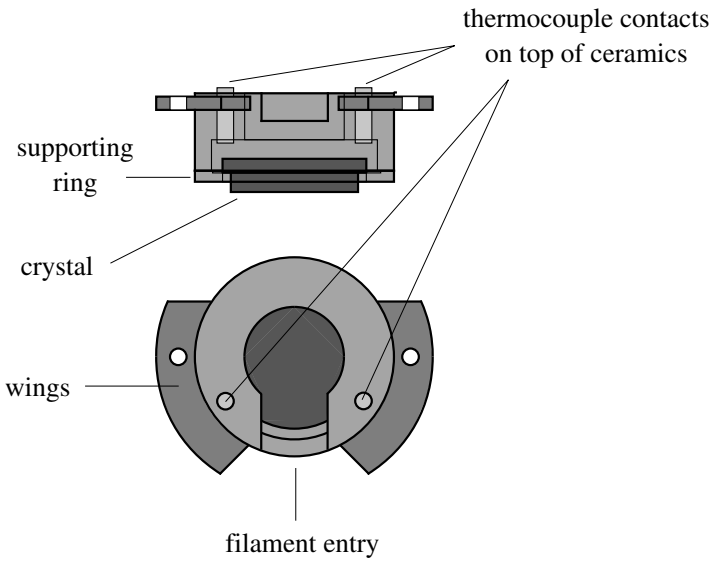

Figure 4.4: Detailed view of the sample holder (EEE).

4.2.3 The Manipulator (EEE)

The design and construction of the manipulator has been one of the main tasks of Renald Schaub during his PhD thesis. For a detailed description of its design and performances the reader is referred to [65].
The manipulator holds the crystal and its sample holder during deposition and during the sample cleaning, performs small displacements of the sample, and occasionally transfers it into the Transition Chamber.
Precise displacements of the sample are assured by the high rigidity of the system. Moreover, in order to investigate the electron emission as a function of cluster incoming kinetic energy, an appropriate potential has to be established on the sample by biasing the manipulator head. The latter is then equipped with a good electrical insulation.

The manipulator consists of a functional head supported by a long rigid support tube. The whole unit is fixed on a rotary CF100 flange, which is mounted on a mechanical system performing the movements of the manipulator in x-, y-, and z-directions, as well as the θ rotation around its axis. All these displacements are either manually operated or controlled by computer.
The sample transfer procedure implies that the sample is not rigidly fixed on the manipulator. Fig. 4.5 illustrates the clamping system of the manipulator. The filament for sample cleaning is also sketched, with the thermocouple contacts which allow to measure and control the temperature of the sample.

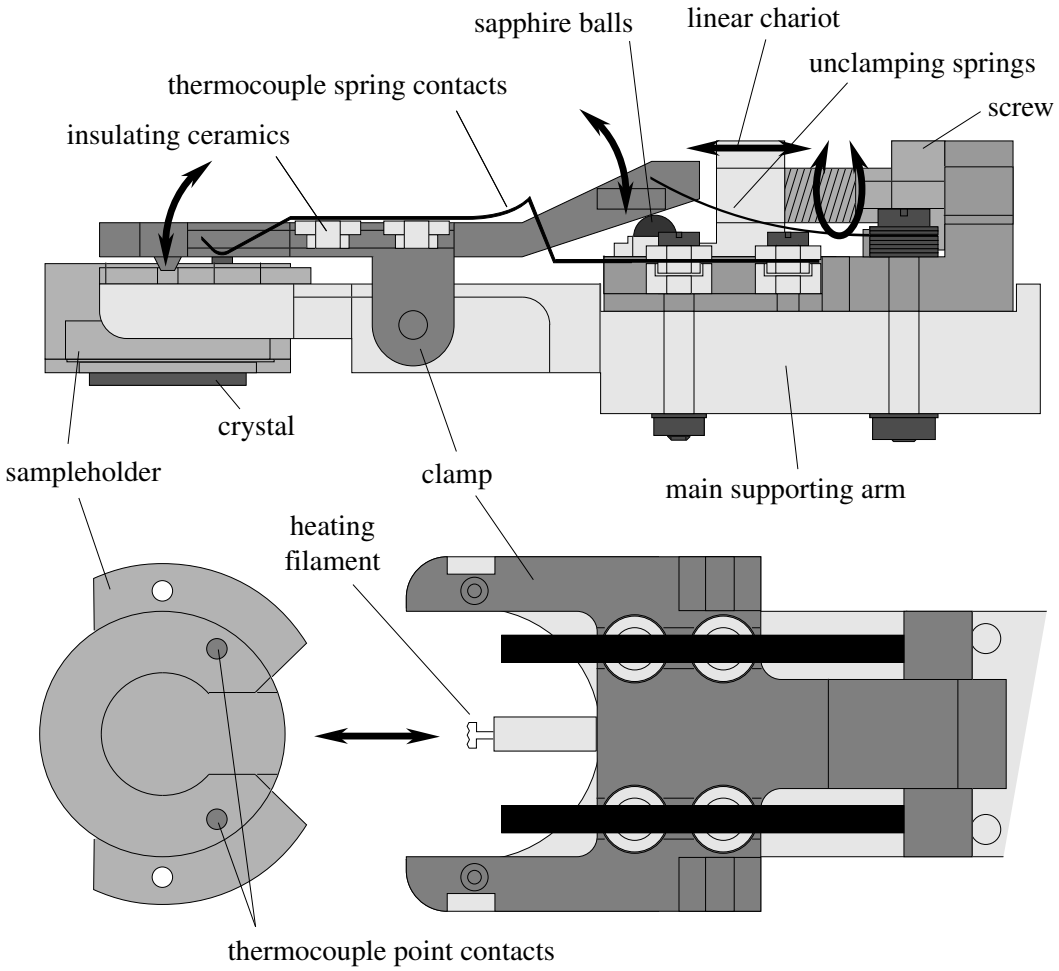

Figure 4.5: Detailed view of the head of the manipulator (EEE).

4.2.4 The sputtering gun (EEE)

When the Pt(111) crystal was used as substrate, it was cleaned by sputtering the surface with Ar ions. We typically used a $0.1\,\mu A$ ion beam of 1000 eV, produced by an ion gun (type IQE 12/38 from Leybold[1]) which forms the ionized atoms into a beam by means of electrostatic lenses and two collimating differentially pumped chambers. This pumping is ensured by a turbo-molecular pump, attached to the preparation chamber which is completely independent of the whole experimental setup, via two UHV tubes provided with gate valves. The beam is then directed on the center of the sample, thanks to electrostatic deflection plates. Finally, the manipulator is used to perform an in-plane scan of the sample surface.

[1]Leybold-Heraeus GmbH, Bonner Strasse 498, D-50000 Köln

4.3 Deposition

4.3.1 The Cluster Source

The cluster source is described in details in the thesis of G. Vandoni [67] and schematically represented in fig. 4.6.

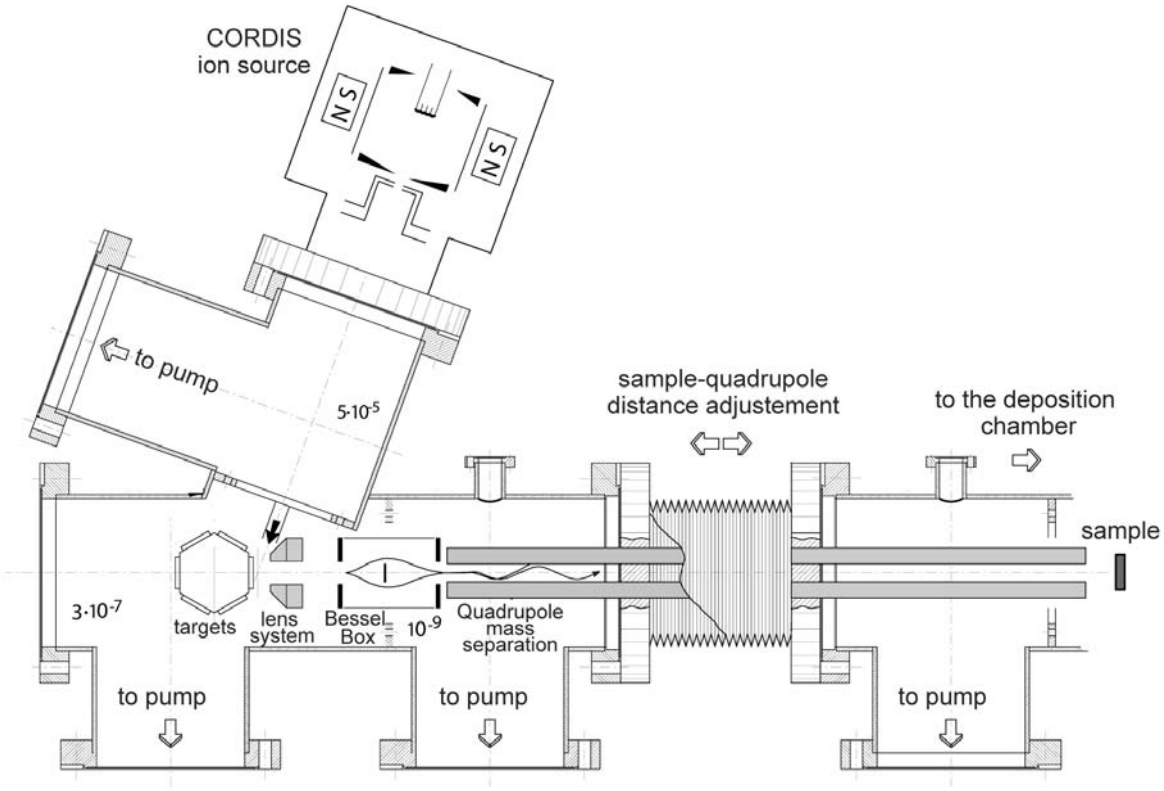

Figure 4.6: Schematic of the cluster source joined to the Deposition Chamber.

Clusters are produced by sputtering from a CORDIS (Cold Reflex Discharge Ion Source) ion source which generates a 20 keV rare gas ion beam. Typical primary beam currents are of the order of 5 mA. The ion beam is focused on a sputter target by an electrostatic secondary lens. Cations are extracted by a series of electrostatic lenses and focused into an energy filter of the Bessel-box type. This filter stops the neutrals and performs an energy analysis of the atomic and cluster cations with an energy window of $\pm$ 7.5 eV. Finally the ions enter the quadrupole, which allows for mass separation up to 5000 amu. A typical mass spectrum of silver cations is shown in fig. 4.7.

Mass-selected clusters are projected at normal incidence onto the surface. The resulting distribution of deposited clusters on the surface has approximately the form of a gaussian distribution. Its FWHM depends on the distance between the quadrupole

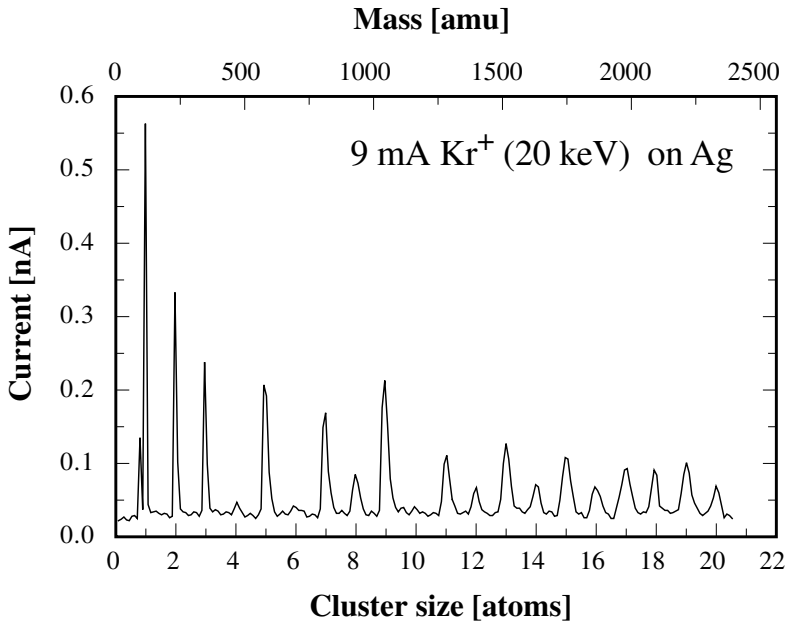

Figure 4.7: Typical mass spectrum of Ag ionized clusters, with a primary Kr^+ current on the silver target of 9 mA and a beam energy of 20 keV. Notice the odd-even alternation and the magic numbers (n = 9), related to the electronic shell structure.

and the surface ($\simeq$ 1 cm), and on the energy of the clusters. For a sample-quadrupole distance of approximately 1 cm and for low impact energies (up to $\sim$ 1 keV), the FWHM of the distribution measures $\sim$ 1 cm.
The impact energy of the clusters is controlled by the bias voltage applied to the sample, and the coverage is determined by the beam current density and the deposition time.

4.3.2 The Cluster Current Reading Device

The two studies performed during this thesis require a precise control of the deposition rate of impinging clusters, in terms of atoms per unit area and unit time. The simplest way to measure the cluster current during deposition is to use the sample as a reading device. An accurate electro-meter (pA to nA range) connected to the sample would yield this information. Unfortunately, the electromagnetic coupling between the quadrupole and the sample depending on the amplitude of the radio-frequency applied to the quadrupole bars, perturbs the cluster current measurement. As we had to deal with very low current values (down to some picoamps), we found a different solution to measure the cluster current.
For electron emission studies, an existing home-made device [65] has been used, which was based on the Faraday cup principle (figure 4.8). An electrically insulated collecting

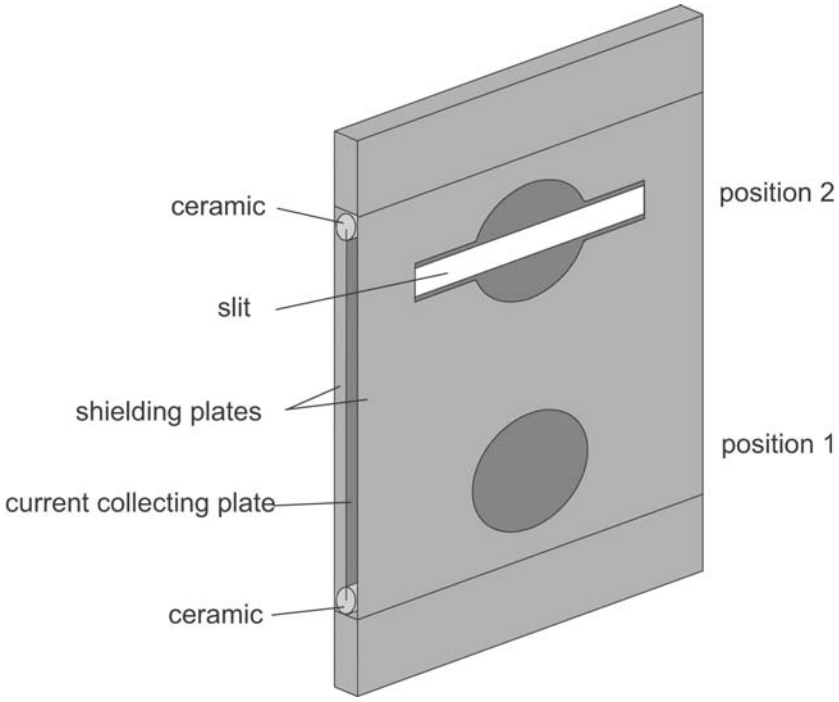

Figure 4.8: Drawing of the cluster current reading device (EEE), based on a Faraday cup. The electrically insulated collecting plate is shielded by two external plates. The device offers two measuring positions: position 1 being placed in front of the quadrupole allows us to measure the total cluster current; if position 2 is placed between quadrupole and sample, a fraction of the total cluster current can be measured.

plate is located between two external shielding plates, which can be either grounded or biased. The whole device is 1.5 mm thick, and can be easily placed between the sample and the quadrupole. It provides two different cluster current reading modes depending on its position in front of the quadrupole. Position 1 allows us to measure the total cluster current, within position 2 a fraction of the total cluster current can be measured. In electron emission studies, this reading device was fixed to the whole detection system (Sect. 4.14), with position 2 located in front of the quadrupole. This allowed us to measure (a fixed portion of) the cluster current during deposition.

Another device has been designed during my thesis, which was also based on the Faraday cup principle. This device was invented to simultaneously measure the cluster current and the electron current in preliminary experiments of electron emission (it was then replaced by the reading device described above). It was composed by a plate with a central hole, to measure the incident cluster current, followed by a semi-sphere working as collecting plate of the emitted electron current. A shielding external plate protected the measurements from external perturbations.

This home-made device has been actually used for implantation studies, with the only requirement of measuring the incident cluster current. The collecting plate of the electron current was connected to the ground.

With both reading devices, a *Keithley* electrometer collects and measures the cluster current, with a stability which is better than 1 pA. This quantity has to be compared to some picoamps, the minimum total current employed in our studies (see section 5).

4.4 Analysis

4.4.1 The oven (IE)

After implantation, the sample is oxidized to obtain wide etch pits of the same depth as the implanted cluster.

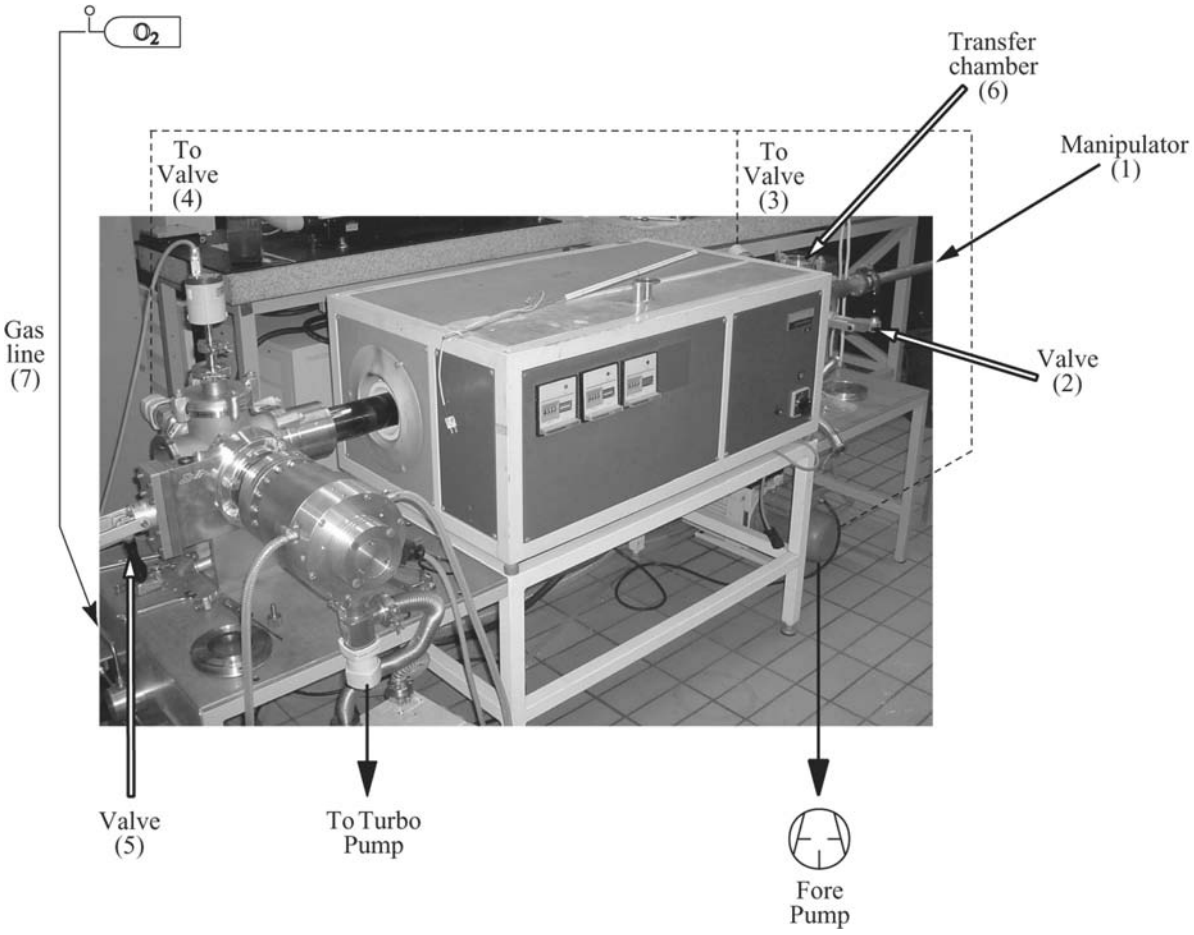

Figure 4.9: The oven employed for the oxidation of the sample.

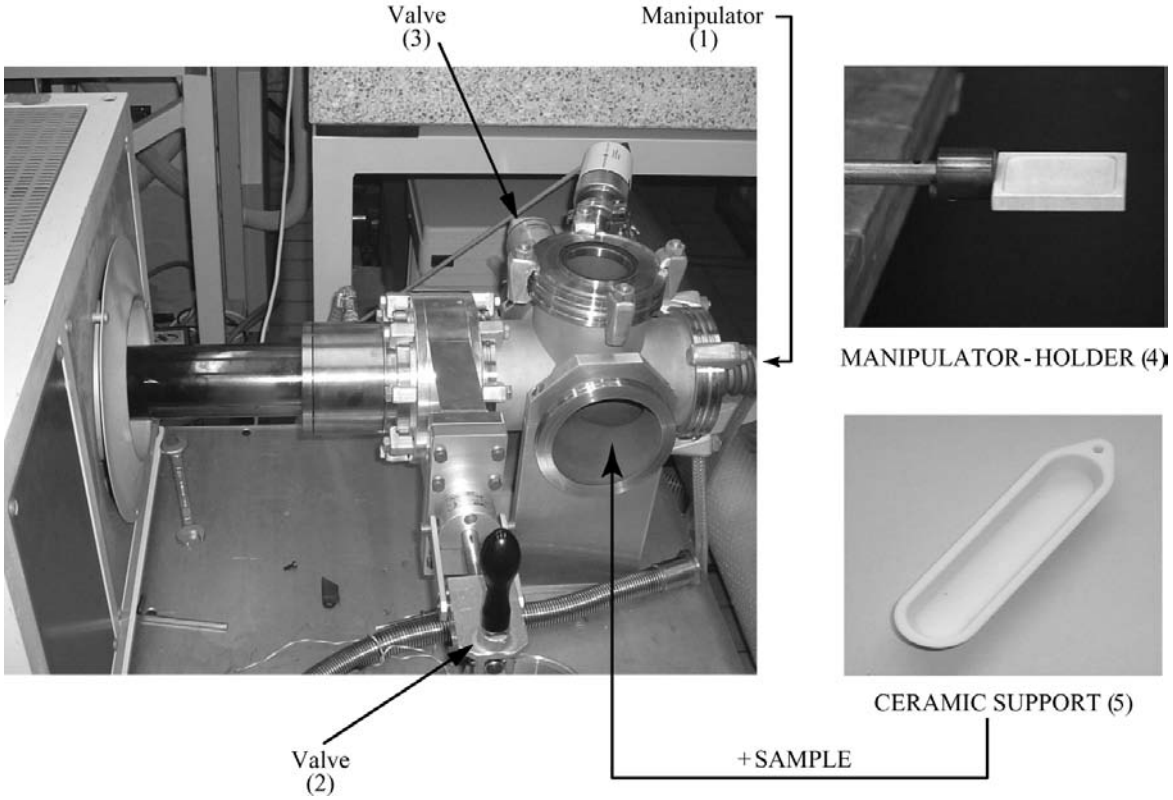

Figure 4.10: Picture of the *transfer chamber* of the oven. The ceramic support (5), which contains the sample, is placed on the manipulator-holder.

Fig. 4.9 shows a picture of the furnace employed for the oxidation of the sample. It is mainly composed of two chambers, a *main* chamber and a *transfer* one, connected together through the valve (2). A turbo-molecular pump, which can be isolated from the main chamber through valve (5), allows to reach a vacuum of the order of $10^{-5} - 10^{-6}$ mbar.

The temperature of the furnace can be manually fixed by a temperature controller, and heating is performed through an heating coil. The temperature is homogeneous in a volume of approximately $10^{-3}\, m^3$ around the center of the chamber.

Different gas lines allow to mix various gases, with the possibility of controlling the partial pressures of each of them. During our experiments only one entry has been used, which provided the 100 mbar of oxygen necessary to oxidize the sample[2].

The transfer chamber (6) is shown in details in Fig. 4.10. Once the transfer chamber has been decoupled from the main one (valve (2)), the ceramic support (5) containing the sample can be posed on the manipulator holder(4). The manipulator allows to move the sample back and forward from the transfer chamber to the main one.

[2]Occasionally another gas entry was used, to break the vacuum in a clean way through nitrogen.

4.4.2 The STM microscope (IE)

The last step in the experimental procedure of implantation experiments consisted in analyzing the topography of the sample with a Scanning Tunneling Microscope.
The design and construction of this microscope has been one of the main tasks of Pierre Convers during his PhD thesis. For a complete description of the microscope, the reader is referred to [68].
We should mention that this microscope has been conceived to work in ultra-high vacuum and at low temperature. It is then inserted into a chamber, which contains two concentric bath cryostats. Preliminary implantation measurements have been done with the microscope inserted into the chamber but working in air, in order to test the whole system. In a second time, as for implantation measurements we need neither high vacuum nor low temperature, a compact STM prototype was built, based on the same design as the first microscope and containing only the fundamental tools to approach the sample and scan its surface.

The following paragraphs summarize the design of the scan head and the STM control electronics. We will skip off the description of the STM chamber used in preliminary measurements. For all the details about this chamber and its cooling system the reader is referred to [66].

The Microscope

A detailed view of the head of the microscope is given in figure 4.11. This microscope is a "home-built" STM in air, whose coarse approach mechanism is based on Pan's design [69, 70]. This microscope is made of two moving parts, the approach sledge bearing the scanner tube at its lower end, and the sample drawer which can move in the x,y directions.
The approach sledge is a polished ceramic prism placed in a V-shaped groove where it is rigidly clamped by two triplets of shear piezos (Steveley Sensors, East Hartford, CT 06108). A sapphire pad is glued on top of each shear piezo. These pads provide the actual contact areas between the piezos and the prism surfaces. Four of the piezos are glued on two ceramic bars which are glued to the whole Macor body. The last two piezos are glued on a third ceramic bar, which is pressed onto the prism by means of a spring and a small inox sphere. This system warrants an equal distribution of the spring force to all contact areas of the six shear piezos and the prism surface.

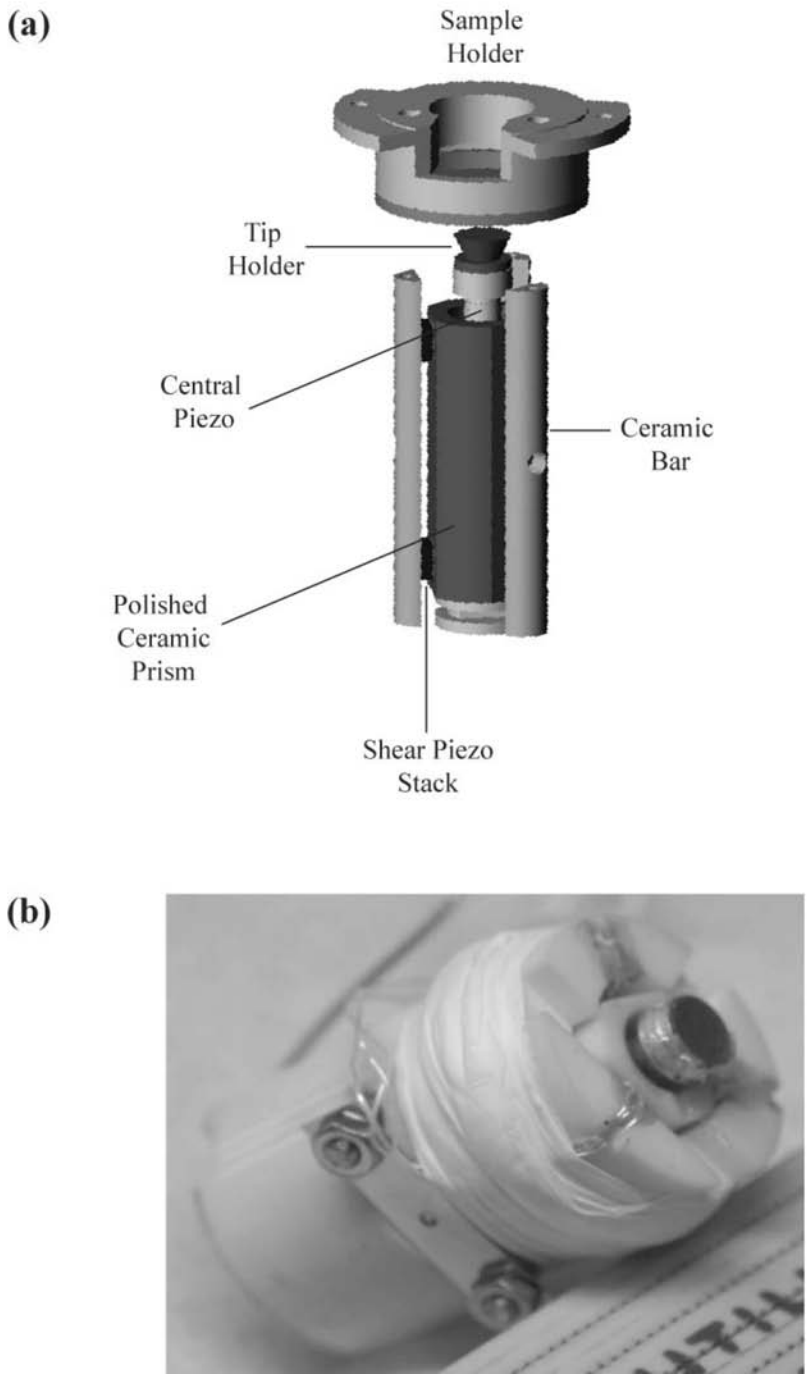

Figure 4.11: (a) Schematic drawing of the *scan head* of the microscope. This mechanism controls the approach-withdraw movement of the tip and the scan movement of the tip on the surface. The sample holder is also shown. (b) Photo of the scan head of the microscope. The z-piezo is completely up.

As proposed in ref. [71], we did not employ walker stepping as a working mechanism but use inertial movement by applying an asymmetric saw-tooth voltage curve to all six stacks simultaneously (*stick and slip*). On the flat slope of the voltage ramp the prism follows the shear movement (stick), while, due to its inertial mass, it is unable to follow the rapid relaxation of the piezos on the steep slope (slip), the result being one step of the prism per period. The step size can be tuned by varying the applied voltage amplitude (200 nm corresponding to the maximum step amplitude, at 300 K), and the frequency can be chosen by the user (typical value of approximately 1 khz).
The central piezo holding the tip is glued to the lower end of the prism. The tip approach towards the sample to approximately 1 mm distance can be carried out automatically with the "fast movement" option. To complete the operation the "fine approach" is accomplished. During a measurement the sapphire prism stays firmly clamped to the microscope body. The scanner in use is a 1/8 in. EBL No.2 piezo tube with a length of 16 mm.
In the microscope operating in vacuum, shear piezos allow the drawer containing the sample to move on the x-y plane, making maximum displacements of the order of a few millimeters at minimum steps of the order of 200 nm. We will not enter into the details of the x-y movement, as in the prototype which has been used for most of the implantation measurements the displacements on the xy plane have been performed by manually moving the drawer containing the sample.
The STM prototype works in the "constant current mode", at ambient conditions of temperature and pressure. Images are taken at typical currents of the order of $1-2\,nA$ and bias voltages of approximately $1-2\,V$ (the sample is positively biased respect to the tip).

To guarantee the good performance of the STM, it must be isolated from environmental vibrations. During measurements the compact microscope has been placed on a vibration isolation table and protected in a cage to be electrically and mechanically isolated.

The STM Control Electronics

A commercial STM control unit STM 200, developed by RHK Technology Inc., is used for the feedback control and the data acquisition. It is equipped with a 16 bit A/D converter for the data acquisition which provides a fine graduation of the absolute height information as well as a sufficiently large dynamical range allowing to solve typical experimental problems as inclined scanning plans or drift in the z-direction.

The tunneling current is amplified by an home-built current-to-voltage converter. This converter (based on an existing design, see ref. [72]) is constituted by a pre-amplifier followed by a system of filters. It provides an amplification of $3 \cdot 10^8$ V/A. The amplifier is connected as close as possible to the beginning of the current-signal wire to avoid any perturbation. The noise level amplitude below 1 Khz (i.e. once the filters are inserted), corresponding to the signal received by the RHK in absence of tunneling current, is approximately 5 mV. The power for the amplifier is supplied by four rechargeable accumulators to avoid 50 Hz noise.

The STM 200 electronics is interfaced by an Indigo workstation by Silicon Graphics. Various features as tunneling spectroscopy or advanced image treatment are implemented in the controlling software.

4.4.3 The Electron Detection System (EEE)

A sketch of all the instruments involved in the electron emission detection is presented in Fig. 4.12.

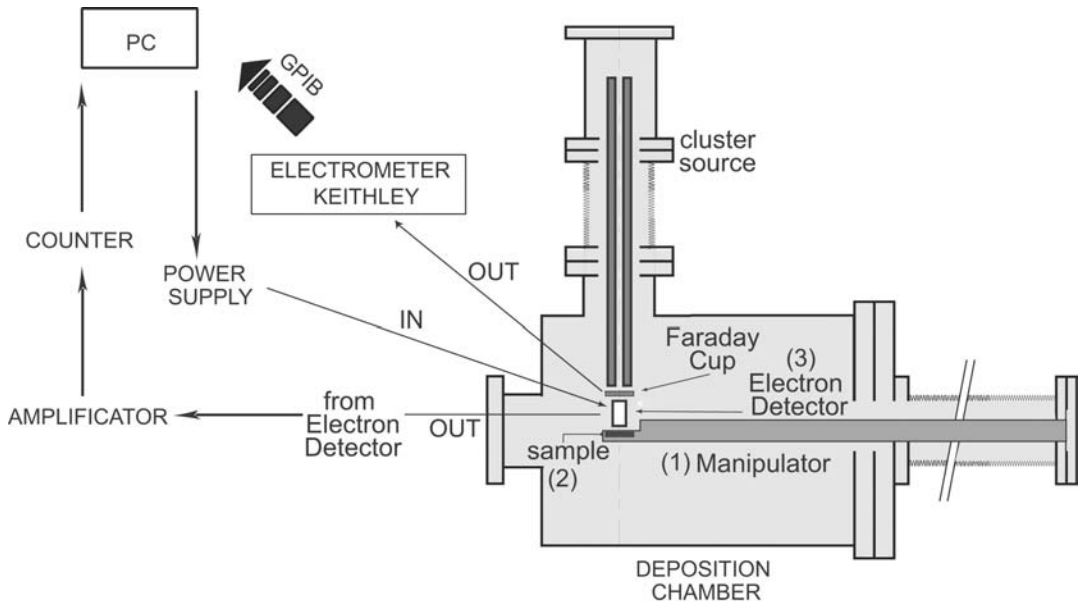

Figure 4.12: Scheme of the *electron emission* detection.

The electron detector efficiency

The cluster source produces clusters at a fixed kinetic energy of approximately 90 eV. To vary the clusters impact kinetic energy we have to vary the bias on the sample. To obtain meaningful results, it is necessary that the *detection efficiency* η[3] remains constant with the changing sample bias. This assures that the recorded current variations correspond to variations of the electron emission and not of the detector efficiency. Moreover, it would be necessary to measure the incident cluster current, to be able to determine the ratio γ between the emitted electrons and the incident cluster current. Due to the high voltages applied on the sample (up to 1000-2000 V), it is impossible to directly measure the cluster current which hits the sample surface.

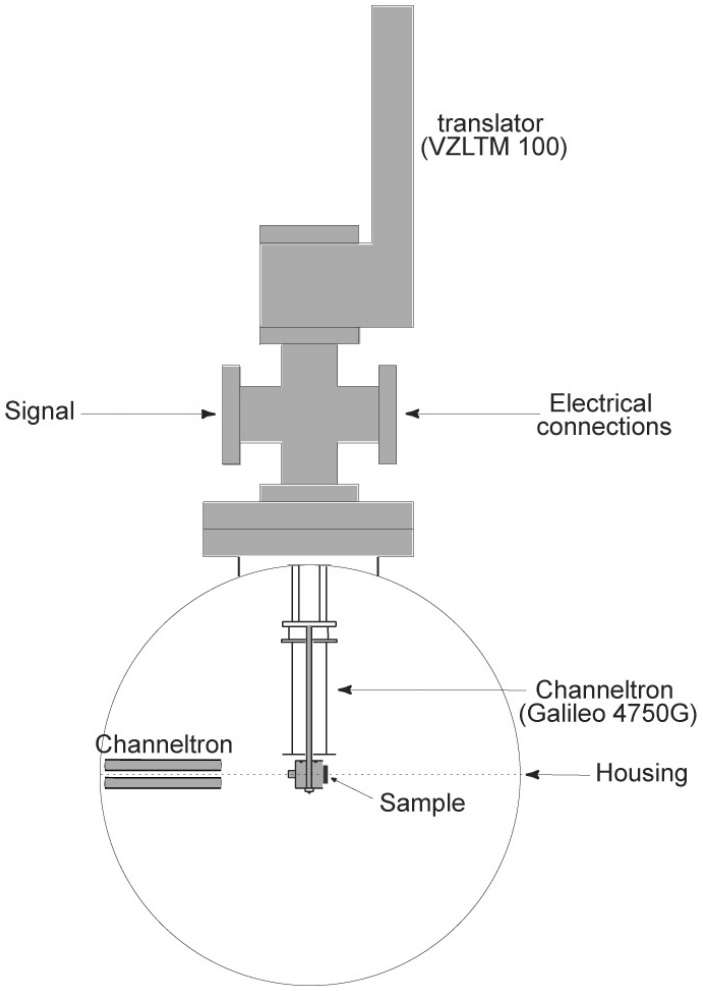

Figure 4.13: Global view of the detector.

Two different systems have been tested for measuring the ratio η: the first one

[3]corresponding to the ratio between the number of detected and the number of emitted electrons

employs a double Faraday Cup to measure at the same time the cluster current and the electron current. The second system is based on a Channeltron, which measures the emitted electron current, coupled with a Faraday Cup to measure the incident cluster current.

Testing both systems has been the main task of P. Convers diploma work. We will not enter into the details of the first arrangement, as it has never been used during this thesis work, and it proved to perform wrong and noisy measurements. For details, see ref. [73].

The "channeltron" system proved to be the most adapted between the two. However, in its first setting it originated very noisy measurements. Various improvements with respect to the original configuration made it even more reliable. Particular efforts have been spent to avoid clusters to hit metallic surfaces and produce emitted electrons which perturbed the measurements.

The electron detection device

The electron detection device (Fig. 4.13) is mounted on a CF35 flask. The hole of the collimator is placed in front of the quadrupole. The sample can be precisely positioned back to the metallic box, the center of the sample being aligned with the axis of the quadrupole-collimator system. The translation system allows a vertical displacement of the whole detector of almost 10 cm, useful in different operations which require large displacements of the manipulator.

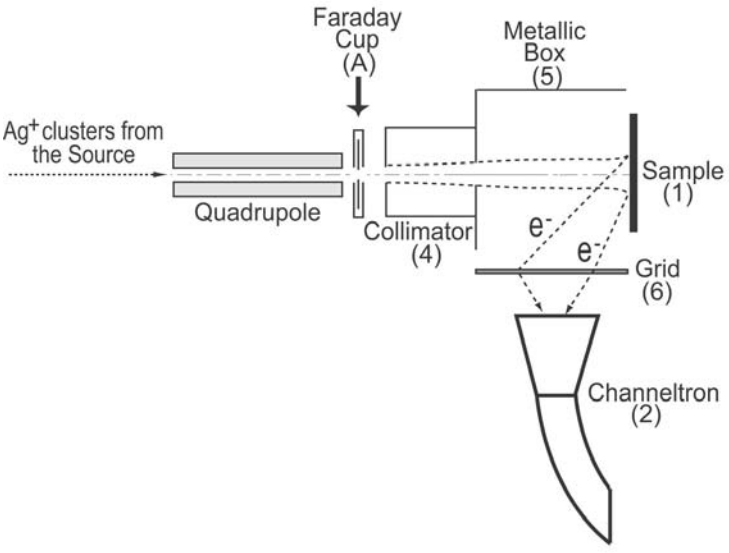

Figure 4.14: The components of the detection system.

Fig. 4.14 shows a detailed view of the components of the electron detection system. The detector is placed between the quadrupole and the sample (1) and it is maintained at a fixed positive potential with respect to the surface. The potentials on the metallic box (5), the grid (6) and the sample (1) vary as the energy of the cluster beam varies, in order to maintain the detector efficiency constant. As a matter of fact, the detector efficiency remains constant during measurements if all the potentials remain constant with respect to the sample bias. The incident cluster beam current is measured by the Faraday Cup (A). A well defined fraction of the beam passes the FC, is collimated (4) and hits the sample surface which is negatively biased. The emitted electrons which reach the grid (6) are accelerated by the high potential of the channeltron (2) and detected.

The control and data acquisition system

The potentials applied on the various numbered components of Fig. 4.14 are all defined by a power supply controlled by the computer.
Fig. 4.15 represents a general scheme of the control and data acquisition system. The control and data acquisition is performed by a VEE TEST [4] program on a PC. The computer controls all the potentials of the constituents of the detector, changes these potentials by user-defined steps, and at each step acquire both the incident cluster current and the current of emitted electrons.
In particular, all the required potentials are defined by a reference potential, V_{ref}. The computer controls the power supply and set the (negative) potential V_{ref}. The potential difference between (6) (the grid) and (7) (the channeltron end) is maintained fixed during measurements. V_{ref} controls also the potentials of the box and of the sample. In particular, in the last configuration of the detector, the parameters "a" and "b" were both set equal to zero, thus assigning the same potential V_{ref} to the grid, the sample and the metallic cage. In this way, the incoming cluster beam is not deviated by the grid potential, as it moves in a constant potential environment. The disadvantage is that the detected electrons are only that proportion of emitted electrons which hits the grid and enters into the channeltron. Anyway, this proportion remains constant during measurements. Moreover, the potential V_{ref} also defines the voltage applied to the collimator. In particular, a positive voltage of 27 V is added to V_{ref}, in order to avoid that noisy electrons emitted by cluster impact on the collimator have a sufficient energy to enter into the channeltron and be detected.

[4] VEE-test is a graphical working space, allowing to model different instruments controls as graphical blocks, which can then be combined with each other in block diagrams.

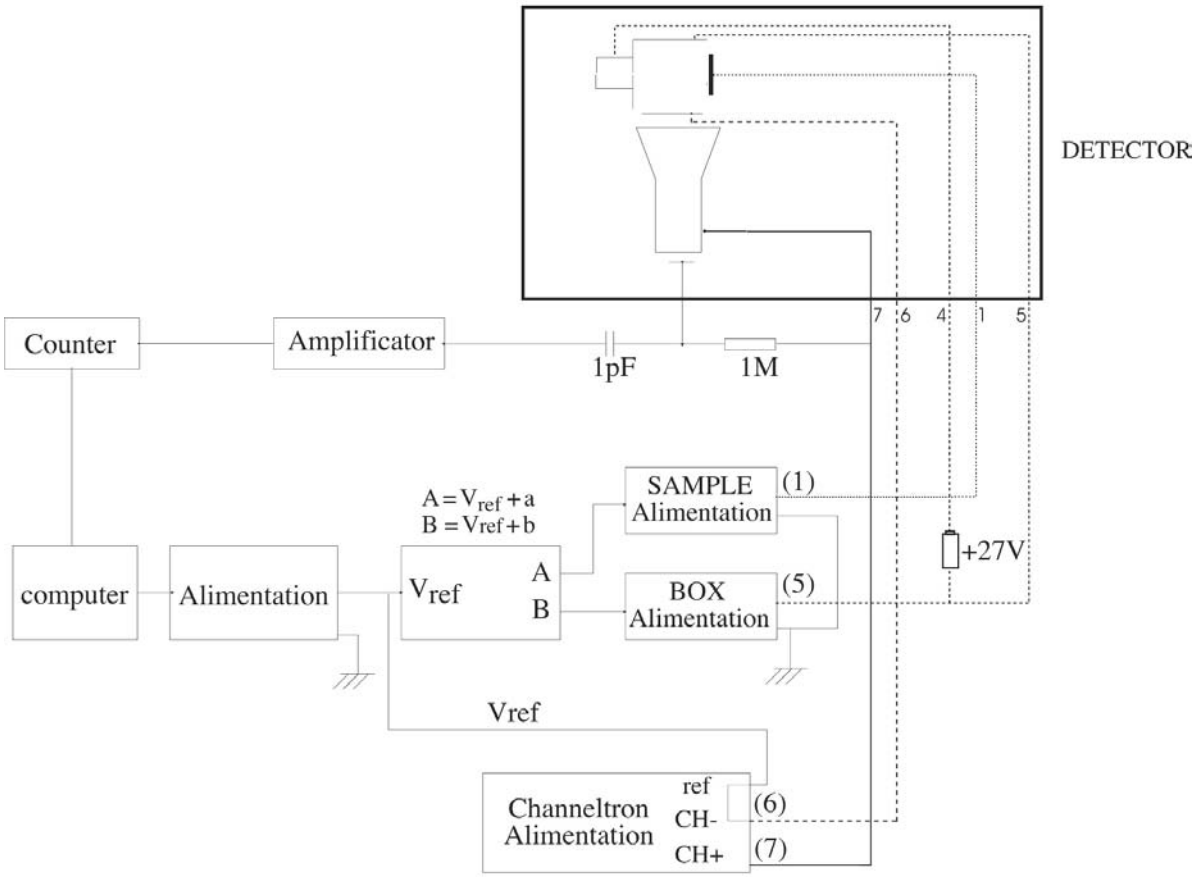

Figure 4.15: The schema of the control and data acquisition system.

Thus, the voltage V_{ref} is one of the inputs the user must enter before running the program.

In addition to this voltage, the user has also to define the voltage step and the waiting time between one step and the following, time required to stabilize the cluster current and the emitted electron current. At each voltage step,the output signal (the detected electron current) is amplified, measured by the counter and stored by the computer. The PC then receives by the Keithley electrometer the information about the incident cluster current (measured by the Faraday Cup). The ratio between the two currents corresponds to the quantity of interest of these measurements.

Chapter 5

Implantation of silver clusters into Graphite

In this chapter a systematic study of the implantation of size-selected Ag_N^+ clusters into a graphite sample is presented, for different cluster sizes (N=1,3,7,9,13) and for incoming kinetic energies ranging from 1 to 30 keV. Results show that for all sizes the implantation depth scales linearly with a "scaled" cluster momentum. The stopping power of the cluster while penetrating the HOPG surface is also investigated for each cluster size, and a "molecular effect" is recognized.

5.1 Introduction

The controlled deposition of clusters preformed in the gas phase, at incident kinetic energies which are larger than a threshold value, allows to pin the clusters to their impact point yielding well-defined and very stable vertical structures. The reader is referred to the main introduction of this work for an overview of some recent controlled deposition experiments.

We have chosen to study the implantation of silver clusters into an HOPG (Highly Oriented Pyrolytic Graphite) substrate, and to investigate particularly the scaling relations which define implantation. The clusters implant into the HOPG by penetrating successive graphite planes immediately beneath the impact zone. Since the well-diameter is typically smaller than the STM tip, measurements of the implantation depth of the clusters require an oxidation of the sample. Oxidation is then used to obtain much wider etch pits of the same depth as the implanted cluster.

5.2 The process of graphite oxidation

In the following we will give some details about the process of oxidation of natural graphite surfaces. The reader is referred to Sect. 2.2.2 for the characterization of the HOPG sample. We will extend the discussion to the oxidation of artificial defects created by irradiating the HOPG surface with different projectiles.

5.2.1 Experimental results in the literature

In the pioneering work by Hennig, Thomas, Yang and others [74–78], the authors used microscopic techniques for extensive studies of gasification reactions of carbon, especially graphite . At the beginning, the main results achieved by optical microscopy consisted in founding anisotropies of reactivity on different crystallographic faces of the carbon sample and in the identification of active sites. An excellent review on this subject has been published by Thomas [76]. Optical and scanning electron microscopy were subsequently replaced by *etch-decoration electron microscopy*, which yielded kinetic data on the atomic scale. The technique was developed by Hennig and is described in detail in his fundamental paper [75]. This technique is based on the high anisotropy of reactivity of graphite on different crystallographic faces and on the ability of the crystal edges to trap and nucleate gold. More recently, Etch-decoration Electron Microscopy has been taken over by *Scanning Tunneling Microscopy*, which has proven to be a powerful tool to study gasification reactions of graphite because of its high resolution in both horizontal and vertical dimensions [79].

A difficulty in comparing data from the literature is that the experiments were carried out under different conditions (different samples, temperatures, gas flows, pressures..). This study shall concentrate on the **gasification of carbon samples in molecular oxygen**. For the reactions of carbon with some other gases the reader is referred to the reviews [75, 78].
The mechanism of the $C - O_2$ reaction is temperature-dependent. At temperatures below 700° C the carbon-oxygen reaction is highly dependent on the nature of the carbon sites on the graphite sample. Oxidation is initiated mainly at single vacancies on the basal plane [74, 77], defects, or edge atoms along cleavage steps, presumably because of their free sp^2 electron [78, 80]. At temperatures above 700° C, oxygen can additionally attack and subtract carbon atoms from the basal plane of graphite and initiate new vacancies. Upon oxidation, these vacancies expand to form monolayer etch pits.

In the following the discussion will be restricted to **carbon-oxygen reactions at temperatures below** 700° C, since 650° C is the oxidation temperature employed during this thesis work.

Instead of the natural graphite crystals used in earlier investigations, *Highly Oriented Pyrolytic Graphite* (HOPG) has become an interesting sample for STM studies of gasification reactions. Chang and Bard [81] treated the HOPG sample at 650° C in air for 15 min, and obtained a majority of pits of circular shape and uniform size, indicating that they were initiated at the same time on naturally occurring point defects on HOPG. Besides the regular pits a certain number of pits and channels with irregular shapes were sometimes observed. This rather broad distribution of pit diameters can be ascribed to initiation and growth at impurities [81] or multivacancies [82] on the HOPG surface. Their different induction time for oxidation with respect to the "regular" pits has been interpreted as the time required to *activate*[1] them.
The majority of the pits was one monolayer deep, as measured from the STM height profile. The existence of monolayer pits confirmed that there is some degree of anisotropy in the mode of carbon removal from the surface, as monolayer pits can only be formed if there is **preferential attack parallel to the basal plane**. At the fixed temperature of 650° C, the diameter of the monolayer pits increased linearly with reaction time (at a rate of 52 Å$\cdot min^{-1}$) [81], a phenomenon which can be understood in terms of a linear increase with time in the number of reactive carbon sites along the steps of a single pit during oxidation. Stevens *et al.* [83] recorded a similar slope ($\sim$ 45 Å$\cdot min^{-1}$) for the linear fit curve of the monolayer pit diameter vs etch time (oxidation again performed at 650° C in air).
The linearity of the "pit diameter vs etch time" curve is consistent with the idea that the reaction rate is not dependent on the pit diameter, and is supported by the occurrence of inner secondary pits which grow tangential to the primary ones (Fig. 5.1). These secondary holes are in fact initiated when the primary pit exposes to air an internal vacancy. The two pits subsequently grow together, hence revealing that the reaction rate is independent of pit size [84].
Comparing monolayer pit growth rates in different HOPG samples, Tracz *et al.* [82] observed a relation between these rates and the pit density. Larger pits were found to be formed at lower pit densities, the phenomenon levelling off at densities above $\sim 10\,\mu m^{-2}$. The same phenomenon has previously been observed for natural graphite samples by Yang and others [77]. For a possible explanation of the origin of this effect see Sect.5.2.2.

[1] The "activation" of the pit can for example consists the removal of the associated adsorbates.

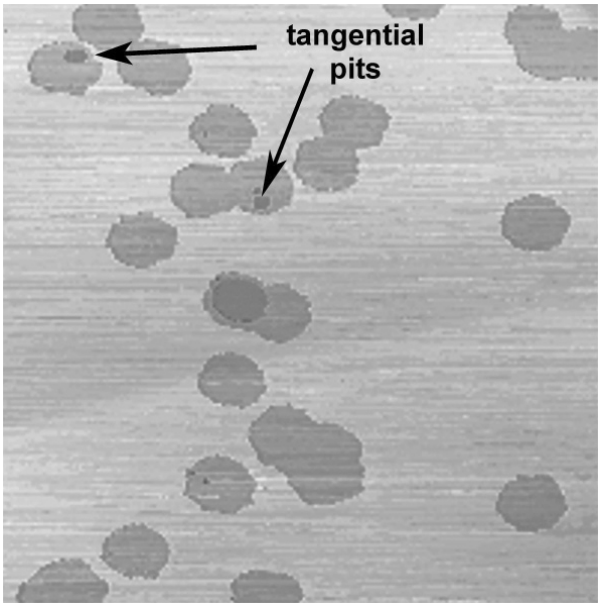

Figure 5.1: An example of secondary pits which grow tangential to primary ones.

Multilayer pits were also sometimes observed by STM, but usually occurring at such low densities that it has been difficult to collect a sufficient amount of data to characterize them [79–81]. The amount of data recently increased thanks to the work of the group of Stevens [83]. They used a lower grade HOPG and were able to image a large number of multilayer etch pits, obtaining better statistics on them. Unfortunately, the origin of these multilayer etch pits remains still unclear. Some of these pits seem to form at screw dislocations (Fig. 5.2), others occur when vacancies on deep layers are exposed to oxygen during the growth of pits on the first layer [81] while others appear at line defects that cut through many graphite layers.

Deep pits with tails and channels have also been observed. These features are probably due to catalytic effects from particles that settled on the HOPG surface before or during the gasification reaction. The random orientation and the different shapes and sizes of the channels support the idea that they represent the paths of randomly moving impurities [80]. For the various effects of different surface particles and their catalytic activities see, for example, the reports [78, 84].

Different reports have disagreed in relation to the **relative etch rates of multilayer edges** as compared to monolayer ones. The *cooperative effect* was first observed by Thomas [76]. It refers to the fact that the reactivity of carbon atoms on the *prismatic planes* of graphite, is substantially higher for a multi-layer edge than for a single-layer one.

Others have also reported that multilayer edges (or pits) grow faster than monolayer

ones by a factor of approximately 3-4 [79, 83] (at $\sim$ 150 $mbar$ of O_2, 650° C). In contradiction with these results, Tracz and others [82] have measured a comparable etch rate of mono- and multi-layer steps (oxidation performed in $\sim$ 200 $mbar$ of O_2, at 670° C). This would indicate that the etch rate of mono- and multi-layer steps is comparable, in contradiction to the "cooperative effect".

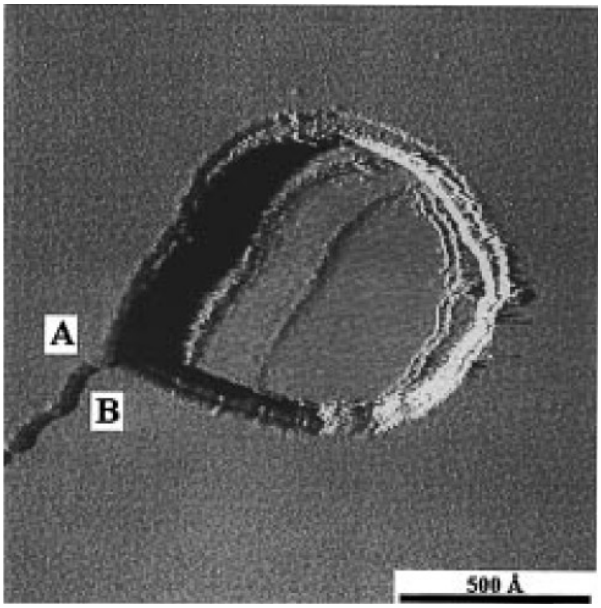

Figure 5.2: A single step radiating from the pit identifies it as having formed at a screw defect. In other words, points A and B are separated by a step in the surface, but by travelling clockwise around the pit it is possible to move from A to B without crossing any step (from ref. [83]).

Trying to obtain a quantitative relationship between the pit depth (or edge thickness) and the reaction rates, we shall start by the basic assumption that the pit etch rate is proportional to the number of edge atoms, i.e. the "active" sites in the oxidation process. Since the number of these edge carbon atoms is directly proportional to the depth of the pit, the etch rate would grow linearly with the pit depth [83].
Most experimental results agree with the idea that the pit etch rate grows linearly with the pit depth. In refs. [83,85], the lateral etch rate is found to be an increasing function of the depth of the initial defect, with deeper pits etching faster than shallower pits **up to a depth of approximately 4 monolayers (ML)**; beyond this depth the etch rate is nearly independent of depth. The observation of this *saturation value* is not yet understood.
Also Hahn and coworkers [86] measured a linear increase of the average growth rate with depth. However, their statistics was only based on 1,2,3,4,ML.

5.2.2 Growth Mechanism and kinetics

The rate data for the C-O_2 reaction have provided the basis for the understanding of the mechanism and kinetics of the carbon gasification reactions. However, numerous open questions still remain.

Regarding the **kinetics of monolayer growth**, different experimental results agree quite well, yielding a linear relation between the radius of voids and the oxidation time. Starting from experimental data and from the general form of the *Arrhenius equation*[2] for rate constants, we can define the following expression for the rate of etching of a single layer in the HOPG basal plane:

$$\frac{dr}{dt}\ (\text{nm/s}) \ = \ k_0^{'}\, e^{-(\frac{E_a}{RT})}\, P_{O_2}\ (\text{mbar}) \tag{5.2}$$

where r is the pit radius, E_a is the activation energy, T is the temperature and P_{O_2} the oxygen pressure during the oxidation process. Eq. 5.2 has been recently [86] extended to also describe the **kinetics of multilayer growth**. The authors measured a value of E_a which is approximately the same for mono and multilayer pits. On the other hand, the $k_0^{'}$ factor increases with the depth of the pit, and this gives rise to the higher etch rate. Unfortunately, only pit depths up to 4 layers were analyzed, and no information about the kinetic parameters of deeper holes were provided.

The **process of pits growth** is quite complicated, and it has only recently been better established.

The "cooperative effect" discussed in the previous section, first suggested that there could be more than one mechanism for the oxidation of edge carbon [74]. Two independent mechanisms were initially proposed for the reaction of oxygen molecules with graphite defects [77]. The first one relates to a *direct interaction* of gas-phase O_2 molecules with reactive carbon sites (Eley-Rideal ER mechanism), the second one involves the *reaction of the edge carbon with the migrated oxygen* that is first chemisorbed on non reactive sites on the surface (Langmuir-Hinshelwood mechanism). Among the two experimental evidences of the importance of surface diffusion [77], the first one has been the discovery that the rate of carbon removal (the *turnover frequency*) depended on the population density of the edge carbon atoms, the rate being higher on low-density

[2]Kinetic rate constants are often expressed in the *Arrhenius form*

$$k^{'} \ = \ k_0^{'}\, e^{-(\frac{E_a}{RT})} \tag{5.1}$$

where $k_0^{'}$ is a pre-exponential factor, and E_a the *activation energy* of the process. This activation energy is experimentally determined from an *Arrhenius plot* of reaction rate *vs* $\frac{1}{T}$.

surfaces. This behavior might show the contribution of "nonactive" sites in the overall gasification rate of active sites. The second evidence of the importance of surface diffusion was related to the continued carbon gasification after O_2 was cut off from the gas flow over the surface, indicating that some oxygen was stored somewhere on the surface. It was uncertain, though, what was the bonding character of the diffusive oxygen species on the surface. The mechanistic details for the oxidation of graphite were not well understood until recently, when defects were induced in the HOPG sample by irradiating it with energetic projectiles. The higher and controllable defect density allowed to better identify the nature of graphite defects, and to develop an appropriate molecular model for the reaction of oxygen molecules with defects.

5.2.3 Artificial defects created by ion bombardment

Artificial control of the surface density and the size of the pits is necessary for applicational purposes of nano-sized pits. A control of the pits density has been attempted by irradiating the sample with high-energy projectiles, such as electrons, neutrons, ions or clusters. The vacancy concentration increases in direct proportion to the irradiation time; these artificial defect sites can then be developed to holes by controlled oxidation. In particular, it has been shown [84] that 800-keV electrons produce predominantly single vacancies, while accelerated heavy particles favor the formation of multiple or clustered vacancies.

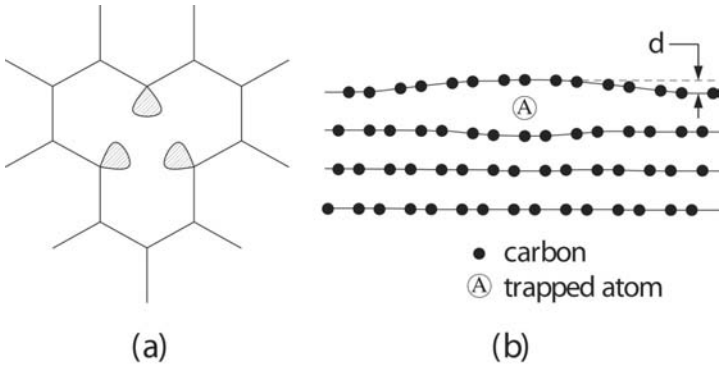

Figure 5.3: (a) A vacancy defect; (b) An interstitial defect originated by an atom which is trapped between the first and the second HOPG layers. Adapted from ref. [87].

Different studies, performed by Kang and coworkers [88–91], about the implantation of rare gas ions on graphite followed by etching reaction in oxygen, have identified the nature of the defects as *carbon vacancies*, created by permanent displacement of surface carbon atoms, and *interstitial defects*, created by trapping of incident atoms

between HOPG layers (Fig. 5.3). Both *vacancy defects* (VD) and interstitial defects (ID) are etched to pits, but their etching efficiencies are different [23]. In particular, in the case of Ar^+ and Kr^+ impinging on HOPG with an energy less than 200 eV, more than 90% of VDs is converted into pits, while less than 15% of IDs undergo the oxidation reaction. In general, they have shown that at all energies there is only a portion of the ID which is transformed into pits, while the rest of the ID defects vanishes without undergoing oxidative etching during the heating period [91]. This is possibly due to the evaporation of trapped atoms (through nearby VD holes) before the initiation of the oxidation reaction, if the oxidation temperature is higher than the desorption temperature of trapped atoms. Similar results were found by Reimann [28], in the case of impact of Ta_1^+ ions on HOPG. They found that such an ion may channel past the first monolayer without damaging it, in which case no etch pit would be nucleated. Furthermore, even if the first monolayer is damaged, if the second one remains intact, only a 1-ML-deep etch pit would be nucleated upon baking, even if the incident ion penetrates more deeply and causes considerable damage below the second ML. Moreover, TRIM calculations [92] predict that the projected range of $550\,eV$ Ta_1^+ equals $6.9\,ML$, strengthening the idea that the etchable damage for incident atomic ions tends to be much shallower than the range of the ions.

A **mechanistic study for the oxidative etching** of Ar^+-induced defects on graphite has been recently reported by Hahn and coworkers [86,90]. The defects were intentionally generated on the HOPG surface with controlled depth and density, and the oxidation behavior has been examined as a function of the defect depth.

The etching mechanism of vacancy defects has been explained [86, 90] in terms of initial dissociative chemisorption of O_2 at the carbon dangling bonds of a VD, followed by activated desorption of CO or CO_2 gas to remove the carbon atoms. In particular, when an O_2 molecule approaches the dangling bonds at a **monovacancy**, charges are transferred from carbon atoms to the oxygen molecule, due to the larger electronegativity of oxygen atoms. This interaction keeps the oxygen atoms apart exothermally, without an activation barrier (Fig. 5.4(a)). When an O_2 molecule approaches to the middle of two dangling bonds at a **divacancy**, three different configurations can occur. If the O_2 molecular axis is parallel to the atomic plane, oxygen can exothermally dissociates and chemisorbs at two top sites (Fig. 5.4(b)), or it can adsorb at the center of the divacancy parallel to the missing carbon dimer (Fig. 5.4(c)). If, on the other hand, the O_2 molecule approaches the bridge site with its own axis perpendicular to the carbon plane, it is molecularly adsorbed at the bridge site in the form of an O_2^* molecular precursor state (Fig. 5.4(d)). Because of the small O-O bond energy, the top oxygen atom can be easily

desorbed at typical etching temperatures, it can migrate on the surface and adsorb on the top and bridge sites at vacancies or react with existing oxides.

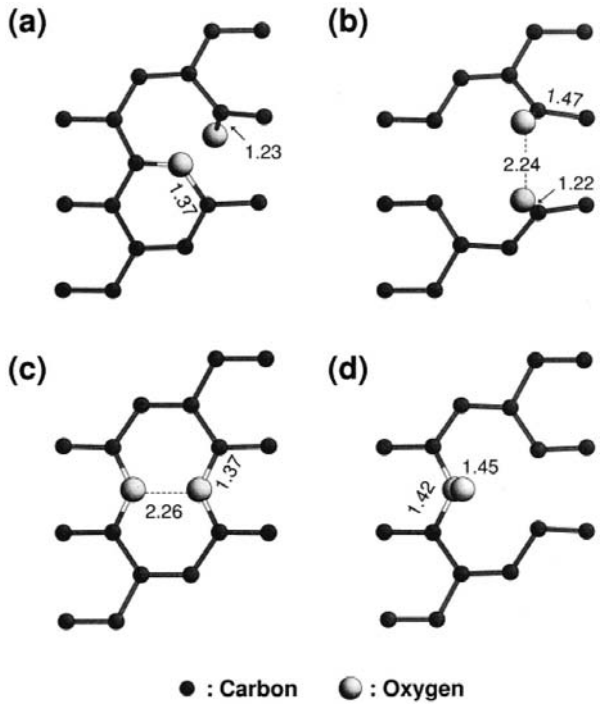

Figure 5.4: Mechanism of O_2 adsorption at vacancies on single graphite layer (from Ref. [86]). (a) O_2 dissociative adsorption at a monovacancy; (b) dissociative adsorption at two top sites of divacancy; (c) dissociative adsorption at two bridge sites of divacancy; (d) O_2 molecularly adsorbed at a single bridge site. Bond lengths are in units of angstroms.

As regards the desorption processes to produce CO and CO_2 gases, the results of Hahn and coworkers [86, 90] are summarized in Fig. 5.5. Since the C-O bond is more stable at the bridge site than at the top site, C-O at the top site is more liable to be etched away to form CO gas at typical etching temperatures. During this reaction, the free-energy is increased but still lower than the initial state, suggesting that exothermal dissociation of O_2 molecules and activated CO desorption from the top sites is the primary etching process, following the ER mechanism. On the other hand, CO_2 can be only formed by a secondary etching process involving energetic CO gas. This explains why the CO production rate is larger than the CO_2 production rate under normal oxidative HOPG etching conditions.

The multilayer reaction can simply be interpreted in terms of the above explained monolayer etching mechanism. There are anyway some differences which lead to the increased efficiency of multilayer etching. The O_2 chemisorption at the multilayer vacancy can produce the oxides or O_2^* species in the sublayer, which, at elevated temperature, lib-

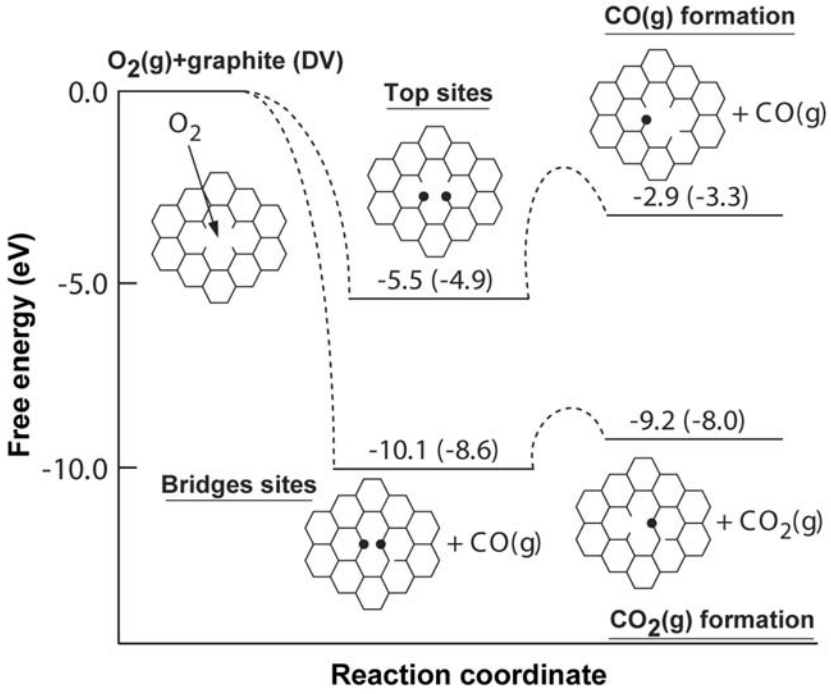

Figure 5.5: Mechanism of O_2 adsorption at divacancies and desorption processes. The top site oxygen is desorbed as CO. CO_2 is formed by reaction of CO gas with the bridge site oxygen. From Ref. [90]

erates gaseous CO or O atoms. The reactive species created in the inner carbon layers will have a higher probability of reacting with oxide species at the upper layer of the etch boundary. These secondary reactions allow to remove the oxides not only from the top sites but also from the more stable bridge sites by forming CO_2.

This mechanistic interpretation explains the increased efficiency for multilayer etching, and is consistent with the kinetic parameters obtained by the STM study. The higher k_0' factor (see Eq. 5.2) for multilayer etching is consistent with the higher collision rate of the reactant, and the similar E_a values are actually related to similar energies for the transition states.

The etching of an **interstitial defect**, on the other hand, is initiated by oxidation of a graphite surface deformed by an interstitial Ar atom trapped underneath. The increase of reactivity at the deformed surface results from a charge density increase in this region [87]. Once initial O_2 attack creates a defect hole at the carbon plane, then the rest of ID etching processes should be identical to VD etching. For oxidation of multilayer defects, the top and inner carbon layers are simultaneously etched away at the boundaries.

Interstitial *carbon* atoms are also generated by Ar^+ collisions, but they are very mobile at room temperature owing to a low diffusion barrier ($E < 0.1\ eV$) and cannot be the

source of etched pits.

5.3 Experimental procedures

The implantation of mass selected clusters into HOPG involves a certain number of operations, which will be described point by point in Appendix A. The basic experimental procedure is summarized in the following.

The **production** of silver clusters has been performed with the CORDIS-type cluster source, which has been described in Sect. 4.3.1. The silver ions Ag_N^+ are injected into the quadrupole, and mass-selected (in this experiment N=1,3,7,9,13). Mass-selected clusters are projected at normal incidence onto the graphite surface, which has been prepared by cleaving with Scotch tape immediately prior to insertion into vacuum. The clusters impact energy is controlled by the voltage on the sample, and coverage is determined by the beam current density and the deposition time. Typical values of the beam current and of the deposition time are $\simeq 10\,pA$ and $\simeq 5\,s$ respectively, which yield a mean coverage of the order of 100 impacts/μm^2.

The **thermal oxidation** of the cluster-bombarded graphite is carried out in a furnace oven (Sect. 4.4.1), which is evacuated to a pressure of $\simeq 10^{-5}\ mbar$ and heated to a temperature of 650° C. A first cleaning of the sample is performed, and oxidative etching is then achieved by heating the sample at 650° C for approximately 25 minutes in a controlled atmosphere of oxygen (the partial oxygen pressure is $\simeq 100\ mbar$).

Different etch times, temperatures and oxygen pressures control the pit growth rates and the activation energies [83]. In particular, the average diameter of the etched pits at a fixed temperature and oxygen pressure, increases linearly with reaction time [80].

We have used a homemade STM (Sect. 4.4.2) to **investigate the surface**. The microscope works in the "constant current mode", at ambient conditions of temperature and pressure. Images are taken at typical currents of the order of $1-2\,nA$ and bias voltages of approximately $1-2\,V$ (the sample is positively biased with respect to the tip).

5.4 Results

5.4.1 Oxidative etching of pure HOPG

The results of the oxidation of the pure graphite substrate in a controlled atmosphere of approximately $100\,mbar$ of oxygen, at 650°, is studied by *scanning tunneling microscopy*. Fig. 5.6 is a representative STM image showing etch pits of uniform size and monolayer

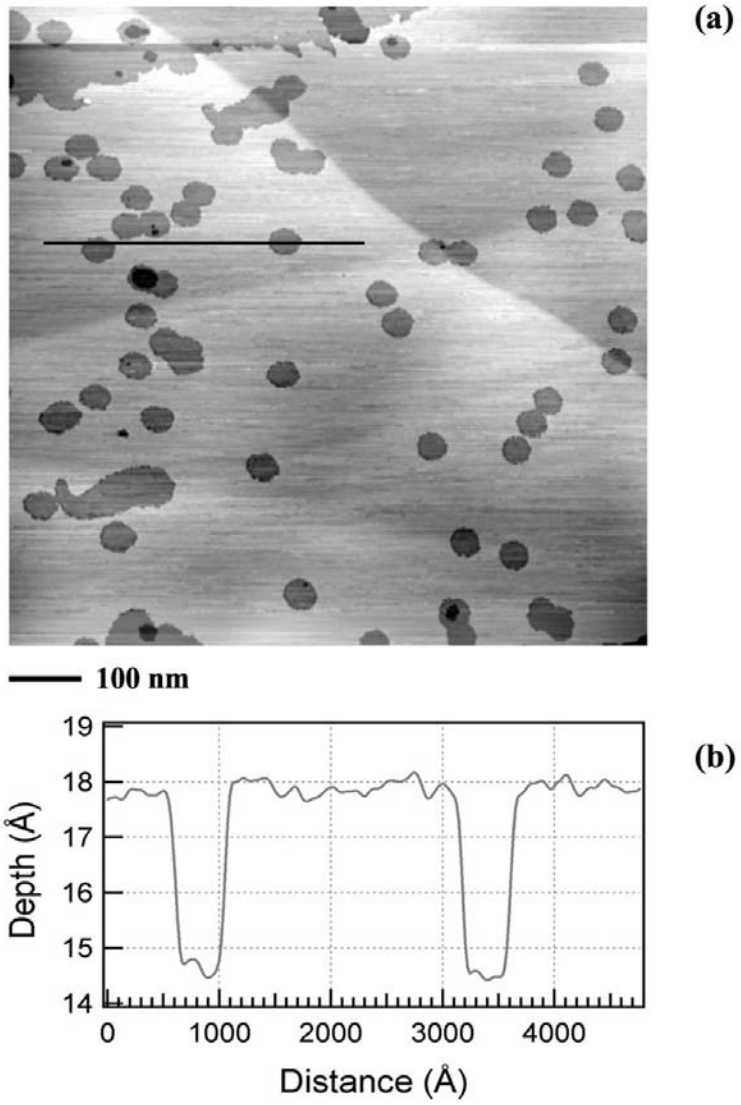

Figure 5.6: (a) Etch pits generated on a pure HOPG sample heated at 650° in a 100 $mbar$ atmosphere of oxygen for 40 min; (b) Line scan on two different 1ML pits.

depth formed on preexisting defects in the HOPG basal plane. The density of pits in different samples varies from 80 to 100 μm^{-2}. Most of the defects are 1ML in height, circular in shape, and their average diameter ranges about $40 - 50\, nm$. These naturally occurring defects on the graphite surface form a background of monolayer pits which has to be subtracted from the defects formed by cluster bombardment.

In a few cases, new etch pits are formed at the center of other pits, meaning that defects in the second layer were exposed to oxygen during the expansion of etch pits in the first layer (see Sect. 5.2.1). Inner smaller pits which grow tangential to primary bigger ones are occasionally observed, supporting the idea that the etch rate is independent of the pit diameter. A few channels and pits of irregular shape are also present on the surface.

Fig. 5.7 shows the result of performing the sample oxidation in a polluted atmosphere. Impurities adsorbed on the HOPG surface are highly reactive to oxygen, and randomly oriented channels observed on the surface could be due to the diffusion of these molecules on the surface. Multilayer pits with tails and various structures of irregular shape may also be due to the catalytic effects of impurities that settled on the HOPG surface.
Such a sample cannot be used as substrate for implantation experiments, because of the impossibility of precisely determining the background of holes due to the oxidation of the graphite sample previous to implantation.

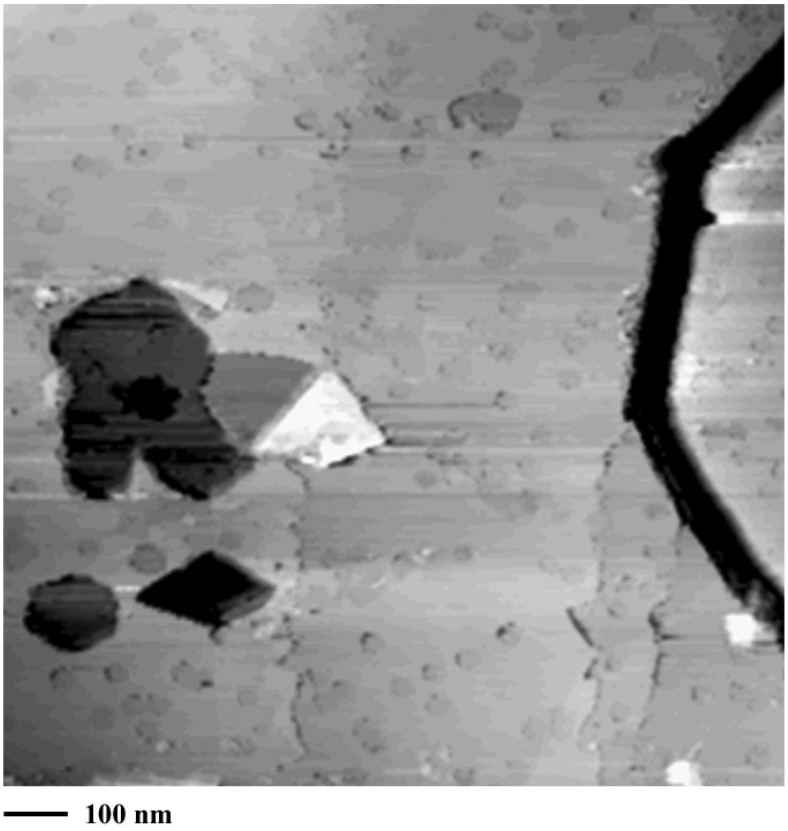

Figure 5.7: Etch pits of various depths generated on a pure HOPG sample heated at 650° in a 100 $mbar$ (polluted) atmosphere of oxygen for 40 min. The large distribution of pit depths might be caused by impurities adsorbed on the sample surface.

5.4.2 Implantation of Ar ions into HOPG

In preliminary measurements, Ar^+ ions have been implanted into a clean HOPG sample, in order to make practice with the parameters of implantation and oxidation. Fig. 5.8 shows an example of the HOPG sample irradiated with 400 eV Ar ions and subsequently oxidized. The bombarded sample has been oxidized at 650° C for

45 minutes, in 100 mbar of oxygen. Pit depths up to 4 layers were measured. This result is in good agreement with the results obtained by Kang and coworkers [86,90,91]. They verified that with Ar^+ ions of energy smaller than 500 eV no pits are formed deeper than four layers. Anyway, due to the small size of the rare gas ions, the etchable damage tends to be much shallower than the range of the ions. The Ar^+ ions in fact can penetrate deeper than the measured 4 ML depth, forming interstitial defects of which only a small portion develops to holes during oxidation (for more details see Sect. 5.2.3).

5.4.3 Implantation of silver clusters into HOPG

Before oxidation

Fig. 5.9 is a typical example of the graphite substrate **after implantation** of Ag_7^+ clusters at a deposition energy of $2\,keV$. As such hillocks have never been observed on the pure HOPG surface, they constitute a mark of the presence of clusters on the substrate. Due to the small size of the protrusions, STM measurements *before* oxidation require a much higher impacts density than the usual one for the analysis of oxidized surfaces. In Fig. 5.9 the coverage is approximately 20000 impacts / μm^2.
The mean hillocks diameter measures $\approx 20 - 30$ Å and their mean height is approximately $3-4$ Å. The size of the protrusions is the same as the one measured by the group of Palmer [24] for the implantation of Ag_N^+ (N=1,3,5,7) clusters on graphite, at similar impact energies. Protrusions of similar size are also observed in the case of different ions impacting on graphite [93,94].
The actual mechanism for the formation of bumps on graphite is not yet fully understood. The hillock structures produced from high-energy ion collisions, typically a few nm in diameter or larger, were interpreted as representing the actual geometry of damaged spots, i.e. local erosion of carbon layers. Energetic ions generate complex collisional cascades in the solid and the resulting damage extends over a wide region (see Sect. 2.1.1). Several explanations were proposed for the formation of hillocks, including *thermal spikes*, *defect-induced stress*, and *electronic excitation*.
On the other hand, ion-surface collisional events can be greatly simplified if the impact energy is below 100 eV (we cite the low-energy case for sake of completeness, but we will not enter into details, as the energies of interest for this study range from 1 to 30 keV). Hahn and coworkers [89] verified that the protrusions originated by low energy Ar^+-impacted graphite actually arise from the electronic structure of the atomic defects. The bright spots appearing in the STM image originated from an increased partial charge

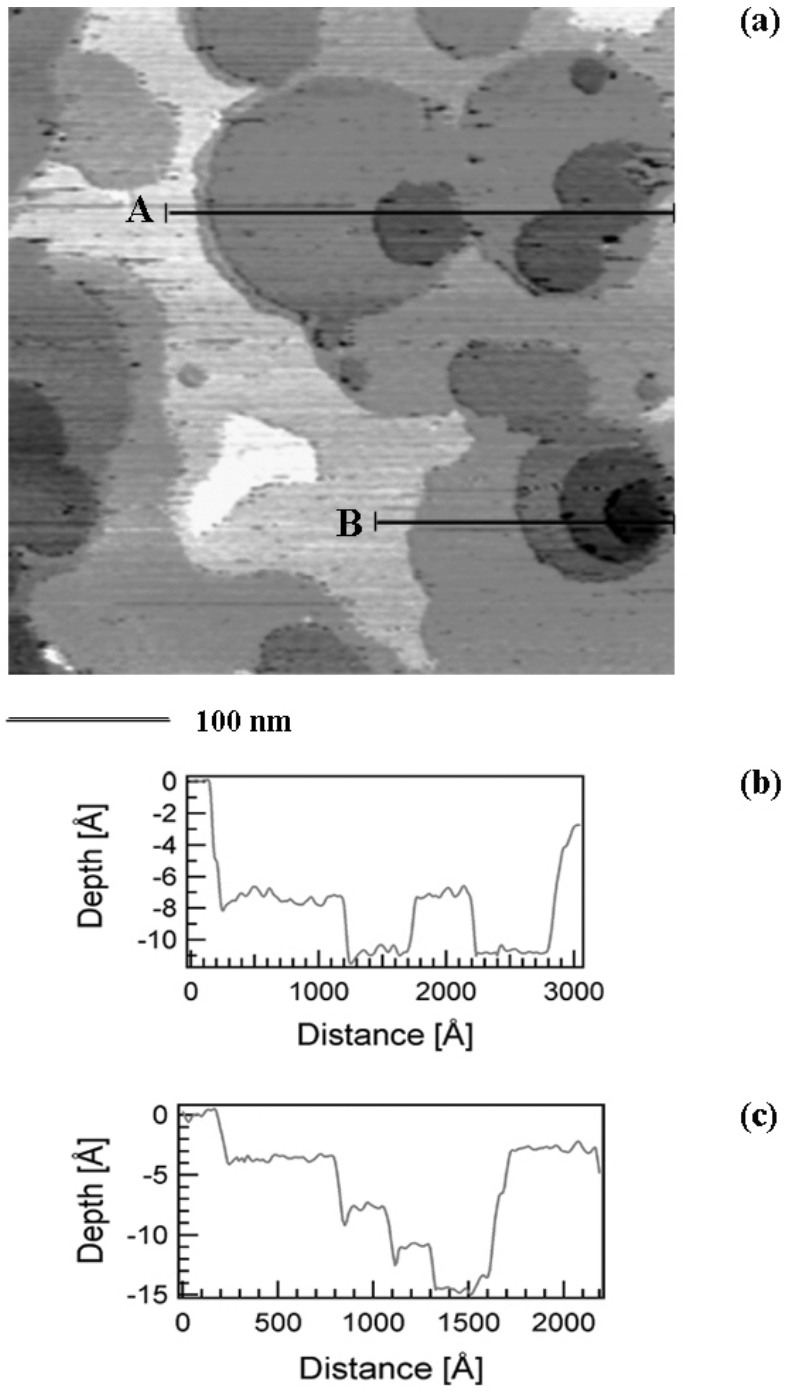

Figure 5.8: (a) STM image of the HOPG sample bombarded with 400 eV Ar^+ ions and oxidized; (b) profile of line A; (c) profile of line B: 1, 2, 3, 4 ML pits can be recognized.

density near the Fermi level (E_F), although the actual topography at a vacancy site is almost flat, as shown in the respective AFM image. These experimental results well agree with electronic structure calculations for graphite atomic vacancies [95], which predict that the charge density of states (CDOS) is increased in the carbon atoms surrounding an atomic vacancy both in their filled and empty states near E_F. As the STM image of a surface is described by the partial CDOS plot near E_F, the STM can efficiently monitor the CDOS change in the neighboring carbons introduced by the vacancy.

More recently [87] these results were extended to *interstitial defects*, which also in-

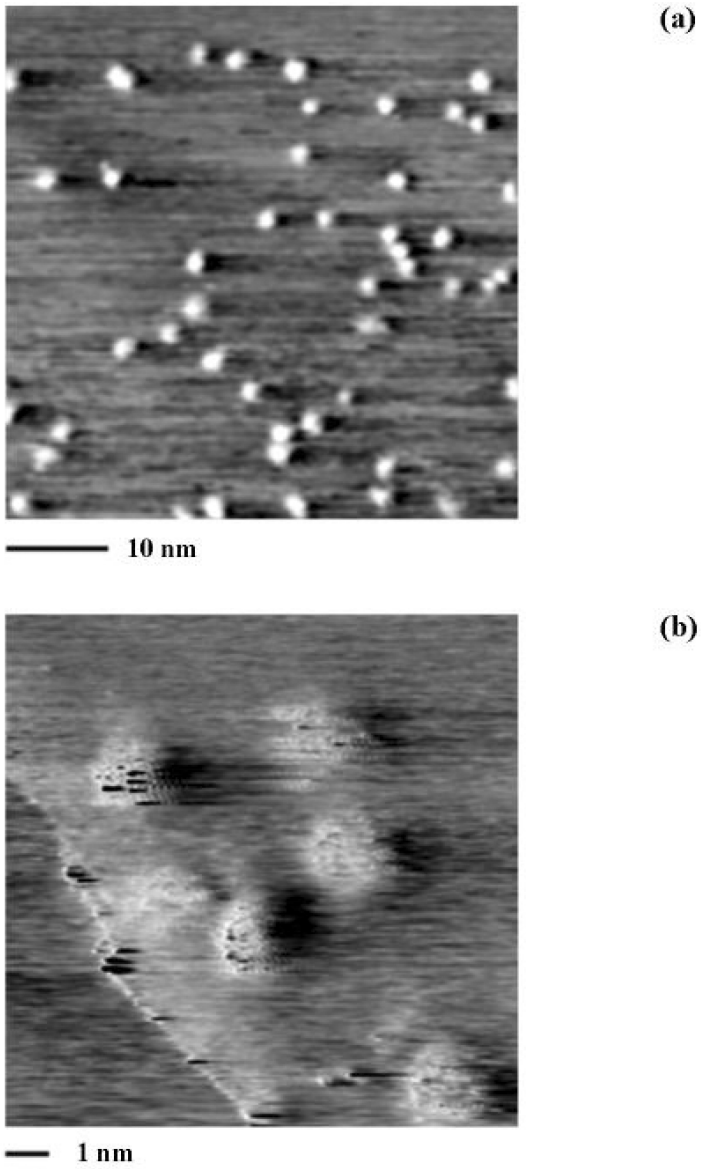

Figure 5.9: (a) STM images of hillock defects on bombarded and still not oxidized HOPG surface; (b) zoom on implanted clusters.

creases the local charge density of states near the Fermi energy, even if the effect is larger for a VD due to its dangling bonds. We will not enter into details, as during this thesis work we employed higher impact energies.

After oxidation

After oxidation of the samples, the hillocks are no longer visible, they are replaced by etch pits of various depths and diameters.
Fig. 5.10 shows examples of the oxidized graphite surface after implantation of Ag_N^+ clusters of different sizes (N=1,3,7,9,13) and different impact energies (ranging from 1 to 30 keV). The HOPG substrates were tested by oxidizing previous to implantation. The chosen ones proved to be of good quality, with an almost constant 1ML defect density (approximately $80\,\mu m^{-2}$) and very few and distinguishable multilayer pits.
All the images have been systematically analyzed by measuring the depth and the diameter of the etch pits. Each image contains two distributions: the first one due to clusters impacts on the surface, and the second one related to the one-monolayer natural defects. The etch pits associated to the naturally occurring defects are smaller and shallower (except for a family of highly irregularly shaped pits, which have been ignored in the pit counts) than the pits originated from clusters impacts.

We have first performed a **systematic study of the pits diameters**. In particular, for each cluster size we have chosen to analyze the experiment performed at a cluster impact energy of 3-4 keV, at which the distribution of pit depths ranges from 1 to approximately 8-10 monolayers (to have an idea of the pit depth distribution at these impact energies, see the histograms in Fig. 5.12). The diameters of the pits of equal depth are measured, and an average value is calculated. These mean diameter values together with their standard deviation are plotted in Fig. 5.11 as a function of the pit depths, for each cluster size at the specified impact energy. An increasing linear behavior is evident for each cluster size, up to a pit depth of approximately 5 ML. In Table 5.1, the parameters of the linear fits (3^{rd} and 4^{st} columns) and of the saturation value (5^{st} column) of the curves in Fig. 5.11 are summarized for each cluster size.
The plots contained in Fig. 5.11 yield information about the **kinetics of the graphite oxidation**, which is strictly dependent on all oxidation parameters, namely the *oxygen partial pressure*, the *temperature* and the *duration time* of the oxidation. Unfortunately, all these parameters could only be manually controlled during experiments, thus not being defined with precision. Moreover, there are delays in the sample heating, which change from one experiment to another. The real oxidation time is thus not known

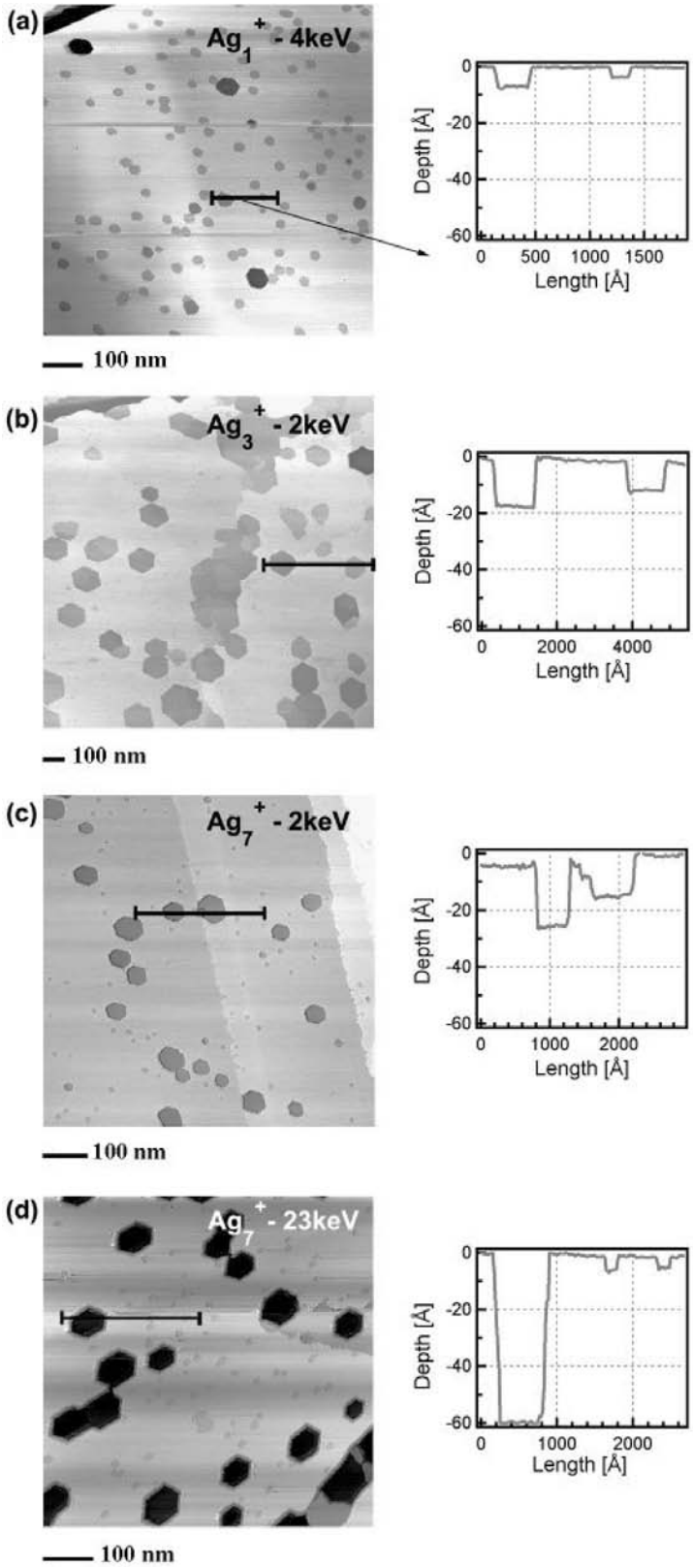

Figure 5.10: Different examples of oxidized graphite surfaces, after the impact of Ag_N clusters at various kinetic energies.

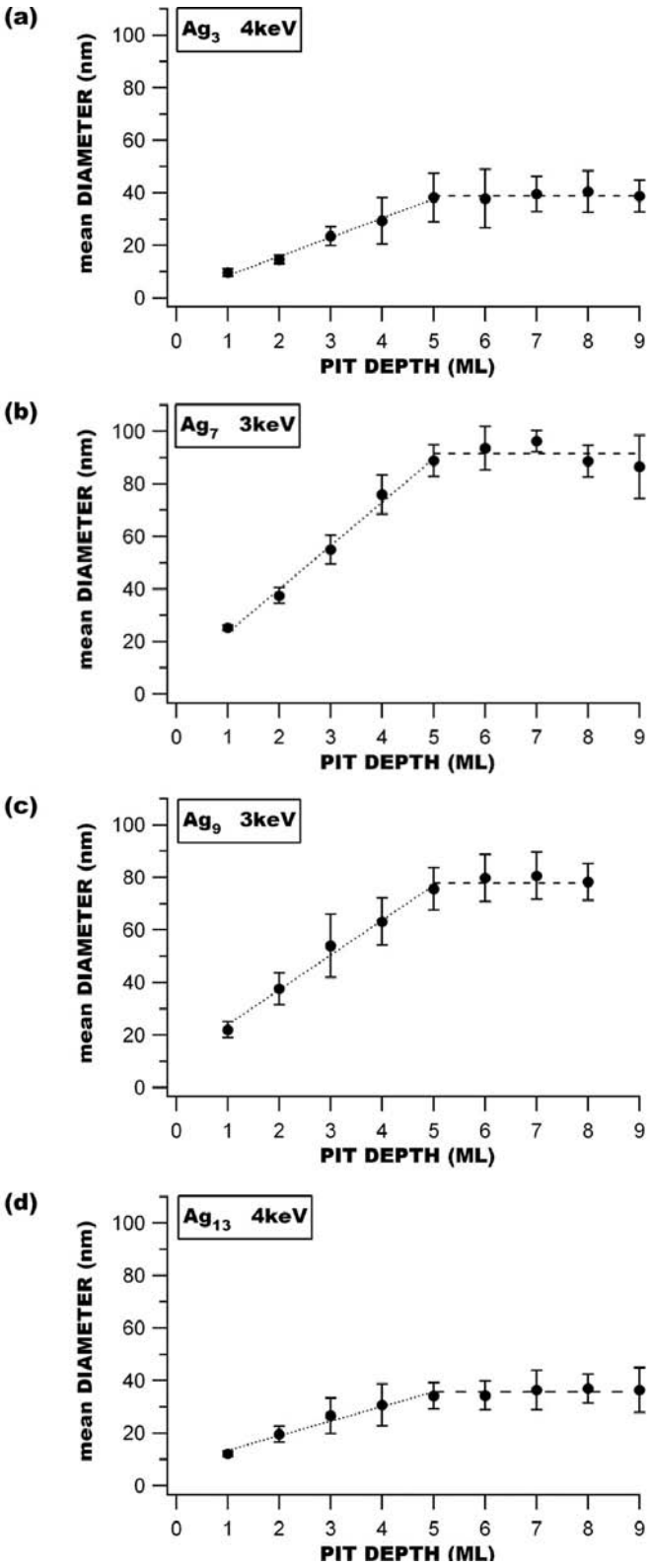

Figure 5.11: Mean pits diameter as a function of the pits depth, for each cluster size. Errors correspond to standard deviations values. For all sizes an increasing linear behavior is distinguishable up to a pit depth of approximately 5 ML.

with great precision. Finally, some variations in the oxygen pressure or in the oven temperature could have occurred during oxidation.
The difficulty in comparing results from the different experiments is then related to the fact that they were carried out under different conditions. In particular we remark that in Fig. 5.11(a) and in Fig. 5.11(d) the diameter of monolayer pits corresponds to half the value in Figs. 5.11(b) and (c). This suggests that the effective oxidation time and temperature are larger for samples (b) and (c) than for samples (a) and (d). The important conclusion to draw from Fig. 5.11 is that for all samples there is a saturation value of the mean diameter for pit depths of approximately 5 ML. This result is in accordance with other results reported in the literature [83, 85, 86] (see Sect. 5.2.1).

Cl.Size	Ox.Time(min)	Y-Intercept(nm)	Slope(nm/ML)	Saturation(nm)
3	30	1.20±1.29	7.30±0.39	38.85±0.21
7	27	6.80±2.70	16.56±0.82	91.60±1.78
9	25	10.65±2.62	13.27±0.79	77.83±1.81
13	18	8.00±1.79	5.54±0.54	35.66±0.59

Table 5.1: Fit Parameters of the mean diameter as a function of pit depth for different cluster sizes.

We have also made a **systematic study of the implantation depths** of the Ag_N^+ clusters into the HOPG substrate.
To obtain significant statistics, at least 80 pits have been measured for each cluster size at a specific kinetic energy. Some of the results are shown in fig. 5.12. Almost all the depth distributions have a gaussian form once the background of monolayer pits coming from the natural graphite defects has been subtracted. Only the **depth-distribution associated to the implantation of monomers presents some differences**, as it does not take a gaussian form and the main peak corresponds to a pit depth which is shallower than the expected one. The reason is that, in the case of monomers, the distribution of etch pit depths doesn't reflect the implantation depth of the ions, as explained in Sect. 5.2.3. This is related to the fact that the monomer, due to its small size, can be trapped in-between graphite layers, forming *interstitial defects*. Only a small portion of interstitial defects develops to holes during the process of oxidation. As in the case of the monomer implantation the proportion of interstitial defects can be important, the real penetration depth of the monomer ion is much higher than the peak of the measured pit-depths distribution. It is then reasonable to assume that the "real" mean implantation depth corresponds to the upper edge of the experimental pit-depths distribution.

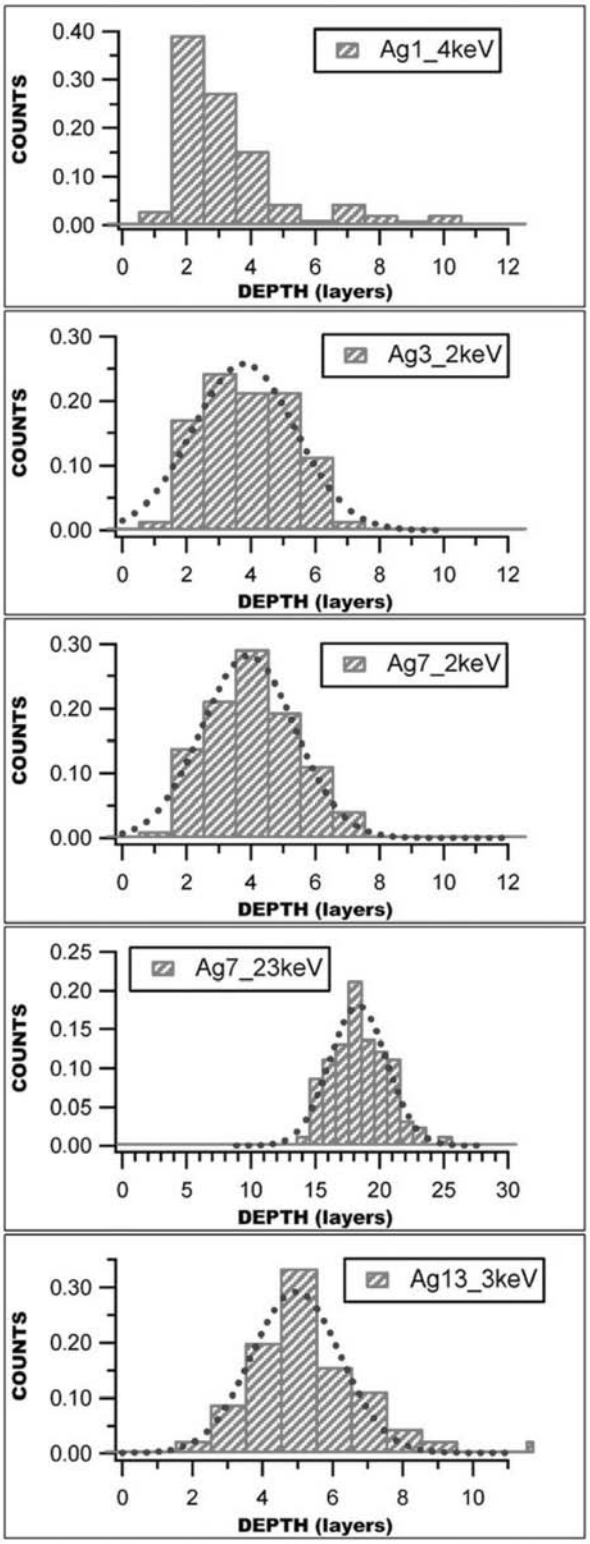

Figure 5.12: Histograms of etch pit depths after implantation of Ag_N clusters at various kinetic energies, as measured by STM.

By fitting the measured histograms with gaussian distributions, we have determined the *mean implantation depth* for each cluster size at each incoming energy. In the case of the monomer, as explained above, the mean implantation depth is taken to correspond to the small peak appearing in the upper part of the distribution.
Fig. 5.13 contains the plots of the *mean implantation depth* (for each cluster size) as a function of the cluster incoming energy. If we consider the low energy range (Fig. 5.13(b)), the different curves are not easily distinguishable. But when considering the whole energy range for Ag_7 and Ag_{13}, a "square-root" behavior of the mean depth as a function of energy can be recognized and possibly extended to the other sizes (Fig. 5.13(a)). In the following sections, starting from this observed relation between the *mean implantation depth* and the cluster kinetic energy, the appropriate scaling relations connecting the depth to other dynamical parameters of the incident cluster will be explored.

5.5 Discussion of the results

5.5.1 Mean implantation depth or upper edge of the height distribution?

To complement their experimental measurements of the implantation depth of silver clusters in graphite, Kenny *et al.* have modelled the cluster implantation process via molecular dynamics simulation [14]. They remarked that the implantation depth found in the simulations lies almost exactly at the upper edge of the experimental distribution for Ag_7^- implantation at 5 keV. Other experiments and calculations for Ta_{1-9} [28, 96] and C_{60} [97] clusters indicated also that the MD implantation depths were larger than the peak depths derived experimentally from the oxidative etching technique. To explain these results, it was first suggested [14] that there can be cluster energy loss channels operating in the experiment, which are not included in the simulations. Another possibility is that the high temperature of the etching process partly anneals the defects created by the implanting cluster, i.e. the defects are partially healed before oxidation takes hold [14]. In particular, they experimentally verified that etching at different temperatures gives rise to different pit depths distributions. In particular, etching at 450° C, compared with 650° C, has resulted in an overall increase of approximately 1 ML in the depth distribution, whereas pre-annealing at 850° C leads to a major decrease in depth of $\sim 5-6$ ML. These results hint at the possibility that the temperatures used during oxidation heal the damage formed by the implanted

clusters, such a process reducing the depth of many etch pits and giving rise to the shallower experimental distributions with respect to the MD simulations.
As there is not yet clear evidence that the "real" cluster penetration depth corresponds to the upper edge of the experimental distribution, we decided to use the peak of the distributions to find a relationship between the implantation depth and different impact kinetic parameters. In any case, we are interested in *general* trends and we expect these trends not to change consistently if considering the peak or the upper edge of the distributions.
Our choice is also supported by the fact that in the case of Ag_7^+ our results of the *mean implantation depth* as a function of cluster kinetic energy, are in a remarkably good accordance with Palmer's group curve of the *upper edge implantation depth vs* energy. This discrepancy may be due to the fact that we used longer etch times (25-30 min) than the Palmer's group ones (approximately 3 min), and different oxygen pressures with respect to the pressures they used.

5.5.2 Scaling relations

As cited in the introduction, recent results on the impact of Ag_7, Au_7 and Si_7 clusters on graphite indicate an implantation depth which scales with the *momentum* of the clusters, suggesting an universal scaling behavior of the implantation depth for small clusters of different species.
The linear relationship between the implantation depth and the cluster momentum is consistent with a retarding force proportional to the cluster velocity [27].
Interesting results come also from the study of fullerene cluster ion induced damage on HOPG, for impact energies ranging from 0.5 to 23 keV [98]. The authors fit their measured implantation depth with both a linear function of the incident velocity and the incident energy, and find a better description of the data in the first case [99].
Looking for a refined investigation of these recently proposed scaling relations, we made a systematic study on different silver cluster sizes (N=1,3,7,9,13) impacting on HOPG over an extended energy range (from 1 to 30 keV).
The observed "square-root" behavior of the mean implantation depth vs energy (see Fig. 5.13), implies that the mean implantation depth varies linearly with the cluster momentum. Our results are presented for all cluster sizes and over the full energy range in Fig. 5.14(a). As expected, a linear fit of the mean depth as a function of momentum describes well our data. However the slopes depend on cluster size.

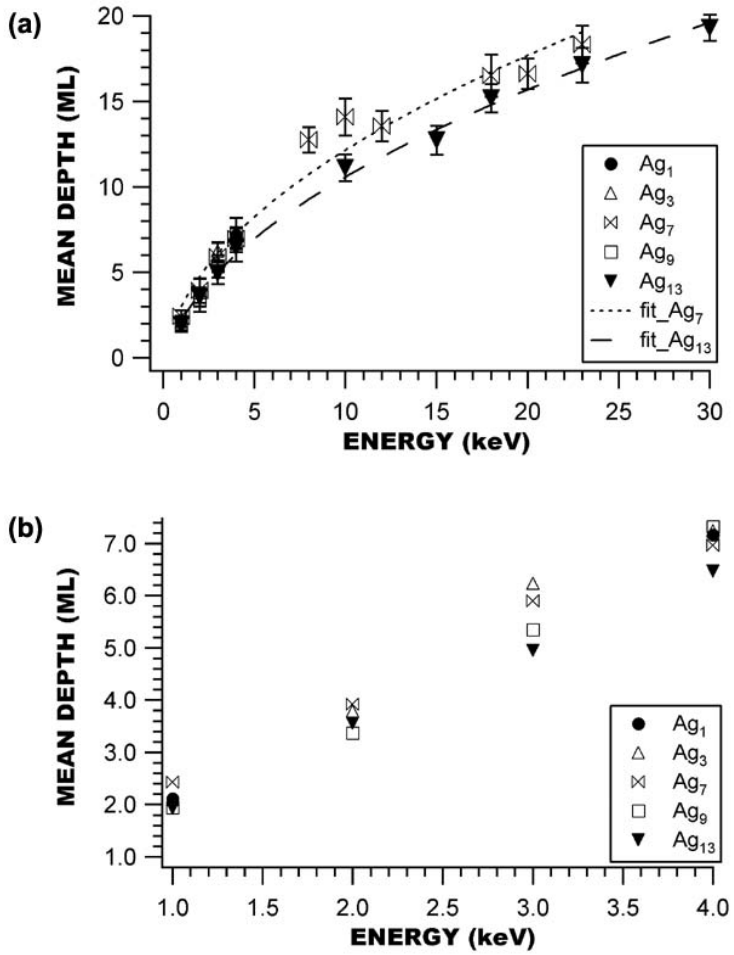

Figure 5.13: Mean penetration depth as a function of the cluster incoming energy, for each cluster size. Filled and open marks are used to better distinguish the different curves. In the following, our results will be characterized by filled marks. (a) The square-root fits of the Ag_7^+ and the Ag_{13}^+ curves are shown. Error bars have been added to the data points. (b) Zoom on the low-energy part of (a). Error bars have been suppressed for more clarity.

Trying to find a sort of "universal" behavior consisting in straight lines of the same slope for each cluster size, we have divided the momentum of the incoming cluster with the cluster projected surface. This momentum scaling was motivated by the fact that when we consider the outcome of cluster deposition, it is not only the energy or the momentum of the cluster which are important, but also the *local area* of the substrate with which the cluster interacts. We expect that the *retarding force* increases for increasing cluster size, and then that the implantation depth decreases.

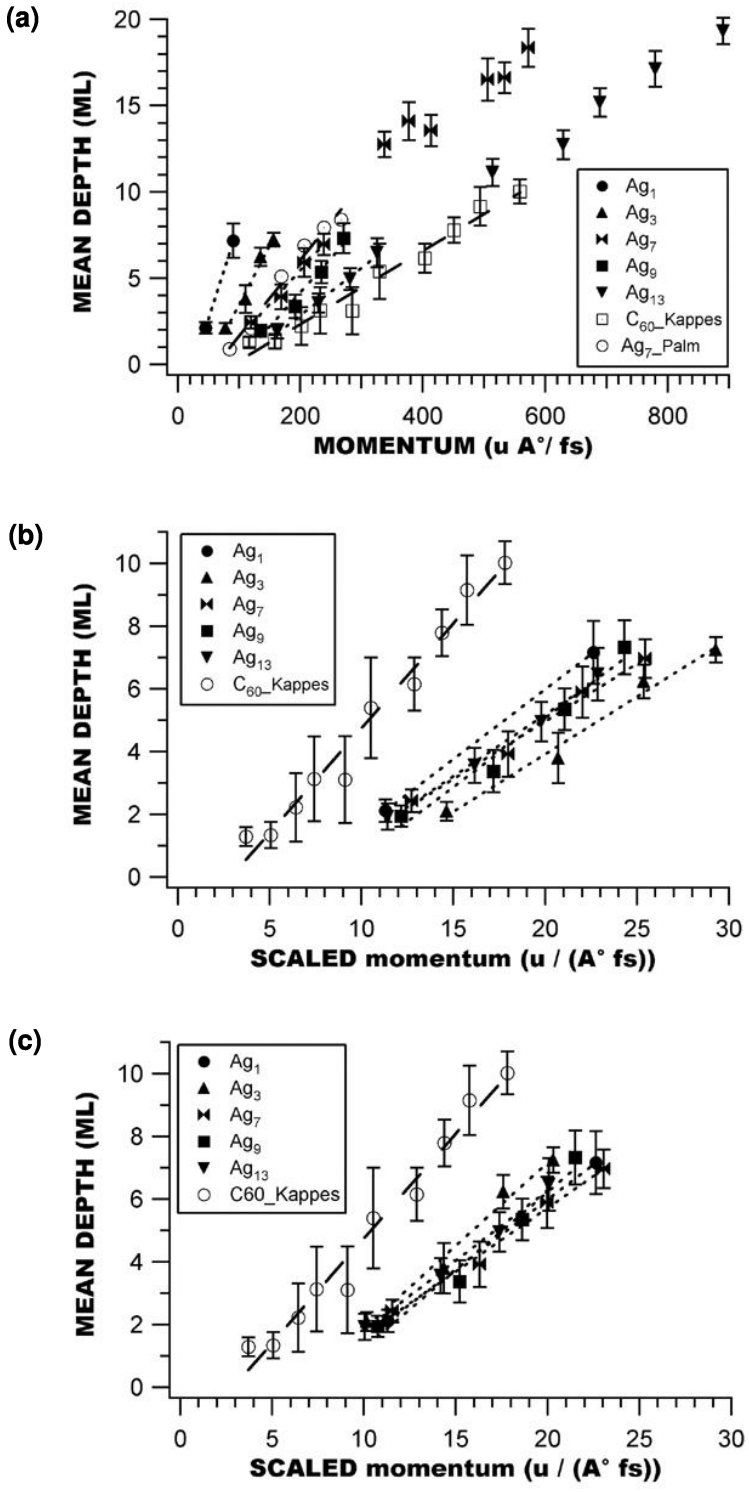

Figure 5.14: Results on C_{60}^{+} [98] are added for comparison (open marks).(a) Mean penetration depth vs momentum, for the different cluster sizes over the full energy range (filled marks). Results on Ag_7^{+} [27] by the Palmer's group are also added for comparison (open marks). In this case, the plotted implantation depth corresponds to the upper edge of their experimental distribution. (b) The momentum is scaled with the cluster projected surface, in the approximation of *spherical particles*. (c) The momentum is scaled with the projected surface calculated from the *real cluster geometry*.

Scaled momentum in the approximation of spherical particles

We started by approximating clusters with spheres. The cluster volume is filled by N-atoms, which are treated like spheres. The atomic radius is the "Wigner Seitz radius", defined by the equation:

$$V = N\frac{4}{3}\pi r_{ws}^3 \quad \Rightarrow \quad r_{ws} = \sqrt[3]{\frac{3M_{at}}{4\pi\rho_0}} \tag{5.3}$$

in which ρ_0 is the density of the bulk, and M_{at} the mass of an atom. For silver, r_{ws} is approximately 1.6 Å. In this approximation the cross-sectional area is equal to $\pi N^{\frac{2}{3}} r_{ws}^2$. In the case of the monomer ion, we consider that it is neutralized before the impact on the graphite surface (see Sect. 6.2.1 for major details on the neutralization process). It is then treated like a neutral atom.
Dividing the momentum of the N-atoms cluster by $\pi\, N^{\frac{2}{3}} r_{ws}^2$, we obtain a momentum scaled by the cluster projected surface. In Fig. 5.14(b) the mean implantation depth is plotted as a function of this scaled momentum. The curves are presented only up to an energy of 4 keV, in order to consider the same energy range for all cluster sizes, and to have higher visibility on the different curves. Results on C_{60}^+ [98] are added for comparison.
C_{60}^+ is taken with its own real structure, a sphere of radius 5.6 Å. The C_{60}^+ projected surface is then the section of the sphere.
Observing the graph, we can conclude that this approximation is already quite good. All the curves group together (except for C_{60}^+), and there is a good agreement between the slopes of the different straight lines.

Scaled momentum starting from the calculated geometry of the cluster

Trying to obtain an even better description of the problem, we have calculated the cluster projected surface starting from the geometrical structure of the clusters (Fig. 2.3). The monomer is still treated like a sphere whose radius is the Wigner-Seitz radius.
Except for Ag_1^+ and for Ag_3^+ (whose case will be discussed later), the size of the atoms is considered to be negligible for the calculation of projected surfaces, and atoms are treated like points. Obviously, this approximation is reasonable only for large sizes (cluster projected surface $\gg$ "atom projected surface"). Still in the case of "large" clusters, the projected surface is calculated as the arithmetical mean between the maximal and minimal sections. This approximation improves the higher the symmetry of the clusters, and it takes into account all the possible orientations into which the cluster can hit the surface. In the case of large projectiles we neglect (in first approximation) the

deformation of the cluster when it impacts on the HOPG substrate.
We shall now discuss the case of the trimer ion, which has a planar structure (Fig. 2.3(a)). As the atomic dimensions are of the same order as the triangular surface calculated from the interatomic distances, atoms cannot be considered as points. In a good approximation, we can assume that the atoms are arranged in the plane in order to fill the triangular structure. If at the impact on the HOPG substrate the Ag_3^+ plane and the graphite surface are parallel, the cluster is not deformed and the projected surface is simply equal to three times the "atomic section", πr_{ws}^2. In the case of all the other orientations of the impinging cluster with respect to the graphite plane, we imagine that the rear atom feels the repulsive potential of the other two, the cluster rotates and hits the surface in the same configuration than before. Ag_3^+ "mean" projected surface is then also equal to three times the "atomic section".
Results obtained with this more accurate momentum scaling are shown in Fig. 5.14(c). We observe that all curves group together, and the slope is almost identical to the C_{60}^+ one (the curve associated to C_{60}^+ doesn't change with respect to the previous model, as it is in both cases taken with its own real spherical structure). The good agreement obtained proves that, independently of the considered element and of the cluster geometry, the implantation depth is a linear function of a momentum "per unit surface".
The small discrepancy observed in the case of the C_{60}^+, which does not exactly lie on the same line as the other curves, can be related to its different structure with respect to the silver clusters. The C_{60}^+ geometrical structure is an *empty* sphere: it deforms - during the interaction with the surface - in a different way compared to the *compact* silver clusters. To obtain a better accordance between all the results, we should then consider a smaller C_{60}^+ projected surface with respect to the section of the sphere.

5.5.3 Stopping power

Fitting the linear behavior of the implantation depth h as a function of cluster *velocity*, we found different straight lines for different cluster sizes (we have shown the linear dependence between implantation depth and cluster *momentum* in Sect. 5.5.2):

$$h = a_N + b_N v_0 \tag{5.4}$$

where h is the mean implantation depth expressed in meters ([m]), a_N and b_N are the fit parameters of the straight lines(expressed in [m] and [s], respectively), and v_0 is the initial velocity of the cluster.
As Pratontep *et al.* [27] pointed out, the latter equation is consistent with a linear dependence of cluster velocity v on distance x from the surface, arising from the application

of Newton's Law with a Stoke's type resistance force ($F = -bv$, where b is a constant). We can then derive the initial cluster kinetic energy E_0 in terms of the initial cluster velocity, v_0, to find:

$$E_0 = \frac{m}{2} \cdot \frac{h^2}{b_N^2} - \frac{ma_N}{b_N^2} \cdot h + \frac{ma_N^2}{2b_N^2} \tag{5.5}$$

We can assume that the latter quantity, with $h = x$, equals the loss of energy undergone by the cluster at a distance x from the surface. In other words, we can express the energy of the cluster at "distance x" in the form:

$$E = E_0(h) - E_0(x) \tag{5.6}$$

The *stopping power* is defined by $\frac{dE}{dx}$, the energy loss per unit distance, which means:

$$\frac{dE}{dx}(x) = \frac{m}{b_N^2} \cdot x - \frac{ma_N}{b_N^2} \tag{5.7}$$

Significant is the trend of the stopping power as a function of cluster velocity, for each cluster size. In eq. (5.7) we can insert the mentioned linear behavior of x vs v using eq. (5.4), and obtain:

$$\frac{dE}{dx}(x) = \frac{m}{b_N^2}(a_N + b_N v_0) - \frac{ma_N}{b_N^2} = \frac{m}{b_N} v_0 \tag{5.8}$$

This equation shows that the stopping power varies linearly with the incident velocity, with a slope which changes with the cluster size.

A consequence of the linear behavior of the implantation depth as a function of the cluster momentum is that the stopping power S shows a so called *molecular effect*, i.e.:

$$S(N) \propto N^{\alpha} S(1) \tag{5.9}$$

with $\alpha < 1$.

All the "stopping power vs velocity" curves have been scaled with the stopping power associated to the monomer, S(1). The resulting curve ($\frac{S(N)}{S(1)}$) is shown in Fig. 5.15, together with the fitting curve $\beta\, N^{\frac{2}{3}}$, with $\beta = 0.73 \pm 0.03$. Analyzing our data yields a good agreement with the fit $N^{\frac{2}{3}}$, which relates the term N^{α} (Eq. 5.9) to the projected surface in the sphere model.

This "molecular behavior" is consistent with previously reported results [100–102], obtained both in the case of heavy ions incident on a light target and in the case of a mass ratio equal to one. This phenomenon is explained by assuming that the earlier arriving cluster atoms knock out the target atoms and *clear the way* for the late-coming cluster atoms [100].

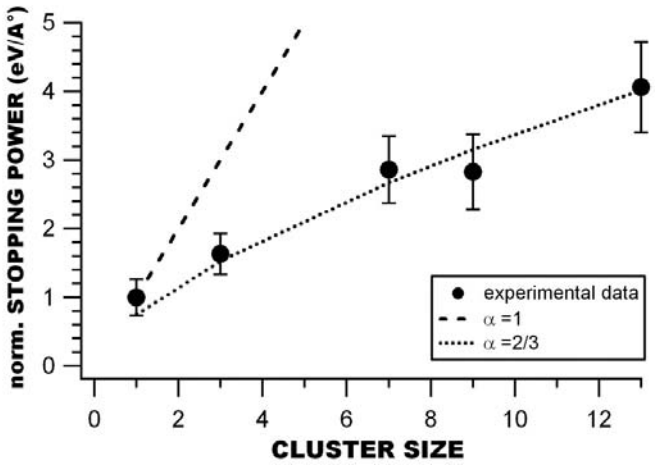

Figure 5.15: Stopping power normalized with the curve associated to the monomer. Two different N^{α} curves are shown ($\alpha = 1$: no molecular effect, $\alpha = \frac{2}{3}$: projected surface in the sphere model.)

5.6 Conclusions

In summary, we have reported a systematic study of the implantation of silver clusters into a graphite substrate, for different cluster sizes and over an extended energy range. First we have found a linear dependence between the *penetration depth* and the *momentum* of the cluster, for each cluster size. This result is in good accordance with previous results for the impact of C_{60}^{+}, Ag_7^{+} and Au_7^{+} on the same substrate.
In addition, we have investigated the effects of the cluster *geometry* on the implantation into the graphite substrate. The step from the simple liquid drop model to the actual calculated geometry of the cluster improved considerably the model.
Finally we have investigated the stopping power "felt" by Ag clusters of different sizes, while penetrating the HOPG substrate. An important question is whether the stopping power is simply linear with the number of atoms N in the cluster. Our data clearly show a *molecular behavior*, meaning that the stopping power per cluster atom is smaller than the stopping power for atomic projectiles moving at the same velocity. In particular, we were able to quantify this molecular effect.

Chapter 6

Electron Emission in Ag_N^+ - surface collisions

A brief summary of the current theories for interpreting secondary electron emission induced by ion-surface collisions will be given in the beginning of this chapter. This is followed by a presentation of the experimental results, which are discussed in terms of recent models about subthreshold emission, molecular effects and charge exchange dynamics.

6.1 Introduction

A common phenomenon (among others) in particle-surface collisions is the excitation of the substrate or particle electronic system and subsequent electron emission (EE). The study of EE provides insight in the underlying physical phenomena during impact. Apart from the fundamental interest in these phenomena, EE finds its applications for example in particle detectors, in the understanding of gas discharges and the generation of charged cosmic dust.

Secondary electron emission from positive atomic ion impacts has been studied since the beginning of the Twentieth Century [103], but the theoretical understanding of secondary electron emission was poorly developed until the 1930's. Today, EE in ion-surface collisions is a mature field in physics [39] and different processes have been found to explain the electron emission process.

The process which carries no collision energy threshold is *potential emission* (PE), which is possible when the ionization potential of the projectile is at least twice the work function of the substrate. The process is qualitatively understood as a resonance neutralization of the projectile ion leaving an excited electron, which then transfers its energy

to emit a conduction electron in an Auger de-excitation process [104]. The second important process is *kinetic electron emission* (KEE) which in contrast is strongly impact velocity dependent. In its most straightforward case, the valence electrons of the solid become excited in binary collisions and are ejected into vacuum. The target electrons are treated as an idealized Fermi electron gas and a classical momentum transfer approach is taken. This model is applicable at elevated projectile energies and characterized by a well defined velocity threshold, which ranges about $10^4 - 10^5 \frac{m}{s}$. However, numerous experiments on KE well below this threshold are reported [105–107]. The understanding of the energy transfer during low energy collisions is more subtle and localization of the electronic wavefunction due to the presence of the surface as well as electron correlation have to be taken into account. This so called *subthreshold KE* has been observed to increase in importance with increasing Z number of the projectile [105,108,109]. Extensive studies by Lörinčík and Winter [107,110] on the Xe and Au on Au systems clearly reveal these phenomena. If, instead of atomic ions, molecular ions or clusters are used as projectiles still a large number of open questions exist. In the case of metal clusters we can, due to the delocalization of the valence electron wavefunctions inside the cluster, think of the impact of a "superatom". In the context of the discussion above we would expect an enhancement of the subthreshold effects and in particular of the many-electron contribution to the emission yield.
Recent experiments by Meiwes-Broer *et al.* [41] have shown an oscillatory behavior in the electron emission yield as a function of cluster size at fixed impact energy. These results have been explained by a time-dependent charge transfer in the cluster ion-solid collision, so called Stückelberg oscillations. These oscillations, according to the authors, reflect themselves in a non-monotonous emission of secondary electrons. Following this idea, electron emission would yield information on the charge exchange dynamics of the cluster-surface collision process.
However, it should be kept in mind that the detailed understanding of electron emission from surfaces impacted by atomic ions is a challenging theoretical problem which is far from being fully explained.

6.2 Electron emission theory

We will discuss the main mechanisms by which *particle*-surface[1] collisions can excite electrons above the vacuum level.

Fig. 6.1 recalls some properties of solids which are important parameters in electron

[1]We denote by *particle* any neutral or charged atom, molecule, or cluster.

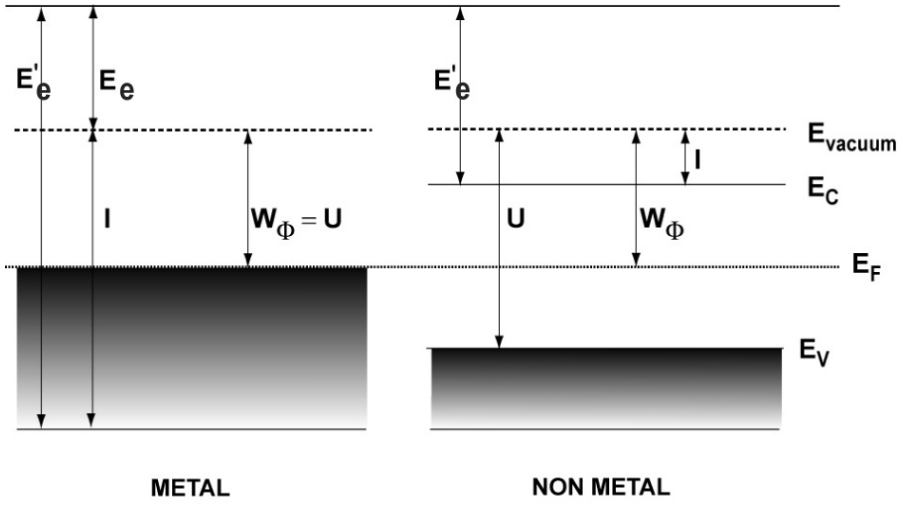

Figure 6.1: Schematic energy bands for metals and non-metals, with energies relevant to electron emission. W_Φ is the work function; E_F, Fermi energy; U, minimum binding energy; I, inner potential; E_v (E_c), top (bottom) of valence (conduction) band; E_e (E'_e), electron kinetic energy outside (inside) the solid. From Ref. [105].

emission. The quantity U is the minimum energy required to extract an electron from the solid into infinity. In the case of metals, U corresponds to the *work function* W_Φ, while for non-metals this energy corresponds to the sum of the band gap energy and the electron affinity. The *surface barrier height* indicates the energy an electron loses when going from the solid into the vacuum. This energy equals the inner potential[2] I, which corresponds to the sum $E_F + W_\Phi$ in the case of a free-electron metal, and to the electron affinity in the case of non-metals.

The electron wave functions decay exponentially outside the surface of the solid, and are considerably distorted by the projectile approaching of the surface. An accurate description of the surface-projectile interaction is very important in treating electron transfer between the surface and the projectile. Charge-transfer processes may eventually lead to electron emission.

As cited in the introduction, we can distinguish two different electron emission processes. The first one is *potential emission* (PE), where the energy received by the emitted electrons comes from an internal energy loss of the projectile. Thus, projectile "internal properties" such as its chemical configuration, charge state, electronic, vibrational or rotational state are of foremost importance, while the kinetic energy and the mass of the projectile are not concerned. The typical time scale of this process is in the range $10^{-13} \div 10^{-16}\, s$. On the other hand, *kinetic emission* (KE) is caused by transfer of

[2]energy that an electron gains when entering the solid.

kinetic projectile energy onto the electrons and atomic cores in the solid, which may lead to the ejection of electrons from the solid surface. In general terms, for intermediate and high energies ($E_{kin} > 1\,keV/amu$) the kinetic emission is dominant with respect to the potential one, while for low energies KE is negligible.
Among the general reviews which treat the topic of ion-induced electron emission we cite the one by Hasselkamp [38], which deals with kinetic electron emission from massive targets under heavy-particle bombardment, and the one from Varga and Winter [39], which is about potential emission. More recent developments in both *potential* and *kinetic* electron emission from solids have been treated in [105].

6.2.1 Potential emission

The basic ideas in Potential Electron Emission (PEE) by the Auger mechanism were developed by Hagstrum in the mid-1950s, both from an experimental [111,112] and from a theoretical [113] point of view. He treated the processes as electronic transitions between the unperturbed solid and a projectile with high potential energy (positive/negative ion or excited atom).
In PEE, electron excitation results from the conversion of internal energy ε brought by the projectile, through an Auger process. Different forms of processes can occur [39, 105], depending on the origin of the two electrons participating in the *Auger transition* (Fig. 6.2(a)).
The projectile ion can de-excite directly by a two-electron interatomic ***Auger neutralization*** (**AN**). This process can eject an electron from the surface valence band if the involved neutralization energy is at least twice the work function W_Φ. Two electrons of the surface valence band will be involved, one neutralizing the ion, and the other one (gaining energy via electron-electron interaction) being ejected with a maximum kinetic energy E_e. This kinetic energy is related to the neutralization energy W_i[3] by the following expression:

$$E_e \leq W_i - 2W_\Phi \tag{6.1}$$

The energy distribution of emitted electrons corresponds to a self-convolution of the electronic surface density of states (S-DOS) and depends on the Auger transition matrix elements and the available potential energy W_i.
An excited particle in the absence of available empty resonant levels in the valence

[3] W_i corresponds to the "effective recombination energy" of the neutralized particle, which decreases (in the case of atomic projectiles) with the process taking place closer to the surface because of an increasing level shift with decreasing distance.

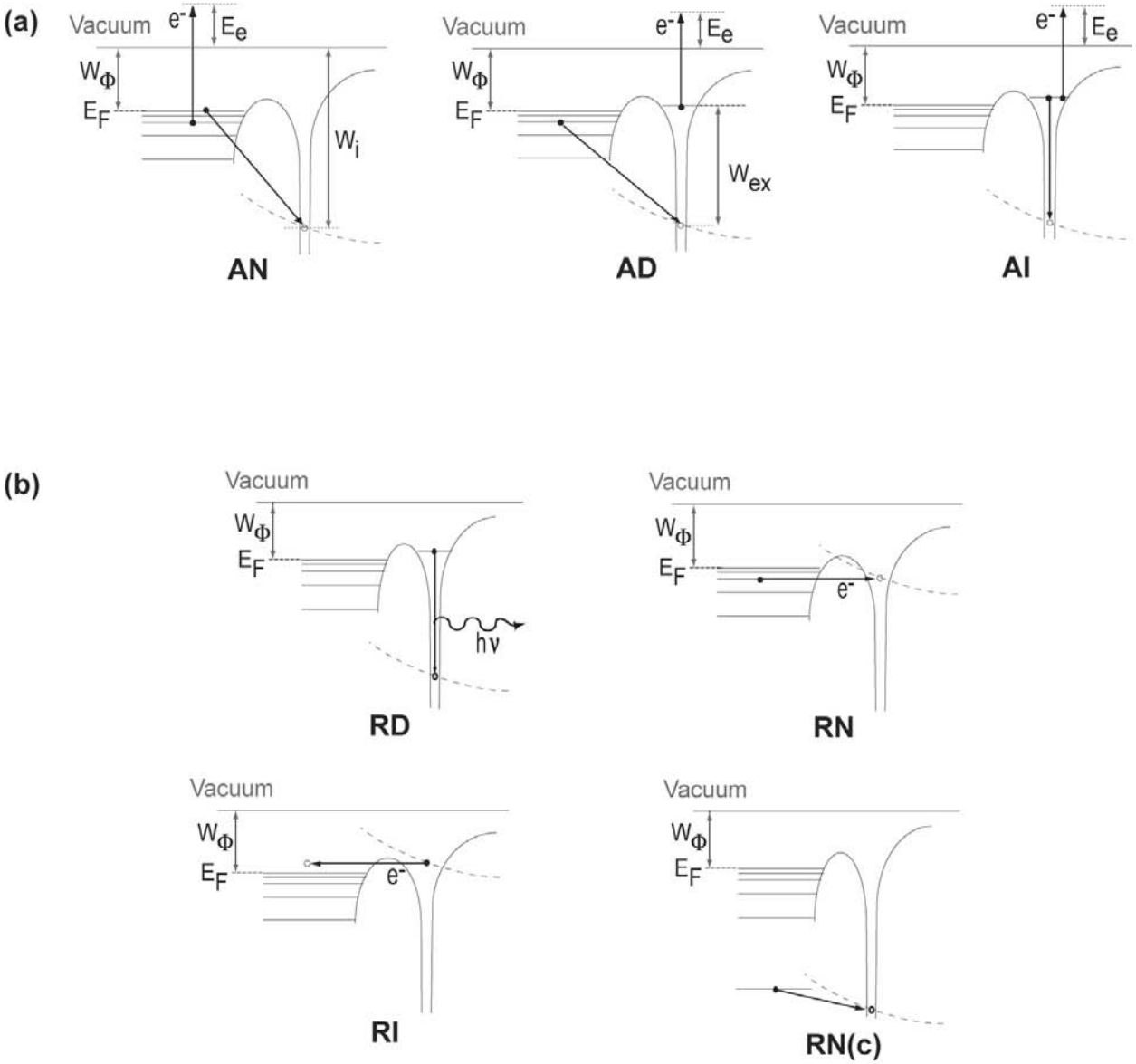

Figure 6.2: Potential energy diagrams showing transition and de-excitation processes for ions and excited atoms in front of a surface. W_Φ is the work function, E_F is the Fermi energy, and E_e is the kinetic energy of possibly emitted electrons. Full dots indicate occupied states, open circles indicate free states. The shift of the electron energy levels with distance is indicated qualitatively by dashed lines. (a) Two-electron transitions: AN, Auger neutralization; AD, Auger de-excitation; AI, Autoionization. (b) One-electron transitions: RD, Radiative de-excitation; RN, Resonance neutralization; RI, Resonance ionization; RN(c), Resonance neutralization from core level.

band[4] may interact with an electron of the valence band, giving rise to an ***Auger de-excitation*** process (**AD**). The such excited electron can be ejected from the particle while a surface electron is transferred into a lower particle state. The maximum energy of the emitted electron is given by

$$E_e \leq W_{ex} - W_\Phi \tag{6.2}$$

with the excitation energy W_{ex} being independent of the particle-surface distance (therefore also of the particle velocity), since the initial and final charge states are identical and thus subject to similar level shifts. The energy distribution of emitted electrons reflects the electronic surface density of states (S-DOS) folded by an energy-dependent escape probability.
The intra-atomic Auger process involving two or more electrons belonging to a doubly-multiply excited atom or ion, is termed ***Autoionization*** (**AI**). In this case, one or more electrons are emitted and one is transferred to a lower state of the particle. As all the electrons involved in this process belong to the projectile atom, relatively narrow energy distributions of emitted electrons can be expected. The energy E_e of emitted electrons results from the potential energy difference of the particle before and after the transition.

Among one-electron transitions of an excited atom-ion in front of a surface, the ***Radiative de-excitation*** (**RD**) (Fig. 6.2(b)) consists in a de-excitation of the projectile by emission of a photon. For singly charged ions approaching a surface, this *dipole radiation* process is highly improbable, because the involved radiative lifetimes of typically 10^{-8} s are about 10^6 s times longer than the transition times for radiationless de-excitation. For highly charged ions, on the other hand, radiative de-excitation can become competitive, because of their rapidly increasing radiative transition rates.

Resonance transitions (Fig. 6.2(b)) into excited projectile states generally dominate the particle-solid interaction because of the much larger spatial extension of the involved wave functions in comparison to the corresponding ground states. As a consequence, such resonance transitions can take place already at a rather large distance from the surface. These kind of processes are non electron-emitting precursors for the subsequently possible electron-emitting two-electron transitions, described above. In particular, electronic transitions near solid surfaces may de-excite and neutralize incoming projectiles, in a two-stage process of ***resonance neutralization followed by***

[4]This happens if the binding energy $W_i - W_{ex}$ of the excited electron in the particle is larger than the surface work function W_Φ.

Auger de-excitation. The projectile, in this case, carries potential energy by virtue of the fact that it is excited, ionized or both. This combined process of neutralization and de-excitation may give rise to electron emission.
Resonance neutralization (**RN**) can occur when unoccupied electronic states in the incident ion become energetically degenerate with occupied states belonging to the surface valence band. The probability of this process depends on the overlap of the atomic wave function with the tail of the wave function of the electron in the solid.
Resonance ionization (**RI**) is inverse to RN, and takes place if the binding energy of an occupied excited state in the particle is smaller than the surface work function W_Φ, i.e. if empty levels in the conduction band become energetically resonant with occupied atomic levels.
Resonance neutralization from core level (**RN(c)**) is a near-resonant transition from more tightly bound localized target states (core states) to projectile states. Such processes can only occur in close collisions, since an interpenetration of the involved inner electronic orbitals has to be assured.

6.2.2 Kinetic emission

The mechanism of *kinetic electron emission* (KEE) consists of three steps. The first one is the *generation* of excited electrons in the solid. This is followed by the *diffusion* of the excited electrons towards the surface (and excitation of other electrons by $e^- - e^-$ collisions), and terminated by the *escape* of secondary electrons through the surface barrier *into the vacuum*. As the mean free path of electrons in the solid is of the order of ten Å, only those secondary electrons which come from the first few monolayers will be detected outside the surface.

There are several ways in which slow heavy projectiles can excite electrons at the expense of their kinetic energy. The two established kinetic-excitation mechanisms [38,105] are ***direct binary collisions*** with target valence electrons and ***electron promotion*** due to electron-electron interaction. Light projectiles excite mainly by direct binary collisions while the heavier projectiles excite more efficiently by the second mechanism. At velocities larger than the Fermi velocity of target electrons, another process becomes important. The projectile can efficiently excite surface and bulk plasmons which decay mainly through the creation of electron-hole pairs. The electrons may then be ejected into vacuum with a maximum energy equal to the plasmon energy minus the work function. We will not enter into the details of this high-energy process, as all the projectile velocities employed in this thesis work are largely below the Fermi velocity of target

electrons.
We will start the discussion by illustrating the two established kinetic emission mechanisms cited above. However, kinetic electron emission is observed at very low impact velocities, well below the velocity thresholds associated to the two mentioned processes. A recent very interesting mechanism will be finally introduced, which accounts for the observed subthreshold kinetic emission and well interprets experimental data.

The *classical* model

The ***binary approximation*** is valid if the solid valence-band electrons can be considered as nearly free, i.e. if the interaction with the projectile is much stronger than that with their parent atom. The model of binary collisions with free electrons was first tested by Baragiola and coworkers [114] for proton impact on different metal surfaces, in the energy range 2-50 keV (impact velocities $v < v_F$). In this model the electron excitation results from the screened Coulomb interaction between the projectile and the target electrons through direct binary collisions. The conservation laws of momentum and energy, however, allow only a small amount of energy to be transferred to the target electron, due to the strong mismatch between the masses of the electron, m, and of the heavy projectile, $M \gg m$. The maximum energy transfer to an excited electron occurs when an electron at the Fermi surface, with momentum anti-parallel to the projectile, scatters into a final state with momentum parallel to the projectile. It is given by:

$$\Delta E_{max} = 2mv\,(v + v_F) \tag{6.3}$$

The excited electron is directed inwards but can be observed outside due to the strong elastic scattering with the target atomic cores.
The threshold velocity for ejection of an electron into vacuum, v_{th}, will be that at which the maximum energy transfer equals the work function W_Φ, that is:

$$v_{th} = v_F/2(\sqrt{1 + W_\Phi/E_F} - 1) \tag{6.4}$$

where v_F and E_F are the Fermi velocity and the Fermi energy, respectively. This **classical** threshold is usually in the speed range of $0.4 - 4 * 10^5$ m/s.

Kinetic emission below this classical velocity threshold (*subthreshold KE*) has been recently observed in the case of 3 keV impact of Au^+ on Au [106], and for polycrystalline gold bombarded by C^+, N^+, O^+, Ne^+, Ne^0, Xe^+ and Au^+ [107]. It was also previously observed for many other collision systems (Ref. [105] and references therein), becoming gradually more important for heavier projectiles. Thus, the above described classical

model has to be replaced by another mechanism which can account for this subthreshold KE.

The *promotion* model

Until recently, the only available explanation for the subthreshold KE was given in terms of the ***promotion model***.

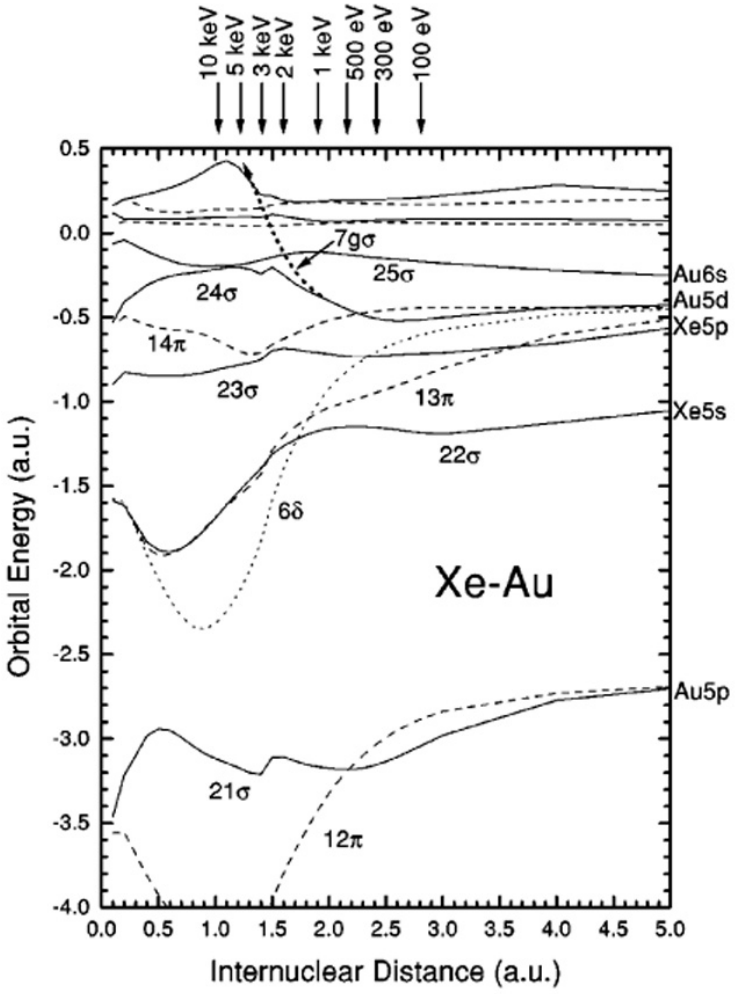

Figure 6.3: Adiabatic molecular-orbital (MO) correlation diagrams for the selected orbitals of Xe-Au (from [107]). The right hand side of the diagram indicates the levels for the separated-atom limit, and bars on top indicate projectile energies corresponding to the distances of closest approach indicated on the x axis. On the graph, solid lines correspond to σ-levels, dashed lines to π-levels, dotted lines to δ-levels, and the dotted heavy curve with an arrow indicates the promotion of a *diabatic level* into continuum. As regards the *adiabatic levels*, the lowest orbital of a given symmetry is numbered 1, and numbering increases with increasing energy.

This model has been first introduced and developed to explain electron emission in ion-atom collisions [115–117] and later applied to the scattering of neutral or ionic projectiles at surfaces [118, 119]. It involves the promotion of electrons to higher energy levels in the quasi-molecular state formed temporarily as the projectile and a target atom or a recoil and another target atom collide[5]. When inner shells of the colliding atoms are promoted in energy, electrons can be transferred into partially or totally empty outer shells.

Vacancies are then formed in inner shells of the projectile and/or the target atom. Typical lifetimes τ of these holes are in the range 1 to 100 fs [120]. The main decay mode for inner holes is an Auger mechanism. In this process, an electron from an outer shell fills the inner-shell vacancy, and the excess energy is given to another electron, which is ejected with an energy related to the energies of the intervening shells. If the core-excited atom decays inside the solid, the Auger energies will represent approximately a convolution of the DOS of the valence band at the location of the inner-shell hole. Otherwise, if the excited atom moves away from the excitation site and decays outside the solid, the Auger energies would correspond to that of a free atom (modified by the interaction with the surface).

Excited inner-shell vacancies can also radiatively decay emitting an X-ray photon. However, this emission mode has a low probability, typically a few percent or less for transition energies of a few hundred eV or less.

To better illustrate the promotion model, let us consider a *slow* encounter between a Xe^+ ion and a gold target atom. The term "slow" indicates collisions characterized by impact velocities much smaller than typical orbital velocities of inner-shell electrons (*near-adiabatic* collisions). During the interaction of the projectile with a target atom a quasi-molecule Xe-Au is formed. The MO correlation diagrams for this system are depicted in Fig. 6.3. In these diagrams, the energies $\varepsilon_i(R)$ of quasimolecular electronic orbitals[6] $\phi_i(\mathbf{r}, R)$ are plotted as a function of the internuclear distance[7] R in the di-atomic collision complex. At infinite separation the electron energy levels are those of separated atoms (right hand side of the diagram). The rules for drawing a *correlation diagram*

[5]The picture of a transient quasimolecule includes the limiting case of a "quasiatom" which is formed if the minimum internuclear distance between the collision partners is much smaller than the sum of their K-shell radii. In this case, the inner-shell electrons "feel", for a short time, the screened Coulomb field of a combined nuclear system with charge number given by the sum of the projectile and target charge numbers. If the sum exceeds the charge number of the heaviest known element, one may speak of the formation of "superheavy quasiatom" [117].

[6]The electronic coordinates $\mathbf{r}$ are referred to a body-fixed (molecular) frame of reference.

[7]This distance is expressed in *atomic units*, where $1 a.u. = 0.053\, nm$.

are discussed in detail by Barat and Lichten [116]. Following these rules, as indicated in Fig. 6.3, the diabatic level $7g\sigma$ level is promoted to the continuum. This promoted level merges into the continuum above the vacuum level at the internuclear distance $r_c \simeq 1.5\,a.u.$. The promotion of this level can create a vacancy in the Au$5d$ level, which may be transferred by *vacancy sharing* [121] into the Xe$5p$ level. De-excitation of the latter can give rise to further electron emission.
We will not enter into further details of this mechanism, for which the reader is referred to other numerous papers [115–119]. We should only stress that this process is characterized by a threshold center-of-mass energy for excitation, related to a critical target-projectile distance r_c which must be attained to promote the inner-shell orbital:

$$E_{th,cm} = V(r_c) \tag{6.5}$$

where V(r) is the interatomic potential.
This *minimum* distance can be experimentally determined and theoretically estimated from the analysis of molecular-orbital (MO) correlation diagrams.

The *Parilis-Kishinevskii* model

Another process which can give rise to subthreshold kinetic emission is the one proposed by **Parilis et Kishinevskii** [122]. They suggest that, as a result of binary collisions between the projectile and lattice atoms, holes are created in the core levels of the latter. A bound core-level electron is excited to the conduction band of the target, so that a subsequent Auger recombination process can possibly release enough energy for a conduction electron to be emitted over the surface barrier (Fig. 6.4).
The calculation of the cross section to excite an electron from a filled shell to the conduction band (process (1) in Fig. 6.4) leads to the following expression [122]:

$$\sigma(v) \;=\; \frac{1.39{\cdot}a_0{\cdot}\hbar}{J}{\cdot}\Big(\frac{Z_1+Z_2}{\sqrt{Z_1}+\sqrt{Z_2}}\Big)^2{\cdot}S(v) \tag{6.6}$$

where a_0 is the Bohr radius, J is the average ionization potential for the outer shells of an atom, Z_1 and Z_2 are the nuclear charges. S_v contains the dependence to the projectile velocity, and can be approximated by:

$$S(v) \;\propto\; v{\cdot}\arctan\, B{\cdot}(v - v_{thresh}) \tag{6.7}$$

where B is a constant and v_{thresh} is a threshold velocity. These parameters have been calculated for Ar^+ and Kr^+ impacting on W and Mo. The constant B is approximately $0.6 \cdot 10^{-5}\,(s/m)$ (almost independent on the colliding species), and v_{thresh} is found to

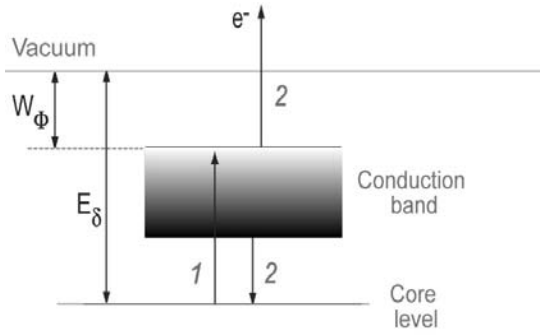

Figure 6.4: Scheme of the kinetic electron emission process proposed by Parilis and Kishinevskii. 1) An electron from a filled core-level shell of a target atom is excited into the conduction band, 2) Another e^- from the conduction band recombines with the hole created by the first electron in the core-level shell, and the energy released can be transferred to another conduction electron which may gain enough energy to be emitted over the surface barrier.

yield $0.6 - 0.7 \cdot 10^5\,(s/m)$ (depending on the considered system).
$\sigma(v)$ has a pronounced threshold v_{thresh} which is lower than the classical one, due to the fact that the electron emission originates from the excitation of a bound electron. Below this threshold, the energy transfer does not attain $E_\delta - W_\Phi$ and excitation of a bound electron is not possible. Above this threshold, starting from Eq. 6.7 we can distinguish two different regions for $\sigma(v)$ (Eq. 6.6): a region of low velocities ($v < 3{\cdot}10^5\,m/s$) where the function $\sigma(v)$ is almost quadratic, and a region of high velocities, where the function is approximately linear.
The above calculated cross section, $\sigma(v)$, is actually the cross section for the formation of an electron-hole pair. We should now consider the recombination of a conduction electron with the formed hole and the transfer of energy to another conduction electron. The energy requirement [122] to have electron emission is that the binding energy of core electrons is larger than twice the work function of the solid ($E_\delta > 2W_\Phi$) (Fig. 6.4). The probability $\omega(E_\delta)$ of extracting an electron as a result of Auger recombination of an electron with a hole, increases with the depth of the filled band δ in which the electron is located, i.e.:

$$\omega(E_\delta) \;=\; 0.016 \cdot (E_\delta - 2W_\Phi) \tag{6.8}$$

To calculate the number of ejected electrons, we have to consider the collisions that the secondary electrons produced inside the solid experience prior to leaving the surface. Assuming that the flow of secondary electrons decreases exponentially with the path

length λ, the number of emitted electrons per single incident ion at the surface equals:

$$\gamma = \int_0^{x_n} \sigma(v) \cdot w(E_\delta) \cdot N \cdot e^{-\frac{x}{\lambda}} dx \tag{6.9}$$

where N is the number of metal atoms per unit volume, and x_n the depth at which the ion can still excite the target inner shell electrons. Taking into account the decrease in ionization cross section ($\Delta\sigma(v)$) related to the retardation of the ion in the metal, and calculating the integral in Eq. 6.9, leads to the following final formula for secondary electron yield γ:

$$\gamma = N \cdot \sigma^*(v) \cdot \lambda \cdot \omega(d) \tag{6.10}$$

where $\sigma^*(v)$ is an *effective cross section* equal to $\sigma(v) - \Delta\sigma(v)$.
The behavior of γ as a function of the velocity is contained in the $\sigma^*(v)$ term, which has been extensively commented above (Eq. 6.6, 6.7). The PK theory successfully explained the velocity dependencies of secondary electron emission from Ar^+ and Kr^+ incident on Mo and W [122].

However, there are many experiments, especially with very low-energy ions (hundreds of eV), where the two mechanisms cited above cannot explain the kinetic electron emission and where the particle velocity is too low to produce electrons by classical particle-electron collisions.
Another relevant mechanism for subthreshold kinetic emission has been recently suggested by Lörinčík and coworkers [107,110]. In what follows, the fundamental principles of this model are presented, as it will be used later to fit our experimental data.

The *"surface assisted"* and *"many-electrons surface assisted"* KE models

The basic assumptions of this model are the **partial localization** of the target valence electrons and their **non-adiabatic** time-varying perturbation due to the rapid passage of the particle through the surface. Semi-localization can be due either to the partially d-character of the valence band, or to the confinement of the electrons by the surface of the solid, or to the intrinsic localized character of valence wave functions due to the orthogonality to the inner-shell wave functions.
In this one-electron non-adiabatic model (**"surface-assisted kinetic emission", sKE**), the perturbing potential V(r) of the moving particle causes a direct interaction between the occupied and unoccupied levels of the continuum. This *time-varying* excitation in the solid is modelled by the matrix elements $V_{kk'} = \langle k | V(r) | k' \rangle$, where the wave functions of the occupied $|k'\rangle$ and unoccupied $|k\rangle$ levels are semi-localized by

the presence of the surface. These matrix elements are actually independent of k, k' ($V_{kk'} = V$), because the potential is assumed to be an s scatterer. The dependence of $V_{kk'}$ on time, is contained in the *relative* coordinate $r = \mathbf{r} - \mathbf{v}t$, which contains the dynamics of the projectile movement. The *spatial dependence* of the perturbing potential (constant inside the solid and smoothly decreasing to zero outside) can then be transformed into a *temporal dependence*. The potential V(t) is expressed in the form VF(t), where $F(t) = \frac{1}{\cosh(2\gamma v t)}$ describes the on/off switching character of the interaction. A first *adjustable parameter* γ is introduced, which characterizes the dynamics of the wave function overlap during the particle-surface interaction.

For small velocities ($e^{-\frac{\pi W_\phi}{2\gamma v}} \gg 1$), the following analytical expression for the sKE yield has been derived:

$$\gamma_{sKE} = 2\xi\rho^2 V^2 \left(\ln\left(e^{-\frac{\pi W_\phi}{2\gamma v}} + 1 \right) - \pi^{\frac{1}{2}} \left(-\frac{\pi W_\phi}{2\gamma v} \right)^{\frac{1}{2}} erfc\left(\left(-\frac{\pi W_\phi}{2\gamma v} \right)^{\frac{1}{2}} \right) \right) \qquad (6.11)$$

where the term $\rho^2 V^2$ is proportional to the electronic stopping of the moving projectile in the solid. This term is quantitatively evaluated from the Lindhard-Scharff formula [123] and is adjusted by the *correction factor* ξ.

It should be stressed that the **sKE model**, due to the semi-localization of valence band wave functions, **does not predict any cut-off impact velocity**. Eq. 6.11 fits the experimentally observable KE subthreshold contribution for clean poly-crystalline Au bombarded by light singly charged ions [107, 110].

On the other hand, the experimental data related to the impact of heavy ions on the same gold target show a subthreshold kinetic emission in the very low impact velocity region, which cannot be explained by the one-electron theories so far presented. Lörinčík and coworkers [107, 110] extended the sKE model to a many-electron model (**"many-electron surface-assisted kinetic emission", mKE**), for interpreting these very low impact velocity KE data.

This model starts with the basic assumptions of the sKE model, i.e. the semilocalization of the electron wave functions due to presence of the surface, and the same shape and character of the perturbing potential. The new key assumption of the mKE model, resides in the fact that at very low projectile velocities the electronic excitation remains localized for a sufficiently long time (some fs) close to the target surface. The energy distribution of excited electrons can then be broadened due to fast ($\sim 10^{-16}\, s$) e^--e^- interactions.

A new parameter, ε_0, is introduced, which characterizes the width of the energy distribution of the redistributed part of the excited electrons. Without entering into the details of the calculation (for which the reader is referred to Ref. [107]), the analytical

expression for the electron emission yield is given by:

$$\gamma_{mKE} = 2\xi\rho^2 V^2 \Bigg(\ln\left(e^{-\frac{\pi W_\phi}{2\gamma v}} + 1\right) - \pi^{\frac{1}{2}} \left(-\frac{\pi W_\phi}{2\gamma v}\right)^{\frac{1}{2}} erfc\left(\left(-\frac{\pi W_\phi}{2\gamma v}\right)^{\frac{1}{2}}\right) + \\ + \frac{\pi\gamma v}{6\varepsilon_0}\left(e^{-\frac{W_\phi}{\varepsilon_0}} - \pi^{\frac{1}{2}}\left(-\frac{W_\phi}{\varepsilon_0}\right)^{\frac{1}{2}} erfc\left(\left(-\frac{W_\phi}{\varepsilon_0}\right)^{\frac{1}{2}}\right)\right)\Bigg) \tag{6.12}$$

For $\varepsilon_0 = 0$ Eq. 6.12 reduces to Eq. 6.11. The mKE model can then be interpreted as a "many-electron" extension of the sKE model.

6.3 Experimental procedures

The study of electron emission induced by cluster impact on surfaces involves a certain number of operations. The fundamental steps of the experimental procedure are summarized below. The reader is referred to Chapter 4, to obtain all technical information about the electron detection system and the related tools.

The HOPG sample is cleaved in air before being inserted into the *Deposition Chamber*. The sample holder is clamped by the *main manipulator* (Sect. 4.2.3), and the sample is cleaned by electron bombardment prior to deposition. When Pt(111) is employed as substrate, cleaning is performed by sputtering the sample with Ar ions (Sect. 4.2.4), followed by annealing.
The sample is then located behind the detector (Sect. 4.4.3), placed in front of the quadrupole, and irradiated by mass selected clusters produced by the *CORDIS ion source* (Sect. 4.3.1). To vary the clusters impact kinetic energy, the bias on the sample has to be varied. A *Faraday Cup* (Sect. 4.3.2) is employed to measure and control the incident cluster current. A well defined fraction of the beam passes the FC, is collimated and hits the sample surface which is negatively biased. The emitted electrons which reach the grid are detected by the channeltron (Sect. 4.4.3) in pulse counting mode.
The interesting quantity is the ratio γ between the number of emitted electrons and incident cluster ions. This quantity is acquired step by step by the computer, and plotted as a function of the cluster impact energy. This impact kinetic energy is also controlled by the computer, which increases the sample bias by user-defined steps.

6.4 Results

In the following the main results concerning electron emission are presented. These results will be discussed in detail in the next section.
The fundamental experiments consist in a systematic study of the emission yields following the impact of Ag_N^+ (N=1,2,3,5,7,8,9) clusters on HOPG, and of Ag_N^+ (N=1,2,3,4,5,8,9) clusters on Pt(111). In the case of silver clusters impact on HOPG, the incident kinetic energy ranges from 300 to 1800 eV and the emission curves are made of approximately 150 experimental points (corresponding to energy steps of 10 eV).

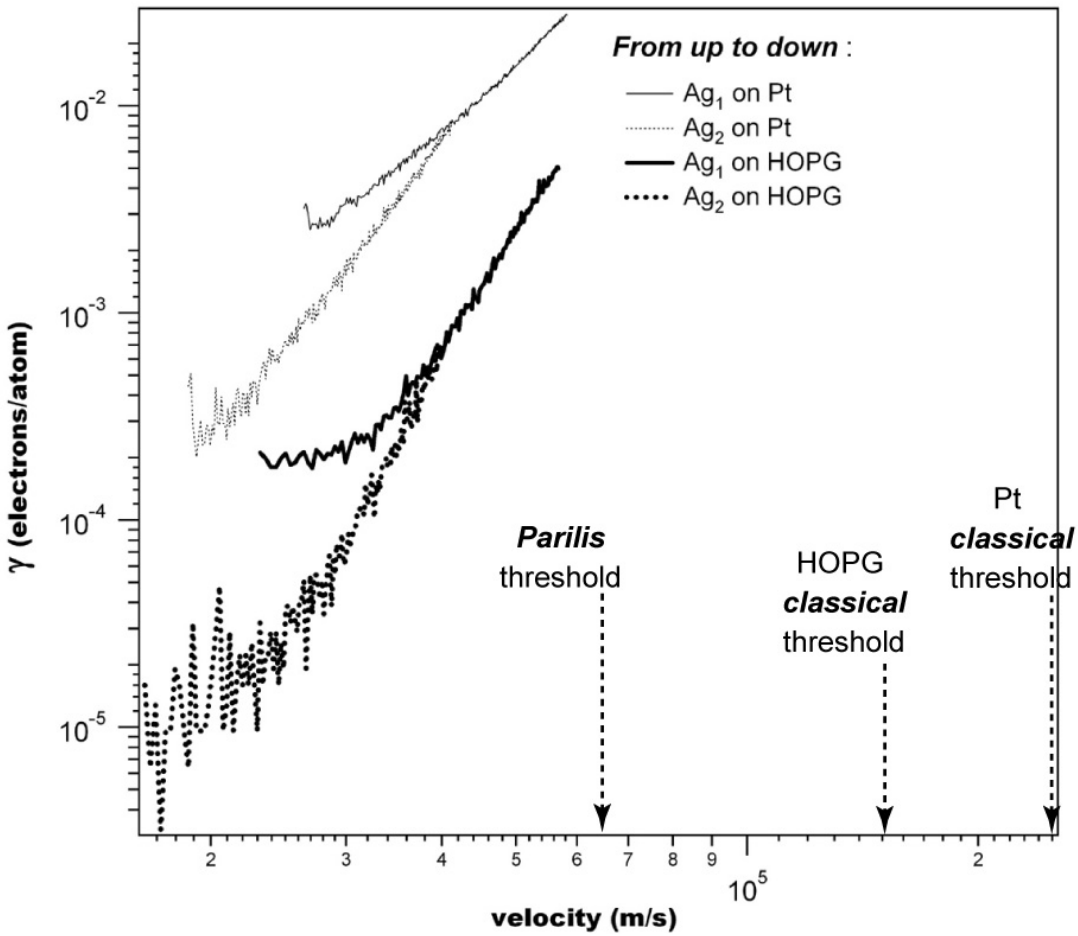

Figure 6.5: Electron emission following the impact of the silver monomer and the silver dimer on the HOPG and the Pt(111) substrates. From up to down, the curves are related to the impact of Ag_1^+ on Pt, Ag_2^+ on Pt, Ag_1^+ on HOPG, Ag_2^+ on HOPG. Potential emission is observed only in the case of the silver monomer, impacting on both substrates. KE thresholds associated to the *Parilis-Kishinevskii* model and to the *classical* model are also indicated.

In Ag_N^+ / Pt (111) experiments, the clusters impact energy ranges from 400 to 1900 eV

and the emission curves consist of 300 experimental points (energy steps of 5 eV). Remind that the measured quantity is the *yield* γ of electrons emitted from the target surface, defined as their total number per impinging projectile particle:

$$\gamma^\star = \frac{N_e}{N_p} \tag{6.13}$$

where N_e and N_p are the fluxes (particles per second) of electrons emitted from and projectiles arriving at the target surface. The electron yield γ that will appear in all the graphs presented in the following (if not otherwise specified) is a *normalized* electron yield. This quantity corresponds to the measured $\gamma^\star$ (as defined in Eq. 6.13) *divided* by the number of atoms *per cluster*. Using these *normalized* electron yields allows to compare the "yields per atom" for the different cluster sizes.

Fig. 6.5 shows the electron emission for the silver monomer and the silver dimer impinging on Pt and HOPG. While the emission yield γ decreases almost exponentially towards low velocities for the dimer (and for all larger clusters as shown below), it levels off at higher values in the case of the monomer. We attribute this behavior to a *Potential Emission* phenomenon, consisting in a combined process of neutralization and de-excitation of the projectile in front of the surface.

All collected electron emission data are presented in Fig. 6.6. The experimental data have been smoothed to better distinguish the behaviors associated to the different cluster sizes. Representatives of *original* emission curves are shown in Fig. 6.5.

We clearly remark higher emission yields for clusters impact on the Pt rather than on the HOPG substrate. This is due to the difference in the *density of states at the Fermi level*, which is higher for the Pt sample.

An interesting question is how the electron emission yield produced by cluster ions compares to the yields produced by the constituent atoms. Our data show a clear *molecular effect*, since the behavior of the emission yield as a function of the cluster size N is of the form $\gamma(N) \neq N\gamma(1)$. This molecular behavior is more pronounced in the case of silver clusters impact on HOPG.

The *classical thresholds* for both substrates are $v_{th}(\mathrm{HOPG}) = 150\,\mathrm{km/s}$, $v_{th}(\mathrm{Pt}) = 250\,\mathrm{km/s}$ (calculated from Eq. 6.4, and shown in Fig. 6.5). As these thresholds are not in the range of velocities we considered, the results presented in Fig. 6.6 indicate a "subthreshold kinetic emission". Among the different non-classical models described in Sect. 6.2.2, the one of Lörinčík and coworkers [107, 110] (see Sect. 6.2.2) is found to fit our experimental data very well. In particular, our emission curves have the same decreasing behavior vs the inverse velocity as the experimental data from Lörinčík and coworkers, concerning the impact of light projectiles on HOPG,

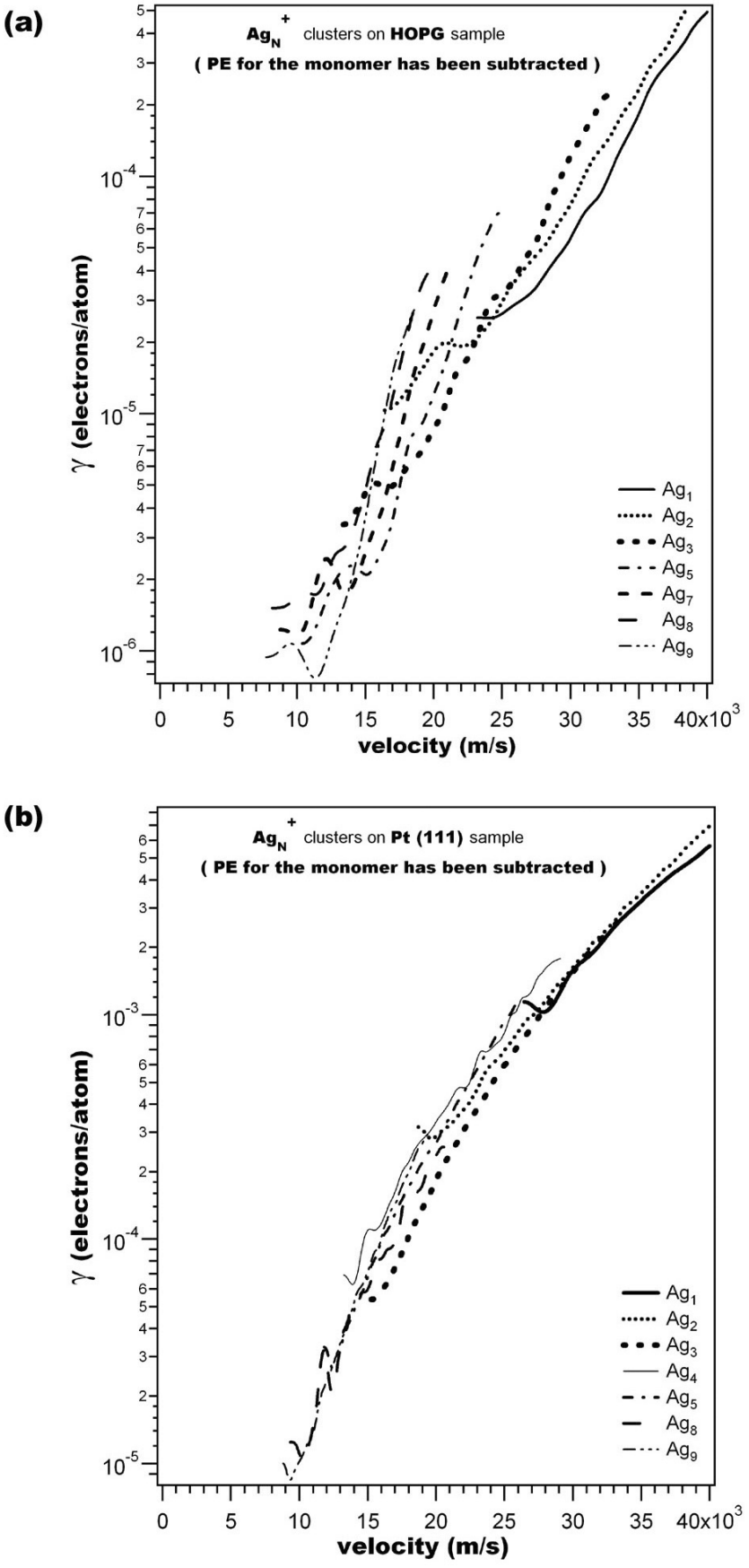

Figure 6.6: Emission yields for the impact of Ag_N^+ on HOPG and on Pt.

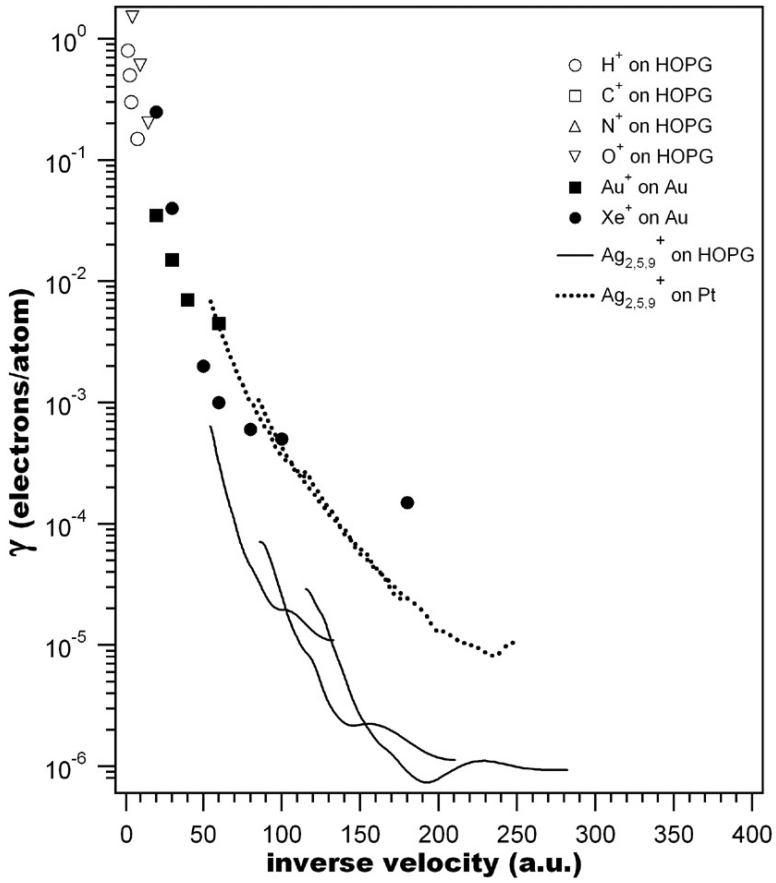

Figure 6.7: Measured electron emission for the impact of H^+, C^+, N^+, O^+ on HOPG, and Xe^+, Au^+ on Au (from Ref. [107]), compared to a selection of our data for the impact of Ag_N^+ and Pb_N^+ on HOPG and Ag_N^+ on Pt. All curves have a similar decreasing behavior as a function of the inverse velocity.

and of heavy projectiles on Au (Fig. 6.7). Again, the chosen "representative" emission curves have been smoothed for more clarity.

6.5 Discussion of the results

6.5.1 Potential emission for the monomer

We can interpret the monomer potential emission by the following considerations.
From sputtering of the silver target, both ground state and excited ions are obtained. If the *life time* τ of the ion excited state is **smaller** than the *time of flight* TOF of the same ion, this projectile will hit the target in its **ground state** (electronic configuration $4d^{10}$, from Fig. 6.8). In this case, **potential emission is energetically not possible**, as the condition $W_i > 2W_F$ is not satisfied with $W_i = 7.57\,eV$ and $W_F \simeq 5 - 6\,eV$

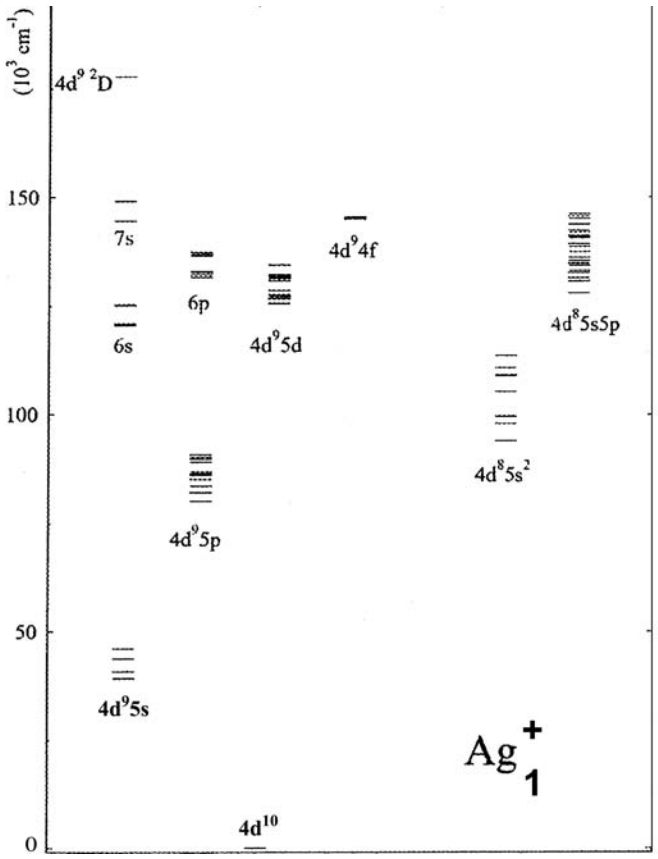

Figure 6.8: Overview of the Ag_1^+ energy level system. Adapted from Ref. [124].

$(W_F(HOPG) = 4.65\,eV,\, W_F(Pt) = 5.65\,eV)$.
On the other hand, if τ of the excited state is **larger** than the TOF of the same ion, this projectile will hit the target in its **excited state**. We interpret the monomer potential emission as due to a combined process of ***neutralization*** and ***de-excitation***. Within this picture, the Ag_1^+ would approach the target in its **metastable excited state**. The electronic configuration of this state is $4d^9 5s^1$, carrying an excitation energy $E_{ex} \simeq 5eV$ (Fig. 6.8). By interaction with the substrate, the projectile experiences a combined process of neutralization and de-excitation, the energy released in this process is $E_{tot} = E_{neutr} + E_{deexc} \simeq 12.5eV > 2W_F$. In this case, for both substrates the potential emission is energetically allowed.

The experimental data obtained for Ag_N^+ clusters (with N>1) do not contradict our interpretation. As a matter of fact, a potential emission is energetically not allowed for these clusters in their ground state, as the Ionization Potential decreases with size (see Fig. 2.4) and then the considerations given for the monomer in its ground state are still applicable.

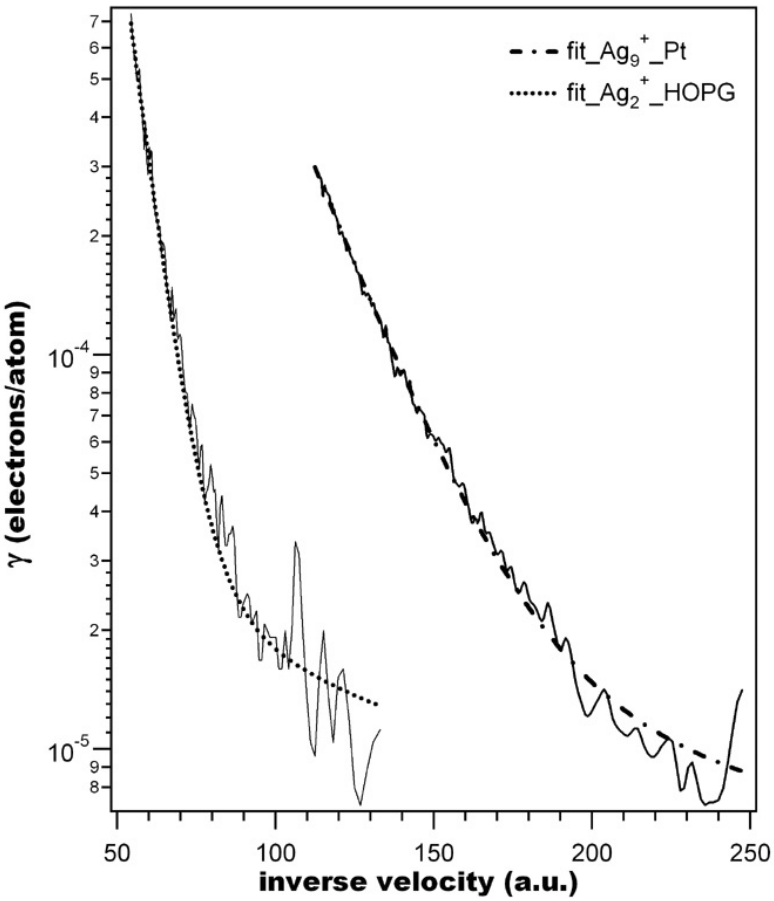

Figure 6.9: One model curve per projectile-target system fitted by the Lörinčík model (Eq. 6.12).

Moreover, to our knowledge, there are no metastable states for cluster sizes N>1. If this is the case, the above cited combined process of neutralization and de-excitation which explained the monomer potential emission would not be possible. According to this prediction, we don't observe any potential emission in our data for Ag_N^+ clusters with N>1.

6.5.2 Subthreshold kinetic emission: model of Winter and coworkers

The many-electron model proposed by Lörinčík and coworkers adapt very well to our system, consisting in *heavy projectiles* impacting on different surfaces. This model suggests an analytical expression for the electron emission yield (Eq. 6.12), which can directly be applied to experimental data.

Fitting our experimental curves with the expression contained in Eq. 6.12 yields satisfactory results. An example of how the fit expression adapts to our electron emission data

is presented in Fig. 6.9. Only one "model" curve per projectile-target system is shown. It has been slightly smoothed, not to make the graph too heavy with undistinguishable lines. The accordance between fits and experimental data is remarkable.
All our electron emission yields curves have been fitted with the expression contained in Eq. 6.12, and the best fit parameters have been plotted as a function of the cluster size. Results are shown in Fig. 6.10 and Fig. 6.11. We just remind the meaning of the different parameters, but the reader is referred to Sect. 6.2.2 for a more complete illustration of the "mKE" model.
ρ is the electronic density of states at the Fermi energy and V quantifies the particle-solid interaction potential (scattering matrix element). The term ρ^2V^2 is related to the electronic stopping of the projectile in the solid, and it is quantitatively estimated using the Lindhard-Scharff formula [123]. ζ is a "correction" factor which adapts the calculated ρ^2V^2 product to experimental data. In general, the correction factor seems to become more important for larger cluster sizes. This ζ behavior is probably related to the domain of applicability of the Lindhard-Scharff formula. This formula is better adapted to the smaller sizes and partially looses its validity as the cluster size increases[8].
The γ parameter characterizes the *high-velocities* emission yield behavior, and it is associated to the dynamics of the changing wave function overlap during the particle-surface interaction. A special trend in the dependence of γ on the *size* of the projectile can be observed, the parameter becoming larger for projectiles with more electrons. This result is reproducible for all considered systems, and consistent with the results of Ref. [110]. The authors in Ref. [110] suggest a relation between the increase of γ and the increasing inner shells electron emission contribution in projectiles with many electrons [110].
Finally, the ε_0 parameter is related to the fit of the very low-velocity emission yield data. The model includes electron-electron interactions due to a *localization* of the electronic excitation in the impact zone, caused by the *slow* passage of the projectile through the surface.

In particular, the ε_0 term is associated to the *broadening* of the energy distribution of excited electrons, due to electron-electron interactions in the impact region. Considering silver clusters impacting on HOPG and Pt, ε_0 appears to have approximately the same trend as a function of cluster size. This similarity in the behavior of ε_0 for the different substrates hints at a relation between this parameter and *some* cluster properties. An interesting observation is that the ε_0 oscillatory behavior reproduces oscillations in the clusters *Ionization Potential*. This observation is only speculative, for the moment, and

[8]The domain of applicability of the Lindhard-Scharff formula is described by the ratio between a Bohr radius-related quantity and the collision diameter.

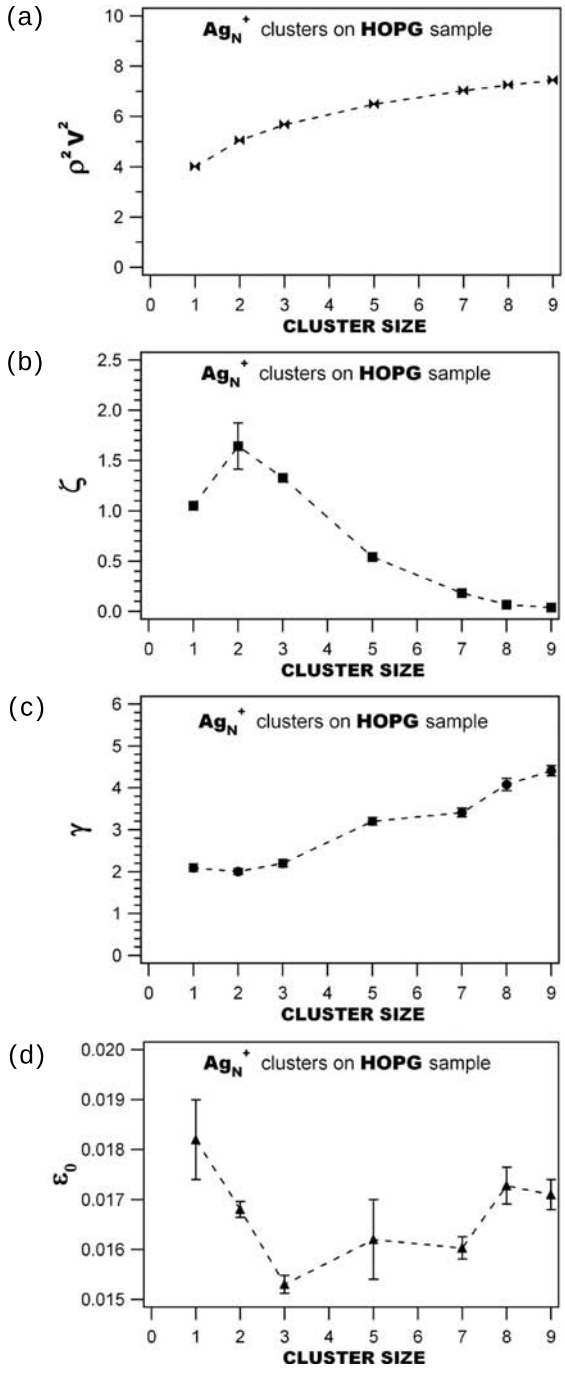

Figure 6.10: Fit parameters of our data fitted by the "mKE" model of Lörinčík and coworkers (see Eq. 6.12). ρ^2V^2 is calculated from the Lindhard-Scharff formula [123] (no errors are included), ζ is a "correction" factor, γ characterizes the *high-velocities* emission yield behavior while ε_0 is a *low-velocity* fit parameter. Errors correspond to standard deviations. If not visible they are smaller than the marker size. The analyzed emission yield curves are related to the impact of Ag_N^+ clusters on the graphite (HOPG) target.

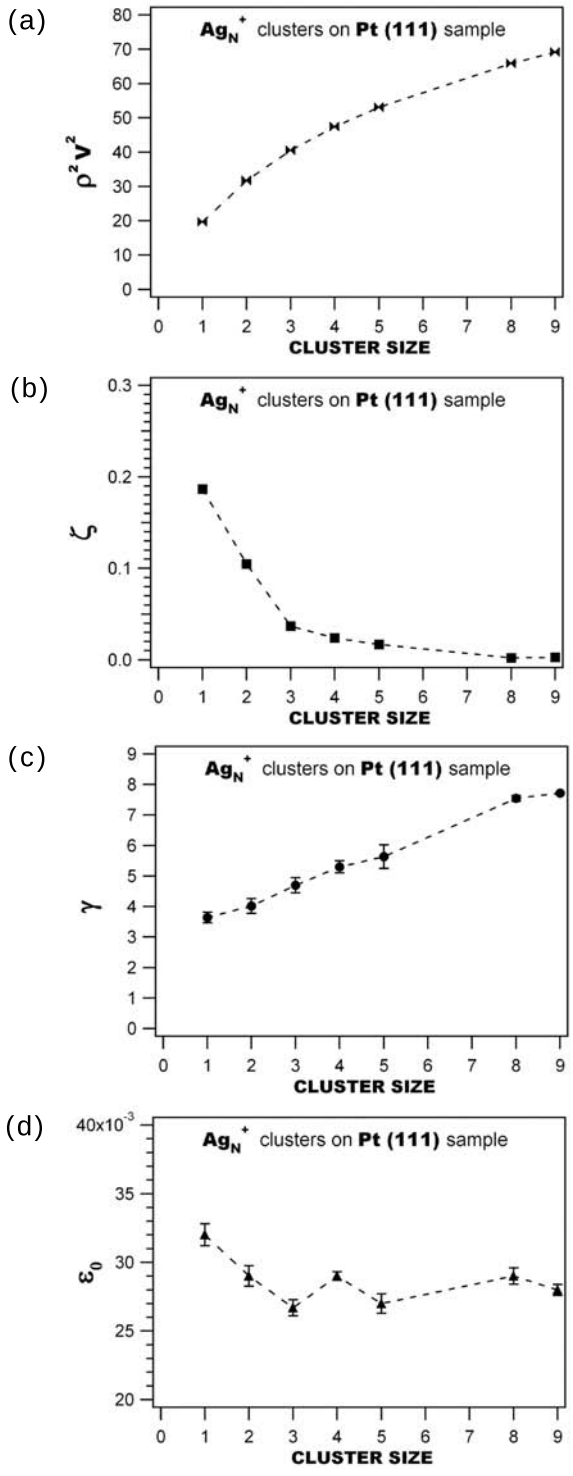

Figure 6.11: As indicated in Fig. 6.10. The analyzed emission yield curves correspond to the impact of Ag_N^+ clusters on the Pt(111) target.

need further developments. However, it is difficult to state if we observe "reliable" oscillations in the ε_0 behavior, due to the very low absolute value of the parameter.

In the context of the interpretation of our data by the Lörinčík model, we can also understand and explain the higher emission yields observed for cluster impact on Pt rather than on HOPG (Fig. 6.6). If we describe the electron emission yield through Eq. 6.12, a different value of the multiplicative term $\rho^2 V^2$ (not dependent on the velocity) is responsible of shifting the whole γ curve on the y-axis. In other words, the overall emission yield increases with increasing $\rho^2 V^2$. This product term is related to the *electronic* stopping of the projectile [125]. It should be kept in mind that it is the electronic part of the stopping which is relevant. This means that a higher electronic density in the valence electrons reflects in a higher electron emission yield. This would explain the higher emission for clusters impact on Pt, which presents a higher DOS at the Fermi level with respect to the HOPG substrate (see Figs. 2.7 and 2.9).

6.5.3 Molecular effect in the emission yields

The simplest approximation for EE by cluster projectiles is that each atom of the cluster counts for its own and contributes with its threshold and yield. Very low thresholds have been found for large clusters impact in agreement with our results. Large water clusters as measured by Beuhler *et al* [126] have shown a threshold down to 19 km/s for gas covered Cu and 9.5 km/s from aluminium oxide targets [127]. Going to large organic molecules like albumin (m=66000 amu) even thresholds as low as 7 km/s have been found. In the context of the discussion above, we have to compare these data that somehow describe a detection limit in the electron yield per atom which becomes extremely small. More interesting than the threshold is the molecular effect in the electron yield. In the following section we discuss the existence of a molecular effect in the electron emission yield i.e.

$$\gamma(N) = RN\,\gamma(N_{ref}) \tag{6.14}$$

where N_{ref} is a *reference* cluster size. The parameter R is *larger than 1* in the case of a *superlinear* effect whereas R is < 1 in the case of a *sublinear* effect.

Superlinear effects were typically found in processes where nuclear stopping dominates the outcome as for example sputtering. Andersen *et al* [128] have found an R as high as 55 for gold clusters hitting a gold surface. Fig. 6.12 shows the sputtering outcome per atom for this example. This is different in processes where the electronic stopping dominates the physical process, as for example electron emission in the kinetic regime. For light projectile cluster ions as for example hydrogen, R<1 is found at low

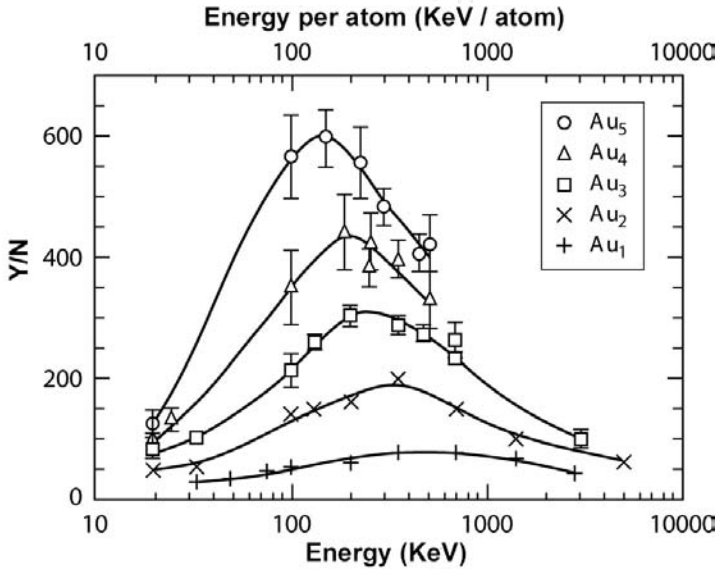

Figure 6.12: Normalized sputtering yield as a function of impact energy and cluster size. After Andersen *et al.* [128]

velocities and R>1 at higher velocities (above 5000 km/s) [129–132].
In the intermediate mass range (for the constituents) R=1 and R<1 is found. Beuhler and Friedman [126] measured the yield of water clusters and found R=1 for a Cu substrate and R<1 for an aluminium oxide target.
The situation is much more complex for heavy cluster projectiles at low energies. Thum and Hofer [133] found R=1 for V_N^+ and Nb_N^+ clusters on stainless steel over the whole measured energy range. Oliva-Florio and coworkers [134], in contrast, observed R>1 for Xe^+ on Au.

The measurements reported here can clearly be classified into the heavy projectiles. There are two different ways to parameterize R, either as a function of velocity or a function of cluster size. Fig. 6.13 shows R as a function of particle velocity for the HOPG and the Pt sample. The R values have been obtained from the fits after equation 6.12. This choice has been made since the experimental data points although taken at the same energies do not cover the same velocity. R in both graphs is normalized to the monomer for cluster sizes up to 3 and to the trimer for sizes up to 9. This choice is given by the experimental energy range covered. There is no velocity overlap between clusters larger than 5 and the atom. For both substrates we find a clear trend: a sublinear effect (R<1) at low velocities crossing R=1 at around 25 km/s and showing a superlinear effect at higher velocities similar to the case of hydrogen projectiles.
In addition to the velocity dependence we find this effect to be size dependent as shown

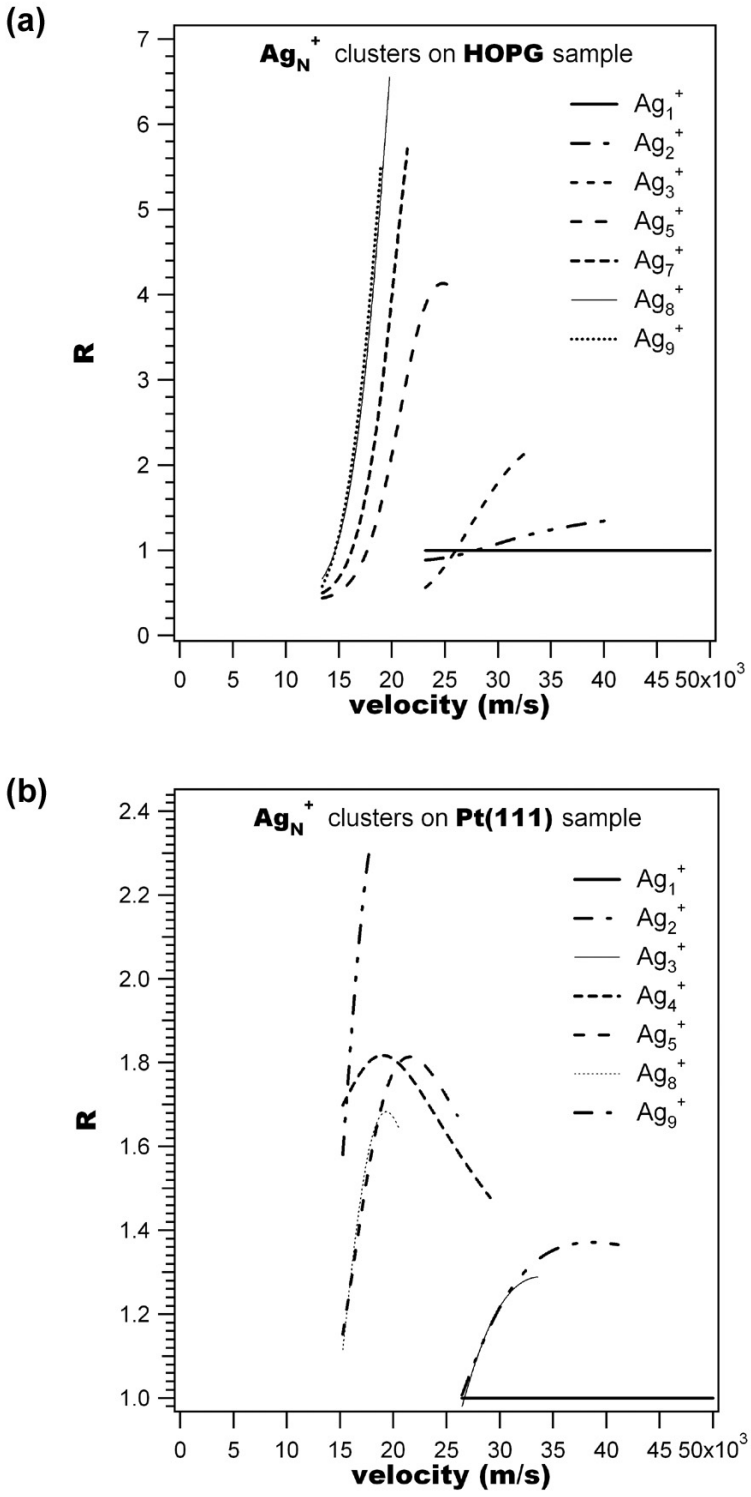

Figure 6.13: The factor R (Eq. 6.14) is plotted as a function of the cluster velocity for each cluster size N colliding on the (a) HOPG, (b) Pt(111) target. Emission yields up to the size N=3 have been normalized on the monomer curve, while larger sizes emission yields have been normalized on the trimer curve.

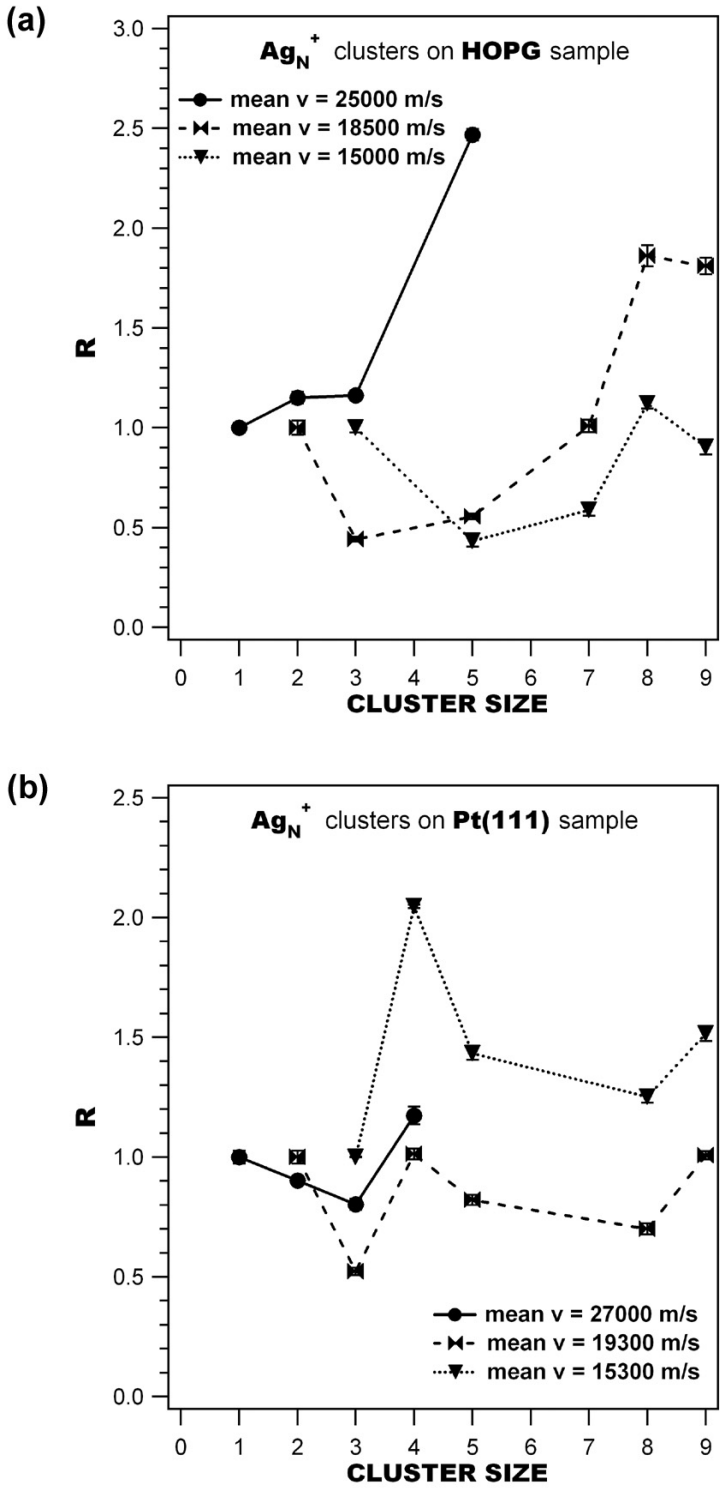

Figure 6.14: The factor R (Eq. 6.14) is plotted as a function of the cluster size, for clusters impact on the (a) HOPG, (b) Pt(111) target. The mean of electron emission yields has been calculated in a 100 m/s region around the specified velocity value. Errors bars are also indicated, which are related to standard deviations in the calculated mean values.

in Fig. 6.14. Three data sets for different *mean* velocities are given. For the *lower* of these velocity values, $\gamma(N)$ has been normalized on the *trimer* mean yield, for the *intermediate* velocity it has been normalized on the *dimer* mean yield, and for the *highest* speed the normalization has been calculated on the *monomer* mean yield. The effect of superlinearity increases as the cluster size increases, the effect being more evident when HOPG is used as substrate.
There exists no satisfying explanation of these observations in the moment and the following discussion has to be considered as speculative.

Thermionic emission in thermal spikes

A molecular effect could be expected due to the increased energy density involved in cluster-surface collisions. The high energy density leads to a superheated solid in a relatively small volume. Molecular dynamics calculations from Betz and Husinsky [135], for example, show that in $Al_N \,/\, Cu$ collisions at comparable energies as used here temperatures exceeding 5000 K are locally reached. This thermal spike lasts for some picoseconds. We can make a simple estimation using the Richardson-Dushman equation [136]:

$$J = A\,T^2\,e^{-\frac{W_\phi}{kT}} \tag{6.15}$$

to calculate thermionic emission. In Eq. 6.15 J is the emission of the hot emitting surface (amps/cm^2), A is a constant, T the temperature of the hot surface (K), W_ϕ corresponds to the work function (eV) and k is the Boltzmann's constant ($1.371 \cdot 10^{-23}$ J/K).
Applying typical parameters for Ag and Pt or HOPG result in electron yields comparable or higher than the ones measured. However, in order for EE to occur, we have to heat up the electron gas to the same temperature as the lattice. This however is not straightforward since it needs a considerable number of electron phonon collisions due to the large mass mismatch between the particles. If we accept that the velocities of the atoms in the spike region are Maxwell-Boltzmann distributed, only valence electrons can be excited which are more or less delocalized. Travelling approximately at the Fermi velocity, the electron leaves the hot spike region very fast and can not be heated effectively. This is different in loosely bound core level electrons. If the tail of the Maxwell-Boltzmann distribution has enough energy to excite these electrons, electron emission is then induced by an Auger emission from an inner shell hole decay. This argument is consistent with both the speed dependence and, in particular, the size dependence of the R parameter.
Thermionic EE from backscattered projectiles of sputtered substrate material as seen by Yeretzian *et al.* [137] can be neglected here, since the bond energies compared to the

ionization potentials are too small to open this channel.

6.5.4 Charge exchange dynamics

Recent interesting results by the group of K.H.Meiwes-Broer [41, 42] suggest that the electron emission yield may reflect the femtosecond neutralization dynamics during the cluster-surface collision. This phenomenon has already been observed in light atoms-surface collisions, but not yet studied with clusters as projectiles. The authors also state that the size-dependence of the emission yield can give information about the cluster-surface interaction potential.

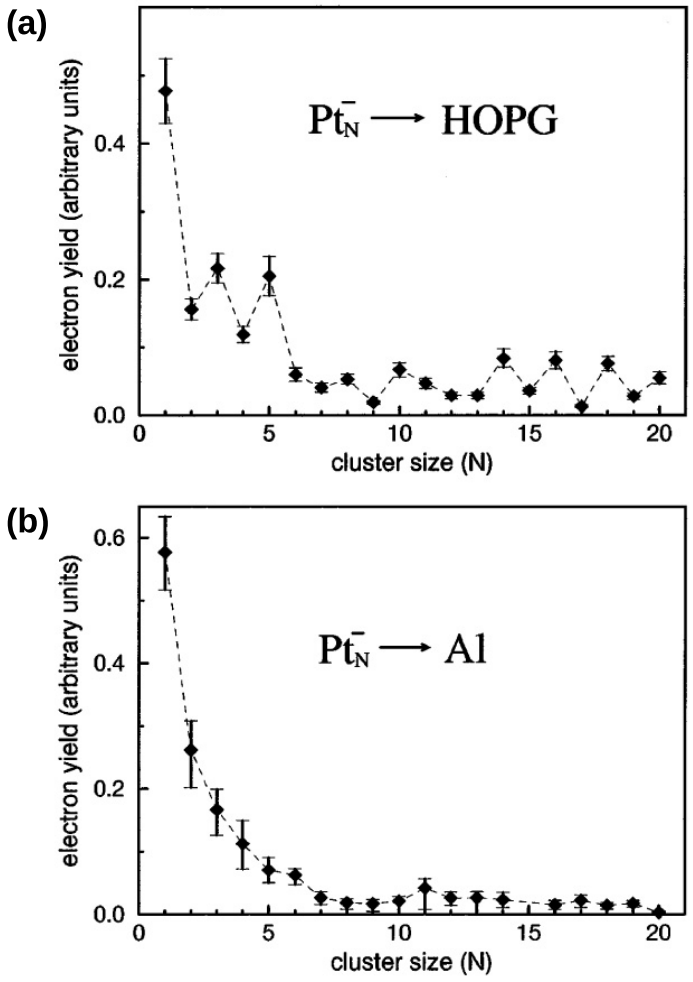

Figure 6.15: Measured electron yield γ as a function of cluster size N for Pt_N^- clusters colliding with (a) a graphite (HOPG) target (oscillations are evident), and (b) an aluminum surface (no oscillations). In both cases the collision energy E_{coll} equals 500 eV (from Ref. [41]).

Their results are shown in Fig. 6.15, where the measured electron yield (which is

not normalized by the number of cluster atoms, but corresponds to the number of emitted **electrons per** incident **cluster ion**) is plotted as a function of size N for Pt_N^- clusters colliding with a HOPG and an Al surface. For a fixed collision energy of 500 eV, remarkable size-dependent features of $\gamma(N)$ are obtained using HOPG as target: the electron emission yield shows characteristic oscillations as a function of cluster size. In addition, the *form* of odd-even oscillations is found to depend on the collision energy. A similar oscillating pattern has been recorded by the same authors when studying the electron emission for Pb_N^+ and Pb_N^- clusters colliding on the same (HOPG) target [42]. In contrast to the results indicated in Fig. 6.15(a), experiments performed under the same conditions but using Al as substrate yield a smoothly decreasing $\gamma(N)$ for increasing cluster size. The completely different behavior of the electron yield when changing the target suggests that the cluster-surface interaction is more important than the electronic structure of the cluster itself. Moreover, the strong dependence of γ on the cluster size and the impact energy, suggests a relation between the electron yield and the incident cluster velocity.

Without entering into the details of the model described in Ref. [42], we briefly summarize its fundamental lines.

The authors assume a relation between the charge-exchange process during the cluster-surface collision and the electron emission yield. In particular, their basic assumption consists in creating a correspondence between the electron emission and the cluster *charge state* at the impact. In other words, only if the cluster reaches the surface unneutralized can an electron be emitted. They calculated the *nonadiabatic survival probability* $P_s(N,t_0)$ of the charged clusters, for different systems. This quantity represents the probability that the charged cluster of size N remains unneutralized until the time t_0, when it reaches the surface. For surfaces with narrow density of states $P_s(N)$ exhibits damped Stückelberg oscillations as a function of N, while for metallic targets (characterized by a very broad bandwidth) it monotonically decreases with increasing cluster size. A comparison between the calculated $P_s(N)$ at the time t_0 and the experimental $\gamma(N)$ yields a very good accordance between the two. This result supports the idea that electron emission reflects the neutralization dynamics of the clusters during the collision.

Thus, in the results presented in Fig. 6.15 the most important effect causing damping is the nonzero width of the $2p_z$ band (see Sect. 2.2.2) of HOPG (Fig. 6.15(a)), while the broad band of the DOS of Al causes a complete oscillations damping yielding a monotonous decreasing behavior of γ (Fig. 6.15(b)).

Since all clusters have the same kinetic energy (500 eV) one can interpret the size dependence of γ as a velocity dependence. This means that the oscillatory behavior of the emission yield vs the cluster size can be transformed in oscillations of the emission yield as a function of velocity, for each cluster size. Looking at Fig. 6.6, which shows all the emission data we collected, we don't observe remarkable oscillations neither for clusters impact on Pt, where no oscillations are expected, nor in the case of impact on HOPG.

However, a direct comparison with Meiwes-Broer curves is not straightforward, as the electron yield they measured is expressed in arbitrary units and it is not normalized on the number N of cluster atoms. We first *divided* their measured emission yield for the Pt_N^+ on HOPG system (Fig. 6.15) by the correspondent cluster size N, obtaining an **emission yield per cluster atom**. We then transformed their oscillatory curve in a "yield vs velocity" curve, associating to each cluster size the cluster velocity correspondent to 500 eV impact energy. Finally, we normalized the first of their data points to one of our measured yields at the same velocity.

Results are shown in Fig. 6.16. We note a remarkable accordance over two orders of magnitude between the general trend of our data and the results by Meiwes-Broer and coworkers. However, we cannot find clear evidence of significative oscillations, reproducible in different cluster sizes. Remind that between our experiments and Meiwes-Broer ones the projectile changes, but, in any case, we expect damped oscillations if HOPG is used as target and non for Pt.

To further verify whether there are oscillations in our data, we followed the inverse path and transformed our "normalized yield vs velocity" curves into (mean) "not-normalized yield vs size" at fixed impact energies of 500 and 600 eV. The new yield corresponds to a mean value of the measured electron yield calculated over a 100 eV region around 500 and 600 eV. This calculated mean yield is multiplied by the correspondent cluster size N (*not-normalized*) and plotted as a function of N. Fig. 6.17 contains the comparison between our (mean) "not-normalized yield vs size" (for silver clusters impact on both HOPG and Pt) and the oscillatory emission behavior of the results of Refs. [41, 42]. Again, we cannot find a direct correspondence between the different data. Even by changing the cluster impact energy the general trend in our emission curves doesn't change considerably, and it presents different features with respect to the oscillatory behavior of Meiwes-Broer and coworkers curves.

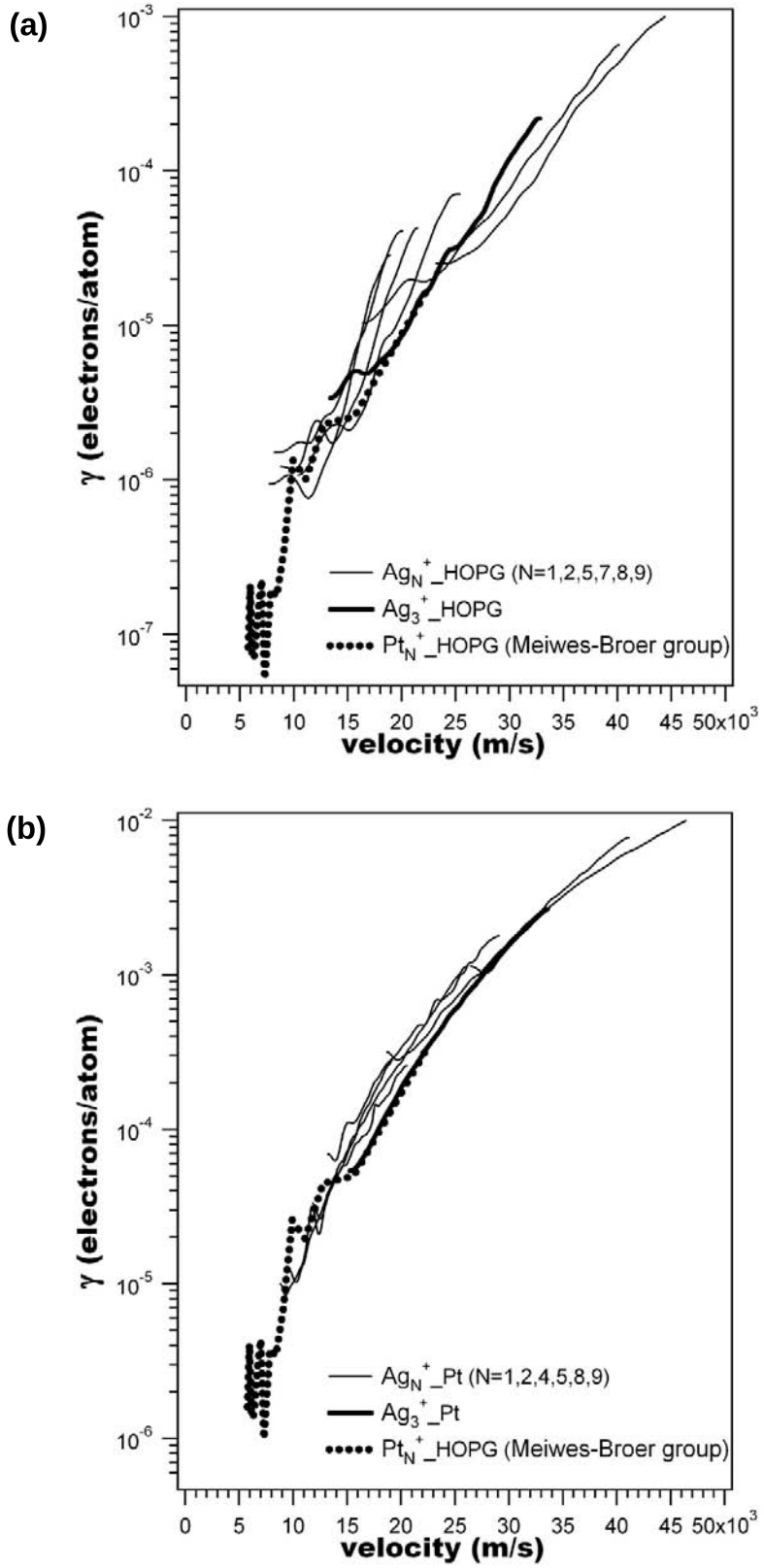

Figure 6.16: Direct comparison between the oscillatory results of Meiwes-Broer and coworkers and our electron emission yield induced by the impact of silver clusters on the (a) HOPG, (b) Pt substrate.

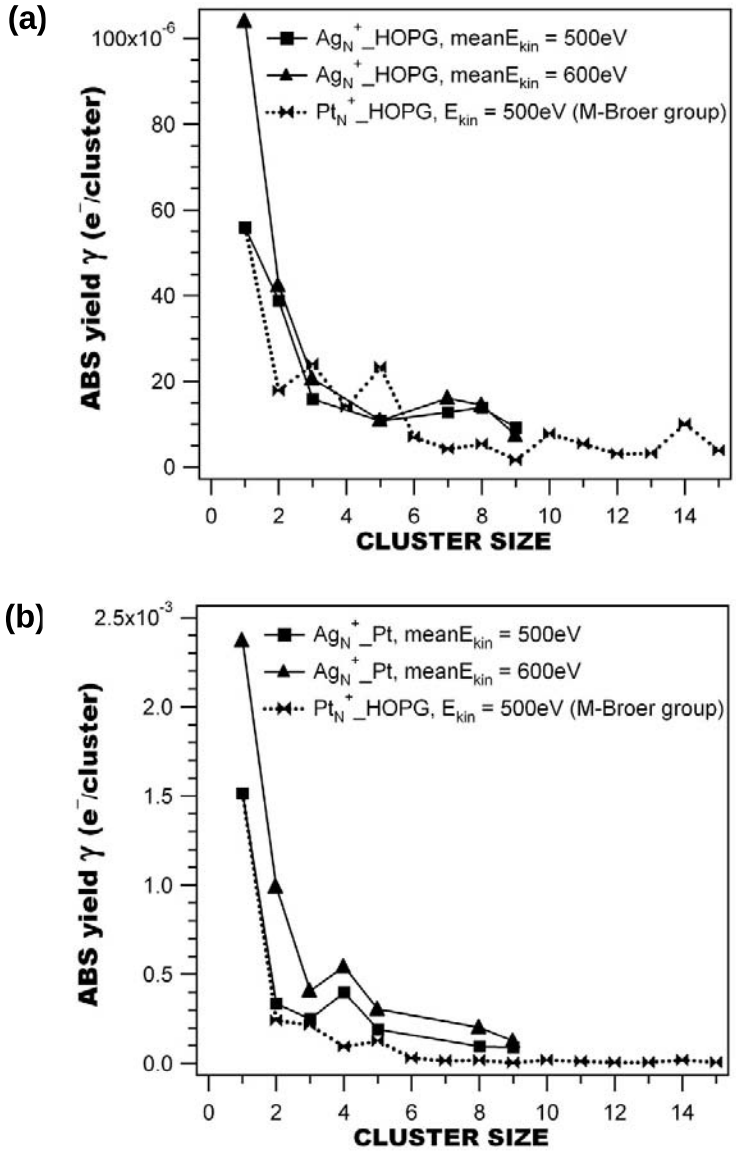

Figure 6.17: Direct comparison between the oscillatory results of Meiwes-Broer and coworkers and our **mean** *absolute* electron emission yield induced by the impact of silver clusters on the HOPG (a) and the Pt (b) substrate. The mean value of the recorded emission yield has been calculated over a 100 eV symmetric region around 500 eV and 600 eV clusters impact energy.

6.6 Conclusions

In summary, we have reported a systematic study of the electron emission following the impact of Ag_N^+ clusters on HOPG and Pt(111) substrates. For all systems we observed a *potential emission* only in the case of the monomer. This emission has been explained assuming a combined process of *neutralization and de-excitation* of the incoming projectile in front of the surface. This process provides enough energy for an electron to be emitted.

An analysis of electron emission data yields the presence of "subthreshold kinetic emission", which cannot be explained by classical models. A model by the Winter's group which is based on the semilocalization of target valence electrons is found to fit very well our experimental data. The obtained fit parameters shed light into the process of electron emission. In particular, the term γ is found to increase with cluster size, hinting at a higher contribution of inner shell electrons to the emission yield for larger projectiles.

Higher emission yields have been measured for Pt than for HOPG, the phenomenon being ascribed to the Pt higher density of states (DOS) at the Fermi level. Emission yield data clearly show a molecular effect, with a shift of emission curves with cluster size which is more important for impact on HOPG than on Pt. In particular, a size-dependent *sublinear* effect is found at low velocities whereas the behavior becomes *superlinear* at higher velocities.

Finally, we observe a remarkable agreement with the general trend of the results of Meiwes-Broer's group. However, no evidence of oscillations in the emission yield as a function of velocity is found.

Chapter 7

Conclusion

Mass-selected clusters deposited on surfaces in a controlled way act as *building blocks* for the creation of nanostructured materials.
We have performed a systematic analysis of the *implantation* of mass-selected silver clusters into an HOPG target. This study has been conducted as a function of the cluster size N (N=1,3,7,9,13) over a broad impact energy range (1-30 KeV).
A good understanding of the *rules* which define implantation allows to control the production of these well-defined vertical nanostructures. The dependence of the penetration depth on the different impact parameters has been investigated as a function of the cluster size. The linear behavior of this depth vs the cluster *momentum* has confirmed recent results obtained for C_{60}^{+}, Ag_{7}^{+} and Au_{7}^{+} colliding on the same HOPG substrate.
The influence of the cluster geometry on clusters implantation has been also analyzed. A *universal* behavior is found when *scaling* the momentum with the *cluster projected surface*. The step from the simple *liquid drop* approximation to the *actual calculated* cluster geometry improves considerably the agreement with experimental data. The linearity between implantation depth and this *scaled* momentum unifies different elements and different cluster sizes.
The *stopping power* experienced by the cluster when penetrating the substrate has been also investigated. This quantity is found to be *nonlinear* in the number of cluster atoms. In other words, the specific *energy loss* per cluster atom is smaller than that of an atomic projectile. In particular, we have succeeded in quantifying this nonlinearity.

The dynamics of the cluster-surface interaction is itself a subject of increasing interest. The main motivation for studying electron emission induced by clusters impact on surfaces is the possibility to gain information about charge transfer and molecular processes in the cluster-surface collision.
Electron emission yields have been systematically measured for size-selected Ag_{N}^{+}

(N=1,2,3,4,5,7,8,9) clusters colliding on HOPG and Pt(111).
Potential emission is energetically allowed only for the monomer, when considering a combined process of *deexcitation* and *neutralization* of the ion in front of the surface. Our results confirm this model, and no PE is observed for cluster sizes N≠1.
Kinetic Electron Emission is observed *below* the classical threshold. This *subthreshold KE* is interpreted within a recent non-classical model based on the *localization* of target valence electrons. The model yields an analytical expression for the emission yield, which fits very well our experimental data. Moreover, the γ fit parameter indicates a higher contribution of inner shells electrons to the emission yield for larger cluster sizes. The trend of the ε_0 parameter as a function of the cluster size might reproduce the behavior of size-dependent cluster electronic properties. These considerations are speculative and need further verification.
However, we believe that an accurate calculation of *molecular orbitals* for the considered systems and the correct evaluation of *correlation diagrams* would yield the right answer for the observed trend of subthreshold electron emission. This possibility should be considered for future developments of these studies.
In addition, we measured higher emission yields for Pt with respect to HOPG. The higher contribution to electron emission is assumed to be related to the higher Pt DOS at the Fermi level.
Molecular effects in the emission yields are also considered. The crucial question is whether the electron emission per atom *increases* or *decreases* with cluster size. We report *velocity-dependent* molecular effects in the emission yields. In particular, a size-dependent *sublinear* effect is recognized at low velocities, whereas it becomes *superlinear* at higher velocities. These results agree with similar observations reported in the literature.
Recent results by the group of Meiwes-Broer suggest a correspondence between the charge-exchange dynamics in cluster-surface collisions and the electron emission yield. Within this picture, charge oscillations related to the dynamics of the collision would reflect themselves in oscillations in the emission yield. We do not recognize oscillations in our emission data, neither as a function of cluster size, nor of velocity.

As regards the future developments of this work, it would be interesting to perform Scanning Tunneling Spectroscopy (STS) on mass selected metallic clusters *pinned* to preformed *nanopits* on the HOPG surface. This study could provide a unique insight of the discrete electronic levels of individual isolated nanostructures. The behavior of the clusters electronic properties as a function of size is of major fundamental interest.

On the other hand, further information on the electronic structure of the cluster-surface system is still an open question in current research.

Appendix A

Protocol of Experimental Procedures

The scope of this appendix is to provide a step-by-step description of the *implantation* experimental procedure. References are provided to the sections which describe in detail the single tools employed in the experiment. This text is written for the next users of this apparatus who will perform these kind of studies. The reader is anyway supposed to know how the whole machine works.

A.0.1 Implantation of silver clusters into HOPG

- The HOPG sample is glued to the sampleholder (Sect. 4.2.1) and cleaved before insertion into vacuum. The sampleholder is then screwed on a support (Sect. 4.2.1) which allows to bias the sample from the exterior of the main chamber. The sample is finally inserted into the main chamber which is evacuated to a vacuum of the order of 10^{-7}mbar.

- The next operation consists in heating the filaments of the cluster source (Sect. 4.3.1). This operation lasts for almost one hour, time required to get a stable cluster current.

- The front end of the quadrupole of the cluster source is placed at a distance of $1\,cm$ off the sample surface. In this way the clusters are guided by the quadrupole in the direction of the sample surface and they are deposited all over the surface. The focalization of the cluster beam increases as the bias voltage applied on the sample increases.

- Prior to deposition, the cluster current reading device (Sect. 4.3.2) is placed be-

tween sample and quadrupole in its total current reading position. It allows to measure and optimize the (positive) current of the impinging cluster ions on the sample (which cannot be measured and controlled during deposition). During this operation the sample is maintained at a constant positive voltage (approximately $200eV$), in order to prevent clusters to reach the surface.

- The cluster source is then started and the potentials of the extraction lenses as well as of the Bessel box are optimized for the chosen cluster mass. For implantation experiments, low cluster currents of the order of $10\,pA$ are sufficient, and easily achievable with source filaments currents of the order of $5\,mA$.

- When the total current is optimized, the potential fixed on the silver target (sputtering target of the cluster source) is switched off, preventing any cluster to hit the surface. All other potentials as well as the quadrupole radio frequency are maintained, and the Faraday Cup is retracted.

- It is now possible to set the cluster deposition energy by biasing the HOPG sample at the desired potential. The cluster deposition is started by switching on the potential on the silver target. The deposition usually takes $5-10\,s$, which yields a mean coverage of the order of 100 impacts/μm^2, if the impinging clusters current is of the order of $10\,pA$, as mentioned before.

- The deposition is stopped by switching off the potential on both the silver target and the HOPG sample. The cluster source can be stopped and the vacuum broken. Before breaking vacuum a waiting time of almost a quarter of hour is necessary to let the filaments of the cluster source cooling.

- The sample can finally be extracted from the chamber and detached from the sampleholder, taking care of eliminating all rests of glue.

A.0.2 Oxidation of the sample

- Prior to the oxidation of the sample, the oven (Sect. 4.4.1) is evacuated to a pressure of $\simeq\ 10^{-5}\ mbar$ and heated up to a temperature of $\simeq\ 800^{\circ}\ C$. The sample ceramic holder (described in sect. 4.2.1) is cleaned by being inserted for almost one hour in the center of the main chamber of the oven. Almost one hour is then required to let the sample holder cool to ambient temperature, and the oven at a temperature of $\simeq\ 650^{\circ}\ C$.

- The sample within its holder is then inserted into the intermediate chamber, ready to be oxidized.

- Once the pressure of the two coupled chambers reach the value of approximately $\simeq 10^{-5}\ mbar$, a cleaning of the sample is performed, by introducing it close to the center of the main chamber ($\simeq 2\ min$ at $\simeq 650°\ C$). This cleaning operation allows to desorb all the impurities that have deposited on the sample surface.

- After withdrawing the sample again in the intermediate chamber, a controlled oxygen flow is introduced into the oven, in order to get to a pressure of $\simeq 100\ mbar$.

- Oxidative etching in a controlled oxygen atmosphere is finally accomplished by inserting the sample into the main chamber of the furnace ($\simeq 25 - 30\ min$ at $\simeq 650°\ C$).

A.0.3 Imaging by Scanning Tunneling Microscopy

- The sample is cooled down to ambient temperature. Approximately two hours are needed to stabilize the ambient temperature of the sample and avoid noisy drifts in the STM measurements.

- The sample is finally examined by the "home-built" STM in air, which has been described in Sect. 4.4.2. Images are taken at typical currents of the order of $1-2\,nA$ and bias voltages of approximately $1-2\,V$ (the sample is positively biased respect to the tip).

Bibliography

[1] H. Brune, M. Giovannini, K. Bromann, and K. Kern, Nature **394**, 451 (1998).

[2] K. Bromann, C. Félix, H. Brune, W. Harbich, R. Monot, J. Buttet, and K. Kern, Science **274**, 956 (1996).

[3] R. Schaub, H. Jödicke, F. Brunet, R. Monot, J. Buttet, and W. Harbich, Physical Review Letters **86**, 3590 (2001).

[4] D. M. Eigler and E. K. Schweizer, Nature **344**, 524 (1990).

[5] U. Heiz, Applied Physics A **67**, 621 (1998).

[6] U. Heiz, A. Sanchez, S. Abbet, and W.-D. Schneider, The European Physical Journal D **9**, 35 (1999).

[7] A. Sanchez, S. Abbet, U. Heiz, W.-D. Schneider, H. Hkkinen, R. N. Barnett, and U. Landman, Journal of Physical Chemistry A **103**, 9573 (1999).

[8] U. Heiz, A. Sanchez, S. Abbet, and W.-D. Schneider, Journal of the American Chemical Society **121**, 3214 (1999).

[9] U. Heiz and W.-D. Schneider, Journal of Physics D: Applied Physics **33**, R85 (2000).

[10] S. Abbet, A. Sanchez, U. Heiz, and W. D. Schneider, Journal of Catalysis **198**, 122 (2001).

[11] A. S. Wörz, K. Judai, S. Abbet, and U. Heiz, Journal of the American Chemical Society **125**, 7964 (2003).

[12] H. Häkkinen, W. Abbet, A. Sanchez, U. Heiz, and U. Landman, Angewandte Chemie-International Edition **42**, 1297 (2003).

[13] E. Wahlström, N. Lopez, R. Schaub, P. Thostrup, A. Ronnau, C. Africh, E. Laegsgaard, J. K. Norskov, and F. Besenbacher, Physical Review Letters **90**, 026101 (2003).

[14] D. J. Kenny, S. Weller, M. Couillard, R. E. Palmer, C. F. Sanz-Navarro, and R. Smith, The European Physical Journal D **16**, 115 (2001).

[15] S. J. Carroll, S. G. Hall, R. E. Palmer, and R. Smith, Physical Review Letters **81**, 3715 (1998).

[16] S. J. Carroll, K. Seeger, and R. E. Palmer, Applied Physics Letters **72**, (1998).

[17] S. J. Carroll, P. Weibel, B. v. Issendorff, L. Kuipers, and R. E. Palmer, Journal of Physics : Condensed Matter **8**, L617 (1996).

[18] S. J. Carroll, P. D. Nellist, R. E. Palmer, S. Hobday, and R. Smith, Physical Review Letters **84**, 2654 (2000).

[19] S. J. Carroll, R. E. Palmer, P. A. Mulheran, S. Hobday, and R. Smith, Applied Physics A **67**, 613 (1998).

[20] S. J. Carroll, S. Pratontep, M. Streun, R. E. Palmer, S. Hobday, and R. Smith, Journal of Chemical Physics **113**, 7723 (2000).

[21] I. M. Goldby, L. Kuipers, B. v. Issendorff, and R. E. Palmer, Applied Physics Letters **69**, 2819 (1996).

[22] C. M. Grimaud and R. E. Palmer, Journal of Physics : Condensed Matter **13**, 1869 (2001).

[23] J. R. Hahn and H. Kang, Surface Science **446**, L77 (2000).

[24] S. G. Hall, M. B. Nielsen, and R. E. Palmer, Journal of Applied Physics **83**, 733 (1998).

[25] B. Kaiser, T. M. Bernhardt, and K. Rademann, Applied Physics A **66**, S711 (1998).

[26] D. J. Kenny, R. E. Palmer, C. F. Sanz-Navarro, and R. Smith, Journal of Physics : Condensed Matter **14**, 185 (2002).

[27] S. Pratontep, P. Preece, C. Xirouchaki, R. E. Palmer, C. F. Sanz-Navarro, D. J. Kenny, and R. Smith, Physical Review Letters **90**, 055503 (2003).

[28] C. T. Reimann, S. Andersson, P. Bruhwiler, N. Martensson, L. Olsson, R. Erlandosson, M. Henkel, and H. M. Urbassek, Nuclear Instruments and Methods in Physics Research B **140**, 159 (1998).

[29] C. F. Sanz-Navarro, R. Smith, D. J. Kenny, S. Pratontep, and R. E. Palmer, Physical Review B **65**, 1 (2002).

[30] C. Brechignac, P. Cahuzac, F. Carlier, C. Colliex, J. Leroux, A. Masson, B. Yoon, and U. Landman, Physical Review Letters **88**, art. no. (2002).

[31] C. Brechignac, P. Cahuzac, F. Carlier, N. Kebaili, J. Le Roux, and A. Masson, Surface Science **518**, 192 (2002).

[32] W. Yamaguchi, K. Yoshimura, Y. Tai, Y. Maruyama, K. Igarashi, S. Tanemura, and J. Murakami, Journal of Chemical Physics **112**, 9961 (2000).

[33] C. Brechignac, P. Cahuzac, F. Carlier, C. Colliex, M. de Frutos, N. Kebaili, J. Le Roux, A. Mason, and B. Yoon, European Physical Journal D **16**, 265 (2001).

[34] C. P. Vinod, G. U. Kulkarni, and C. N. R. Rao, Chemical Physics Letters **289**, 329 (1998).

[35] A. Bettac, L. Köller, V. Rank, and K. H. Meiwes-Bröer, Surface Science **404**, 475 (1998).

[36] H. Hövel, B. Grimm, M. Bodecker, K. Fieger, and B. Reihl, Surface Science **463**, L603 (2000).

[37] H. Hövel, Applied Physics A **72**, 295 (2001).

[38] D. Hasselkamp, *Springer Tracts in Modern Physics* (Springer, Berlin, 1992), Vol. 123, p. 1.

[39] P. Varga and H. Winter, *Springer Tracts in Modern Physics* (Springer, Berlin, 1992), Vol. 123, p. 149.

[40] R. L. Erickson and D. P. Smith, Physical Review Letters **34**, 297 (1975).

[41] B. Wrenger, K. H. Meiwes-Broer, O. Speer, and M. E. Garcia, Physical Review Letters **79**, 2562 (1997).

[42] O. Speer, M. E. Garcia, B. Wrenger, and K. H. Meiwes-Broer, Surface Science **443**, 195 (1999).

[43] W. Harbich, *Collision of clusters with surfaces: surface modification and scattering, Springer Series in Cluster Physics* (Springer Verlag, Berlin, 2000).

[44] H. Hsieh, R. S. Averback, H. Sellers, and C. P. Flynn, Physical Review B **45**, 4417 (1992).

[45] H. P. Cheng and U. Landman, Science **260**, 1304 (1993).

[46] C. Félix, G. Vandoni, C. Massobrio, R. Monot, J. Buttet, and W. Harbich, Physical Review B **57**, 4048 (1998).

[47] H. Jödicke, R. Schaub, R. Monot, J. Buttet, and W. Harbich, Surface Science **475**, 109 (2001).

[48] H. P. Cheng and U. Landman, J. Phys. Chem. **98**, 3572 (1994).

[49] B. Kaiser, T. M. Bernhardt, and K. Rademann, Appl. Phys. A **66**, 711 (1998).

[50] J. Nordiek, M. Moseler, and H. Haberland, Rad. Effects **142**, 27 (1997).

[51] V. Bonacić-Koutecky, L. Cespiva, P. Fantucci, and J. Koutecky, Journal of Chemical Physics **98**, 7981 (1993).

[52] private communication .

[53] C. Jackschath, I. Rabin, and W. Schulze, Zeitschrift fr Physik D - Atoms, Molecules and Clusters **22**, 517 (1992).

[54] J. Zhao, Y. Luo, and G. Wang, The European Physical Journal D **14**, 309 (2001).

[55] I. Rabin, C. Jackschath, and W. Schulze, Zeitschrift fr Physik D - Atoms, Molecules and Clusters **19**, 153 (1991).

[56] I. Katakuse, T. Ichihara, Y. Fujita, T. Matsuo, T. Sakurai, and H. Matsuda, International Journal of Mass Spectrometry and Ion Processes **67**, 229 (1985).

[57] I. Katakuse, T. Ichihara, Y. Fujita, T. Matsuo, T. Sakurai, and H. Matsuda, International Journal of Mass Spectrometry and Ion Processes **74**, 33 (1986).

[58] R. C. Tatar and S. Rabii, Physical Review B **25**, 4126 (1982).

[59] A. Snis and S. F. Matar, Physical Review B **60**, 10855 (1999).

[60] P. R. Watson, M. A. Van Hove, and K. Herman, *Atlas of surface structures*, *Journal of Physical and Chemical Reference Data* (American Institute of Physics for NIST, New York, 1994).

[61] N. V. Smith, G. K. Wertheim, S. Hüfner, and M. M. Traum, Physical Review B **10**, 3197 (1974).

[62] G. Binnig, H. Rohrer, C. Gerber, and E. Weibel, Physical Review Letters **50**, 120 (1983).

[63] C. J. Chen, *Introduction to scanning tunneling microscopy* (Oxford University Press, New York, 1993).

[64] J. Tersoff and D. R. Hamann, Phys. Rev. Letters **50**, 1998 (1983).

[65] R. Schaub, PhD thesis, EPFL, 2000.

[66] H. Jödicke, PhD thesis, EPFL, 1999.

[67] G. Vandoni, PhD thesis, EPFL, 1995.

[68] P. Convers, PhD thesis, EPFL, 2005, to be published.

[69] S. H. Pan, International Patent Publication Number WO 93/19494 **(international Bureau, World Intellectual Property Organization)**, (1993).

[70] S. H. Pan, E. W. Hudson, and J. Davis, Review of Scientific Instruments **70**, 1459 (1999).

[71] O. Pietzsch, A. Kubetzka, D. Haude, M. Bode, and R. Wiesendanger, Review of Scientific Instruments **71**, 424 (2000).

[72] B. Michel, L. Novotny, and U. Dürig, Ultramicroscopy **42-44**, 1647 (1992).

[73] P. Convers, Diploma, EPFL, 2001.

[74] E. L. Evans, R. J. M. Griffiths, and J. M. Thomas, Science **171**, 174 (1971).

[75] G. R. Hennig, in *Chemistry and Physics of Carbon*, edited by J. P. L. Walker (Marcel Dekker, New York, 1966), Vol. 2, p. 1.

[76] J. M. Thomas, in *Chemistry and Physics of Carbon*, edited by P. L. Walker (Marcel Dekker, New York, 1965), Vol. 1, pp. 121–203.

[77] R. T. Yang and C. Wong, Journal of Chemical Physics **75**, 4471 (1981).

[78] R. T. Yang, in *Chemistry and Physics of Carbon*, edited by J. P. L. Walker and P. A. Thrower (Marcel Dekker, New York, 1984), Vol. 19, pp. 163–210.

[79] X. Chu and L. D. Schmidt, Carbon **29**, 1251 (1991).

[80] H. Chang and A. J. Bard, Journal of the American Chemical Society **113**, 5588 (1991).

[81] H. Chang and A. J. Bard, Journal of the American Chemical Society **112**, 4598 (1990).

[82] A. Tracz, G. Wegner, and J. P. Rabe, Langmuir **9**, 3033 (1993).

[83] F. Stevens, L. A. Kolodny, and T. P. Beebe, Journal of Physical Chemistry B **102**, 10799 (1998).

[84] G. R. Hennig, Journal of Chemical Physics **40**, 2877 (1964).

[85] G. Bräuchle, S. R. Schneider, D. Illig, J. Rockenberger, R. D. Beck, and M. M. Kappes, Applied Physics Letters **67**, 52 (1995).

[86] J. R. Hahn, H. Kang, S. M. Lee, and Y. H. Lee, Journal of Physical Chemistry B **103**, 9944 (1999).

[87] J. R. Hahn and H. Kang, Physical Review B **60**, 6007 (1999).

[88] J. R. Hahn and H. Kang, Surface Science **357-358**, 165 (1996).

[89] J. R. Hahn, H. Kang, S. Song, and I. C. Jeon, Physical Review B **B53**, R1725 (1996).

[90] S. M. Lee, Y. H. Lee, Y. G. Hwang, J. R. Hahn, and H. Kang, Physical Review Letters **82**, 217 (1999).

[91] J. R. Hahn and H. Kang, Journal of Vacuum Science and Technology A **17**, (1999).

[92] J. F. Ziegler and J. P. Biersack, TRIM code, 1992.

[93] R. Coratger, A. Claverie, A. Chahboun, V. Landry, F. Ajustron, and J. Beauvillain, Surface Science **262**, 208 (1992).

[94] T. Li, B. V. King, R. J. MacDonald, G. F. Cotterill, D. J. O'Connor, and Q. Yang, Surface Science **312**, 399 (1994).

[95] K. H. Lee, H. M. Lee, H. M. Eun, W. R. Lee, S. Kim, and D. Kim, Surface Science **321**, 267 (1994).

[96] M. Henkel and H. M. Urbassek, Nuclear Instruments and Methods in Physics Research B **145**, 503 (1998).

[97] R. P. Webb, M. Kerford, M. Kappes, and G. Bräuchle, Nuclear Instruments and Methods in Physics Research B **122**, 318 (1997).

[98] G. Bräuchle, S. R. Schneider, D. Illig, R. D. Beck, H. Schreiber, and M. M. Kappes, Nuclear Instruments and Methods in Physics Research B **112**, 105 (1996).

[99] S. Gilb, M. Blom, G. Bräuchle, C. Stoermer, R. Wellmann, and M. M. Kappes, , not published.

[100] V. I. Shulga and P. Sigmund, Nuclear Instruments and Methods in Physics Research B **47**, 236 (1990).

[101] V. I. Shulga, Nuclear Instruments and Methods in Physics Research B **58**, 422 (1991).

[102] Z. Pan, Nuclear Instruments and Methods in Physics Research B **66**, 325 (1992).

[103] E. Rutherford, Philosophical Magazine series 6 **10**, 193 (1905).

[104] M. L. E. Oliphant, Proceedings of the Royal Society of London Series A **127**, 388 (1930).

[105] R. A. Baragiola, in *Low energy ion-surface interactions*, *Wiley Series in Ion Chemistry and Physics*, edited by J. W. Rabalais (PUBLISHER, ADDRESS, 1994), p. 188.

[106] H. Eder, W. Messerschmidt, H. Winter, and F. Aumayr, Journal of Applied Physics **87**, 8198 (2000).

[107] J. Lörincík, Z. Sroubek, H. Eder, F. Aumayr, and H. Winter, Physical Review B **62**, 16116 (2000).

[108] H. Eder, F. Aumayr, and H. Winter, Nuclear Instruments and Methods in Physics Research B **154**, 185 (1999).

[109] G. Lakits, F. Aumayr, M. Heim, and H. Winter, Physical Review A **42**, 5780 (1990).

[110] H. Winter, H. Eder, F. Aumayr, J. Lörincík, and Z. Sroubek, Nuclear Instruments and Methods in Physics Research B **182**, 15 (2001).

[111] H. D. Hagstrum, Physical Review **91**, 543 (1953).

[112] H. D. Hagstrum, Physical Review **96**, 325 (1954).

[113] H. D. Hagstrum, Physical Review **96**, 336 (1954).

[114] R. A. Baragiola, E. V. Alonso, and A. Oliva-Florio, Physical Review B **19**, 121 (1979).

[115] U. Fano and W. Lichten, Physical Review Letters **14**, 627 (1965).

[116] M. Barat and W. Lichten, Physical Review A **6**, 211 (1972).

[117] U. Wille and R. Hippler, Physics Reports-Review Section of Physics Letters **132**, 129 (1986).

[118] L. Guillemot, S. Lacombe, V. N. Tuan, V. A. Esaulov, E. Sanchez, Y. A. Bandurin, A. I. Dashchenko, and V. G. Drobnich, Surface Science **365**, 353 (1996).

[119] E. W. Thomas, Progress in Surface Science **10**, 383 (1980).

[120] M. H. Chen, F. P. Larkins, and B. Crasemann, Atomic Data and Nuclear Data Tables **45**, 1 (1990).

[121] W. E. Meyerhof, Physical Review Letters **31**, 1341 (1973).

[122] E. S. Parilis and L. M. Kishinevskii, Soviet Physics - Solid State **3**, 885 (1960).

[123] J. Lindhard and M. Scharff, Physical Review **124**, 128 (1961).

[124] G. Kalus, U. Litzén, F. Launay, and W. L. Tchang-Brillet, Physica Scripta **65**, 46 (2002).

[125] G. Falcone and Z. Sroubek, Physical Review B **39**, 1999 (1989).

[126] R. Beuhler and L. Friedman, Nuclear Instruments and Methods **170**, 309 (1980).

[127] R. Beuhler, Journal of Applied Physics **54**, 4118 (1983).

[128] H. H. Andersen, A. Brunelle, S. Della-Negra, J. Depauw, D. Jacquet, Y. Le-Beyec, J. Chaumont, and H. Bernas, Physical Review Letters **80**, 5433 (1998).

[129] R. A. Baragiola, E. V. Alonso, O. Auciello, J. Ferron, G. Lantschner, and A. Oliva-Florio, Physics Letters A **67**, 211 (1978).

[130] N. R. Arista, M. M. Jakas, G. Lantschner, and J. C. Eckhardt, Physical Review A **34**, 5112 (1986).

[131] B. Svensson and G. Holmén, Physical Review B **25**, 3056 (1982).

[132] D. Hasselkamp and A. Scharmann, Physica Status Solidi A-Applied Research **79**, K197 (1983).

[133] F. Thum and W. O. Hofer, Surface Science **90**, 331 (1979).

[134] R. A. Baragiola, Nuclear Instruments and Methods in Physics Research B **88**, 35 (1994).

[135] G. Betz and W. Husinsky, Nuclear Instruments and Methods in Physics Research B **122**, 311 (1997).

[136] A. Eastman, *Fundamentals of Vacuum Tubes* (McGraw-Hill, New York, YEAR).

[137] C. Yeretzian, K. Hansen, and R. L. Whetten, Science **260**, (1993).

Curriculum vitae

Name:	Lucia Seminara
Date of Birth:	September 27, 1974
Birth place:	London (GB)
Nationality	Italian
Address:	Av. Tissot 11, 1006 Lausanne, Switzerland
1988–1993	High School at the *Liceo Scientifico G. D. Cassini* in Genoa, Italy
1993–1999	Diploma studies in physics at the University of Genoa, Italy
Apr. 1997–Jul. 1997	Erasmus project at the *Oxford Brookes University*, Oxford (UK)
Feb. 1998–June 1999	Diploma thesis on "Investigation of thin films magnetism by optical techniques", supervisor Prof L. Mattera, University of Genoa, Italy
Dec. 1999–Jan. 2004	Research and teaching assistant in the group of Prof R. Monot and Dr. W. Harbich at the Institute of Nanostructure Physics of the Swiss Federal Institute of Technology in Lausanne, Switzerland
Jan. 2004	PhD thesis: "Implantation and electron emission in cluster-surface collisions"

Acknowledgements - Remerciements

J'aimerais ici remercier toutes les personnes qui m'ont aidé tout au long de ce travail de thèse.

En premier lieu, je tiens à remercier mon directeur de thèse, Dr Wolfgang Harbich, qui m'a donné la possibilité d'effectuer ce travail dans son groupe. J'ai pu profiter de sa présence constante, de ses innombrables idées pour résoudre les problèmes dans le labo, et de sa collaboration assidue pendant la phase finale de rédaction de la thèse.

J'exprime ma gratitude au professeur René Monot, pour son soutien, sa capacité à motiver et à donner confiance aux collaborateurs: les tâches d'assistanat sous votre direction ont été très enrichissantes! Je remercie aussi le Professeur Jean Buttet, qui a toujours montré beaucoup d'intérêt dans mon travail, et dont les conseils ont été précieux dans la phase de rédaction de la thèse.

Merci à mes "premiers" collègues de labo, Renald Schaub et Fréderic Brunet, avec qui on a su créer une atmosphère de travail très agréable, qui m'ont appris tous les secrets de la machine, et avec qui j'ai partagé les premières joies et les premières déceptions des expériences au labo. Et encore merci aux membres du groupe actuel, Pierre Convers et Raphäel Vallotton qui, avec leur patience et tolérance, ont su supporter mes états d'âme très changeants... Un grand merci particulier à Pierre, collègue du bureau depuis longtemps, pour son calme, sa disponibilité et ses compétences!

Dans le cadre de l'Institut, plusieurs autres personnes ont été fondamentales pour ce travail. En premier lieu toute l'équipe de techniciens: Gilles Grandjean, le mâitre de l'art technique et des montagnes suisses, qui a toujours en tête la solution à tous les problèmes... merci pour ton bonheur et pour tes milles idées!! Et encore, en particulier, Claude Blanc, André Schläfli, Michel Fazan, André Guisolan, Martial Doy et José Grandjean pour la résolution des petits-grands problèmes des tous les jours et pour l'atmosphère très amicale, Claire-Lise Bandelier pour sa facilité à ameliorer n'importe quelle image, Françoise Jenny pour l'efficacité dans le démélement des affaires administratives!

Je remercie aussi les autres membres de l'Institut, en particulier Laurent et Bulu pour

la résolution des nombreuses problèmes avec LaTeX, Nicolas pour sa grande compétence avec Solid Works et son "oeil d'homme" pour voir les structures 3D, Max pour sa collaboration "sous le tapis" (...), Slobi pour les conseils techniques sur les portables, pour sa sympathie, et sa disponibilité.

Et encore un grand merci à tous les membres du LMM à l'Institut de Matériaux, mon "deuxième" groupe, pour m'avoir souvent écoutée et soutenue.

Au délà du travail, j'aimerais encore et surtout remercier tous les amis avec qui j'ai partagé des inoubliables moments à Lausanne. "The italian team" au complet, pour les sorties à ski, les balades en montagnes, les fréquents soupers "cuisine italienne", les sorties à la salle des sport, les débats enflammés sur la politique italienne...
Un mot particulier à Laura, ma "guide spirituelle", que j'aimerais remercier pour son soutien, son encouragement, sa confiance en moi, sa sensibilité.
Mes amis et voisins, Ketia et Luigi, parfaits compagnons de discussion, confessions et pates à la dernière minute!
Diego! Mon premier colocataire et vrai ami, qui m'a introduit dans la ville lausannoise et m'a gatée avec sa delicieuse cuisine.
Je tiens enfin à remercier la liste (trop longue pour être nommée au complet...) de tous les autres nombreux amis, à Gênes et à Lausanne, qui m'ont accompagnée pendant ces quatre ans.

Last but not least.. je suis en premier lieu reconnaissante à ma grande famille, "il clan Seminara", mon point de référence dans la vie, et qui a toujours été présente malgré l'éloignement. Un enorme merci pour tout ce que vous m'avez apporté.

Enfin, Ali... un grand merci du fond du coeur pour m'avoir toujours encouragée et soutenue. Merci pour ton sourire et ton calme dans mes moments de stress. Merci pour avoir été une personne sur laquelle j'ai toujours pu conter.

List of Figures